J. Fluid Mech. (1980), *vol.* 97, *part* 1, *pp.* 331–346
Printed in Great Britain

The forces on sharp-edged cylinders in oscillatory flow at low Keulegan–Carpenter numbers

By J. M. R. GRAHAM
Department of Aeronautics, Imperial College, London SW7 2BY

(Received 11 December 1978 and in revised form 22 August 1979)

This paper describes an analysis of the forces induced by separation and vortex shedding from sharp-edged bodies in oscillatory flow at high Reynolds number. The analysis which is valid for the case of small oscillations of the fluid is compared with experimental data obtained at fairly low Keulegan–Carpenter numbers.†

1. Introduction

The understanding of the flow past a body in an oscillatory free stream has important applications in the study of wave induced forces on structures and the behaviour (particularly the damping) of bodies vibrating in a fluid. In the former case the complex three-dimensional flow field which results from the interaction of a free surface wave with a cylindrical structure is frequently approximated by an analogous two-dimensional flow although this does, of course, neglect some important three-dimensional effects. In the latter case the flow induced by a body vibrating in otherwise still fluid is kinematically the same as that due to an oscillating free stream past a stationary body and only dynamically different by the Froude–Krylov force which is in phase with the acceleration and represents the action of the pressure gradients of the imposed flow on the body. As a result two-dimensional oscillatory flows have been quite widely studied experimentally, usually in water, either by vibrating the body or by oscillating the fluid back and forth in a tank.

Probably the most controlled way of producing a uniform fluid oscillation is by means of a U-tube as described by Sarpkaya (1975) who has used this device to make an extensive study of circular cylinders.

Previous to this work Keulegan & Carpenter (1958) made a study of oscillatory flow round both flat plates and circular cylinders using the flow field of a standing water wave. They showed that if the measured force F in the flow direction was expressed in the form of Morison's equation

$$F = \tfrac{1}{2}\rho U|U|\,dC_D + \tfrac{1}{4}\pi\rho\dot{U}d^2C_m, \tag{1}$$

the drag and inertia coefficients C_D and C_m were functions of the Keulegan–Carpenter number $K_c = U_0T/d$. Here U is the free-stream velocity with amplitude U_0, T the period of oscillation, ρ the fluid density and d the body diameter. They did not find any

† The main conclusions of this paper were presented at the International Symposium on Wave Induced Forces on Structures at Bristol, 1978.

0022-1120/80/4414-8840 $02.00

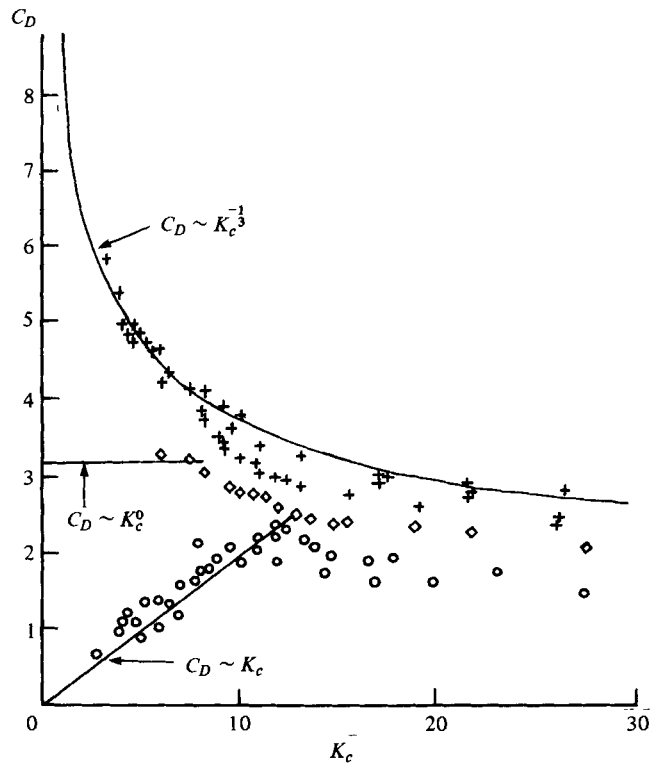

FIGURE 1. Drag coefficient at low Keulegan–Carpenter numbers. +, Flat plate (Singh 1979); ◇, square cylinder (Singh 1979); ○, circular cylinder (Sarpkaya 1975; Singh 1979).

very significant effect of Reynolds number on these coefficients, but Sarpkaya in a later paper (1976) reports a quite marked dependence for circular cylinders. Recently Maull & Milliner (1978) have also described measurements on circular cylinders and Bearman, Graham & Singh (1978) on various cylindrical bodies in U-tubes. Most of these experiments have been conducted over a range of Keulegan–Carpenter number from about 2 up to the order of 100. It is apparent from them and particularly from the flow visualization studies carried out by Singh (1979) that the whole Keulegan–Carpenter range contains two (at least) quite different flow régimes. In one régime, for $K_c > 20$ depending on the body, the flow past the body separates forming a limited wake in the flow direction containing a number of vortices staggered as in the von Kármán vortex street. The length of this wake and the resemblance of the flow to the corresponding steady free-stream situation grows with increasing Keulegan–Carpenter number. In the other régime, for $K_c <$ about 20, vortices are shed from the separation points on the cylinder but because of the relatively shorter amplitude of oscillation of the flow each is swept back past the body to form a pair with a successive vortex of opposite sign during the next half cycle. The resulting vortex pairs usually convect away from the body in directions at large angles (typically 45°) to the flow axis.

The in-line forces which arise in both régimes are usually expressed by Morison's equation, which with suitable values of the coefficients C_D and C_M gives fairly accurate predictions for averaged force cycles in the higher K_c régime. However, the predictions

are not so good in the lower K_c régime, particularly in the case of sharp-edged cylinders such as flat plates and diamond sections. Secondly the behaviour of the coefficients (particularly C_D) as $K_c \to 0$ is quite different for different cylinder cross-sections and differs significantly from the corresponding steady flow value. The two extreme cases are the normal flat plate for which $C_D \to \infty$ and the circular cylinder for which (neglecting eventual boundary-layer drag) $C_D \to 0$ as $K_c \to 0$, see figure 1. The differences appear to be due to the different behaviour and strength of the vortices shed by the various bodies.

Maull & Milliner (1978) have pointed out that there is no basis for the use of Morison's equation at these lower Keulegan–Carpenter numbers, since a quasi-steady drag generating wake does not occur. They have suggested that the force might more properly be calculated from the shed vortices through Blasius' equation

$$Z = -i\rho \frac{\partial}{\partial t} \oint_s W\,dz - \frac{i\rho}{2} \oint_s \left(\frac{dW}{dz}\right)^{*2} dz, \tag{2}$$

where Z is the complex force due to the complex potential W in the $z = x + iy$ plane, the integrals are taken round the perimeter s of the body, and * indicates a complex conjugate.

Substituting for W in the case of a circular cylinder gives

$$Z = \frac{\pi}{4}\rho C_{m_0} d^2 \dot{U} - i\rho \Sigma \frac{\partial}{\partial t}(\Gamma_n z_n), \tag{3}$$

where the sum is taken over all the point vortices Γ_n at z_n and their images in the cylinder. C_{m_0} is the value of the inertia coefficient for attached flow, in this case equal to 2·0. This formulation has the advantage of being linked to what is happening in the flow and also in providing a formula for the force transverse to the flow direction. This force (the lift) is frequently found to be as large as the in-line force. However equation (3) cannot be used to predict forces without further equations for Γ_n and z_n and Maull & Milliner have so far only used it qualitatively to explain the forces which arise under certain observed states of movement of the vortices. On the other hand it is well established that for small enough Keulegan–Carpenter number K_c the force on a body in oscillatory flow is entirely due to the attached flow inertia (C_{m_0}) component and the second term in equation (3) or its counterpart for other cylindrical sections is negligible owing to the absence, or weakness, of any shed vortices. In this paper we follow these suggestions of an alternative form of calculating the force from the complex potential due to distributed point vortices and attempt to provide a prediction, valid for small K_c, of the vortex force component F_v which should be added to the attached flow inertia component: thus

$$F = \tfrac{1}{4}\pi\rho C_{m_0} d^2 \dot{U} + F_v. \tag{4}$$

The method of calculating the force from a distribution of invisicid point vortices assumes that the flow can be represented adequately by an infinite-Reynolds-number approximation in which the effect of viscosity is negligible except as a cause of separation. The effect of separation at a sharp edge, which is independent of Reynolds number can be replaced by a Kutta–Joukowski condition, but in the case of separation from a continuous surface, such as a circular cylinder, further information is required to specify the separation point which may also change with time.

The method of representing separated vortex sheets by arrays of point vortices, or other forms of discretization, has been used recently to obtain numerical predictions of quite a large variety of different two-dimensional bluff body flows, as well as unsteady aerofoil and trailing vortex flows, (see e.g. Clements & Maull 1975). It has also been applied by Stansby (1977) to oscillatory flow past circular cylinders. However, in the present case, restricted to low Keulegan–Carpenter flows, it is possible to derive the power law dependence of the vortex force on K_c without carrying out the computation, which is only necessary if the constant of proportionality is required

2. Vortex shedding at low Keulegan–Carpenter number and flow scaling

When the Keulegan–Carpenter number is small, the maximum displacement of particles in the undisturbed flow is small compared with the scale of the body. It is therefore impossible for vortices to move far from the edge of the body from which they are shed except under the induced velocity field of other vortices, and shedding at each edge may become independent of the other edges.

The pattern of vortex shedding from a single isolated edge consists of one vortex pair shed per cycle. During the first part of the cycle separation of the stream passing the edge leads to the shedding of vorticity which rolls up in the expected sense behind the edge. As the free stream slows down, the flow round the edge reverses ahead of the free stream owing to the presence of the vortex. A second vortex is therefore shed and starts to grow on the other side of the edge. The first vortex is meanwhile swept round the edge by the reversed free stream. The two vortices thus form a pair and appear to convect away rapidly once the second vortex has reached an approximately equal and opposite strength to the first, since the path of the vortex pair is fairly straight with respect to the fluid. Since equalization of vorticity does not necessarily occur at the end of the second vortex period of growth, the pairing process splits the second vortex sheet leaving a smaller amount of residual vorticity to be engulfed by the next strong vortex. An example of this is shown in figure 2 (plate 1), in which polystyrene beads have been used as tracer particles. In the case of a body with two shedding edges at low Keulegan–Carpenter number, the above process which is asymmetric about the edge takes place in an anti-symmetric way about the two edges with the residual vorticity migrating from its own edge to join with a growing vortex of the same sign at the other edge. The process appears to revolve round the body either clockwise or anti-clockwise with vortex pairs being shed at about 45° to the line of flow. Singh (1979) has studied a number of such flows with two main edges shedding vortices and found that once such a pattern is established it remains fairly regular and stable over large numbers of flow cycles, But at the very lowest values of Keulegan–Carpenter number (and therefore correspondingly low Reynolds numbers for a given body) diffusion of the vortices into each other is so rapid that little or no convection of vortex pairs was seen.

The analysis which follows assumes that such a stable and regular process does occur, for Keulegan–Carpenter numbers below some value of order 10, depending on the body, right down to zero Keulegan–Carpenter number in the limit of vanishing viscosity.

As the Keulegan–Carpenter number becomes smaller, the ratio of the amplitude of the motion to the body scale, the diameter d say, decreases. Hence the size of the vortices and the characteristic length scale of the vortex shedding will also decrease in

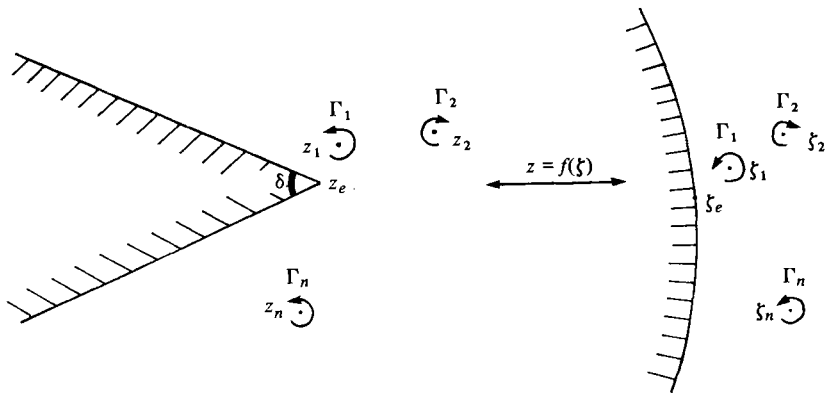

FIGURE. 3 An edge in the physical and transformed planes.

comparison with d until the process takes places in the neighbourhoods of the edges of the body. The flow therefore sees the body locally as if it were an infinite wedge subject to an oscillatory velocity U_e obtained by matching this inner edge region to the outer flow past the body.

We consider therefore a body as shown in figure 3 with one edge under consideration at z_e. A function

$$z = f(\zeta)$$

can be found which maps the body into the circle $\zeta = a\,e^{i\theta}$ with its centre at the origin of the ζ plane and with ζ_e corresponding to z_e. With a suitable choice of a, $df/d\zeta \to 1$ as $\zeta \to \infty$, so that the free stream is unchanged. We can therefore expand $f(\zeta)$ for large ζ as:

$$f(\zeta) = \zeta + b_0 + \sum_{n=1}^{\infty} b_n \zeta^{-n}. \tag{5}$$

Near $z_e = f(\zeta_e)$ the mapping opens out the edge, of angle δ say, into a continuous surface and can therefore be expanded as the series:

$$f(\zeta) = f(\zeta_e) + C_0(\zeta - \zeta_e)^{\lambda} + \sum_{n=1}^{\infty} C_n(\zeta - \zeta_e)^{\mu_n}, \tag{6}$$

where

$$\mu_n > \mu_{n-1} \ldots > \mu_1 > \lambda = 2 - \delta/\pi,$$

and the coefficient $C_0 \propto d^{1-\lambda}$.

The effect of the free stream U flowing round the edge at z_e is to cause a separation resulting in the shedding of a vortex sheet from z_e. We assume that this vortex sheet which rolls up into concentrated vortices can be represented in some way by point vortices or vortex elements Γ_m at $z_m = f(\zeta_m)$. The last Γ_m which is in the process of being shed from z_e is a function of time while the rest, assuming inviscid flow, are constant.

The complex potential W due to the flow round the body and the shed vortices in the circle plane is:

$$W(\zeta) = U(\zeta + a^2\zeta^{-1}) + \frac{i}{2\pi}\Sigma\Gamma_m \log(\zeta - \zeta_m) - \frac{i}{2\pi}\Sigma\Gamma_m \log(\zeta - a^2/\zeta_m^*).$$

The equation of motion of the vortex sheet, which is force free and therefore moves with the fluid is:

$$\frac{\partial z_n^*}{\partial t} = \frac{\partial W}{\partial z_n} \tag{7a}$$

at each point z_n of the sheet, where $\partial W/\partial z_n$ excludes the singularity due to the vortex element at z_n.

Therefore

$$\frac{\partial z_n^*}{\partial t} = \lim_{z \to z_n} \left\{ \frac{\partial W}{\partial \zeta} \cdot \frac{\partial \zeta}{\partial z} - \frac{i\Gamma_n}{2\pi(z - z_n)} \right\}.$$

This equation for finite $\partial z_n^*/\partial t$ includes the Kutta–Joukowski condition

$$\partial W/\partial \zeta = 0 \quad \text{at the edge} \quad \zeta = \zeta_e$$

since $\partial \zeta/\partial z$ is infinite at these points if $\delta < \pi$.

Substituting for $W(\zeta)$ and taking the limit:

$$\frac{\partial z_n^*}{\partial t} = \frac{\partial \zeta_n}{\partial z_n} \left\{ U(1 - a^2 \zeta_n^{-2}) + \frac{i}{2\pi} \sum_{m \neq n} \Gamma_m \left[\frac{1}{\zeta_n - \zeta_m} - \frac{1}{\zeta_n - a^2/\zeta_m^*} \right] \right\}$$
$$+ \frac{i\Gamma_n}{4\pi} \left\{ \frac{\partial^2 \zeta_n}{\partial z_n^2} \Big/ \frac{\partial \zeta_n}{\partial z_n} - 2 \frac{\partial \zeta_n}{\partial z_n} \Big/ (\zeta_n - a^2/\zeta_n^*) \right\}. \tag{7b}$$

This equation is for a point vortex representation of the sheet, whether by a multi-point array, or an isolated vortex representation. A similar equation involving the principal value of an integral (see for example, Pullin 1978) expresses the same condition for a continuous representation of the sheet.

Vortices whose strength is changing with time, such as the last vortex in the process of being shed or 'core vortices' used to represent the centre of a continuous spiral, satisfy a modified zero force equation (Rott 1956; Graham 1977):

$$\frac{\partial z_n^*}{\partial t} + \frac{1}{\Gamma_n} (z_n^* - z_s^*) \frac{\partial \Gamma_n}{\partial t} = \frac{\partial W}{\partial z_n}, \tag{7c}$$

where $z_n - z_s$ is the cut joining the vortex to the body or the rest of the sheet. Since however this equation is dimensionally the same as (7*a*) the conclusions for the latter apply equally to it.

In the case of flow round an infinite edge, no natural length scale is provided by the body. However a length scale can be obtained by considering, for example, the maximum attached flow velocity $U_e(L)$ at a distance L from the edge. Regarding the wedge flow as the inner region of an oscillatory flow past a finite body,

$$U_e(L) \propto U_0 C_0^{-1/\lambda} L^{1/\lambda - 1},$$

where U_0 is the amplitude of the free-stream velocity.

Therefore, if T' is the time scale of the flow, which we assume for the moment can be taken to be the period, then the length scale, on which L itself must scale is

$$U_0 C_0^{-1/\lambda} L^{1/\lambda - 1} T'.$$

Therefore $L \propto C_0^{-1/(2\lambda-1)} (U_0 T')^{\lambda/(2\lambda-1)}$, suggesting the following scaling for the vortices:

$$\Gamma_m(t) = (U_0 T')^{2\lambda/(2\lambda-1)} C_0^{-2/(2\lambda-1)} T'^{-1} g_m(t/T') \tag{8a}$$

and

$$z_m = z_e + C_0^{-1/(2\lambda-1)}(U_0 T)^{\lambda/(2\lambda-1)} s_m(t/T), \tag{8b}$$

g_m and s_m being dimensionless functions, or in the case of g_m constant for vortices already shed.

This scaling is similar to that deduced by Pullin (1978) for a self-similar vortex sheet shed from an infinite edge in unidirectional accelerating flow. The choice of scales made above can be justified for oscillatory flow past an infinite edge by substituting (8*a*) and (8*b*) into equation (7*b*) with $U(t) = U_0 \sin 2\pi t/T$, to give:

$$\frac{\partial s_n^*}{\partial \tau} = \frac{1}{\lambda s_n^{1-1/\lambda}} \left\{ (1 - e^{2i\phi_e}) \sin 2\pi\tau + \frac{i}{2\pi} \left[\sum_{m \neq n}^{\infty} g_m \left(\frac{1}{s_n^{1/\lambda} - s_m^{1/\lambda}} - \frac{1}{s_n^{1/\lambda} + e^{2i\phi_e} s_m^{*1/\lambda}} \right. \right. \right.$$
$$\left. \left. \left. + g_n \left(\frac{(1-\lambda)}{2 s_n^{1/\lambda}} - \frac{1}{s_n^{1/\lambda} + e^{2i\phi_e} s_n^{*1/\lambda}} \right) \right] \right\}, \tag{9}$$

where $\tau = t/T$, and $\phi_e = \arg(\zeta_e)$.

This result is exact for an infinite wedge flow. This may be imagined as a finite amplitude oscillatory flow past an infinitely large body (i.e. $K_c = 0$) at a finite time after the start so that no vortices have yet reached the outer flow region of the body, but are all still within the wedge type flow field.

The same scaling, but with the vortex sheet strength γ expressed as:

$$\gamma = (U_0 T)^{\lambda/(2\lambda-1)} C_0^{-1/(2\lambda-1)} T^{-1} \bar{g}(s, \tau)$$

can be substituted into the integral equivalent of equation (7) to give similarly a dimensionless equation for the evolution of a continuous representation of the vortex sheet. Applying the scaling to a wedge flow regarded now as the inner region of an oscillatory flow at low Keulegan–Carpenter number past a body of finite length scale d, gives to lowest order the same equation as equation (9), but contributions of higher order ($K_c^{1/(2\lambda-1)}$, $K_c^{(\mu_1-\lambda)/(2\lambda-1)}$ also arise from the effect of the finiteness of the body on the vortices and free stream in the vicinity of the edge. The ratio of d to the length scale L of the vortex shedding at the edge is proportional to $K_c^{-\lambda/(2\lambda-1)}$, therefore the smaller the Keulegan–Carpenter number, the more the shedding process takes place within the edge region. However in continuous oscillatory flow this process generates an infinite stream of vortices which convect out into the outer region of the body. It is therefore necessary to show that the effect of these on the similarity behaviour of the vortices in the inner region becomes negligible at small enough Keulegan–Carpenter numbers.

Let $|\partial z_n/\partial t|_M$ be the contribution to $\partial z_n/\partial t$ from vortices Γ_m where $m \geqslant M$ and the numbering is outwards from the edge. Then from equation (7*b*)

$$\left| \frac{\partial z_n^*}{\partial t} \right|_M = \frac{i}{2\pi} \frac{\partial \zeta_n}{\partial z_n} \sum_{m=M}^{\infty} \left[\frac{1}{\zeta_n - \zeta_m} - \frac{1}{\zeta_n - a^2/\zeta_m^*} \right]. \tag{10}$$

According to the assumptions made above about the vortex shedding when K_c is small, the vortices in the outer region are arranged in pairs with approximately equal and opposite circulation $\pm \Gamma$ and constant separation δz, one pair shed from each edge per flow cycle.

Therefore rewriting (10) as a sum of such pairs and substituting the inner region expansion (6) for ζ_n and the outer region one (5) for ζ_m gives:

$$\left| \frac{\partial s_n^*}{\partial \tau} \right|_M = \frac{i\Gamma}{2\pi\lambda U_0} \sum_{m=M}^{\infty} \left\{ \frac{\delta z}{z_m^2} + \frac{\delta z^*}{z_m^{*2}} e^{-2i\phi_e} + O\left(K_c^{1/(2\lambda-1)}, K_c^{\mu_1 - 1/(2\lambda-1)} \right) \right\}.$$

The convection speed of a vortex pair in the outer region is $\Gamma/2\pi|\delta z|$ to first order, so that

$$|z_m| \to mT\Gamma/2\pi|\delta z| \quad \text{as} \quad m \to \infty.$$

Therefore the leading terms in the series eventually decrease like $1/m^2$ giving a finite sum, and hence

$$\left|\frac{\partial s_n^*}{\partial \tau}\right|_M = O\left[\frac{\delta z^3}{U_0 \Gamma T^2 M}\right].$$

This is a small quantity for the range of low Keulegan–Carpenter numbers considered in the experiments. Although M was not large for these, being about 3, δz was observed to be much smaller than z_M. However, formally, in the limit $K_c \to 0$, $M = O(K^{-\lambda/(2\lambda-1)})$, the ratio of the body length scale to the vortex shedding length scale. Since both Γ and δz are generated in the inner region they scale as inner region variables. Therefore

$$|\partial s_n^*/\partial \tau|_M = O(K_c^{1/(2\lambda-1)}),$$

which indicates a negligible contribution to $\partial s_n^*/\partial \tau$ as $K_c \to 0$.

3. The force due to vortex shedding

The complex force Z induced on the body by the free stream and vortices can be written, by considering the rate of change of momentum across a circuit at infinity as

$$Z = -i\rho \frac{\partial}{\partial t}\left\{\oint_\infty W\,dz\right\}.$$

This equation can also be derived, as in the appendix, from Blasius equation applied to a system of force free vortices. Therefore expanding W and $dz/d\zeta$ for large ζ and using the residue theorem:

$$Z = 2\pi\rho \frac{\partial}{\partial t}\left\{(a^2 - b_1)\,U - \frac{i}{2\pi}\Sigma\Gamma_m(\zeta_m - a^2/\zeta_m^*)\right\}. \tag{11}$$

The first term in this expression is the force due to the inertia of the attached flow and is equal to $(\pi/4)\rho d^2 C_{m_0}\dot{U}$.

The second term is the vortex force.

$$Z_v = -i\rho \frac{\partial}{\partial t}\{\Sigma\Gamma_m(\zeta_m - a^2/\zeta_m^*)\}.$$

Substituting the inner region similarity expressions into this gives:

$$Z_v = -i\rho(U_0 T^{(2\lambda+1)/(2\lambda-1)} C_0^{-4/(2\lambda-1)} T^{-2} \frac{\partial}{\partial \tau} \sum^{M-1} \{g_m(\tau)\,[s_m^{1/\lambda}(\tau) + e^{2i\phi_e} s_m^{*1/\lambda}(\tau)] + O(K_c^{1/(2\lambda-1)}, K_c^{(\mu_1-\lambda)/(2\lambda-1)})\} + Zv_M \tag{12}$$

where, as before,

$$Zv_M = -i\rho \sum_{m=M}^{\infty} \Gamma_m(\partial/\partial t)\,(\zeta_m - a^2/\zeta_m^*)$$

is the contribution to Z_v from the vortices which have been convected out of the inner regions. Using the same argument as before and summing the vortices in pairs, Zv_M

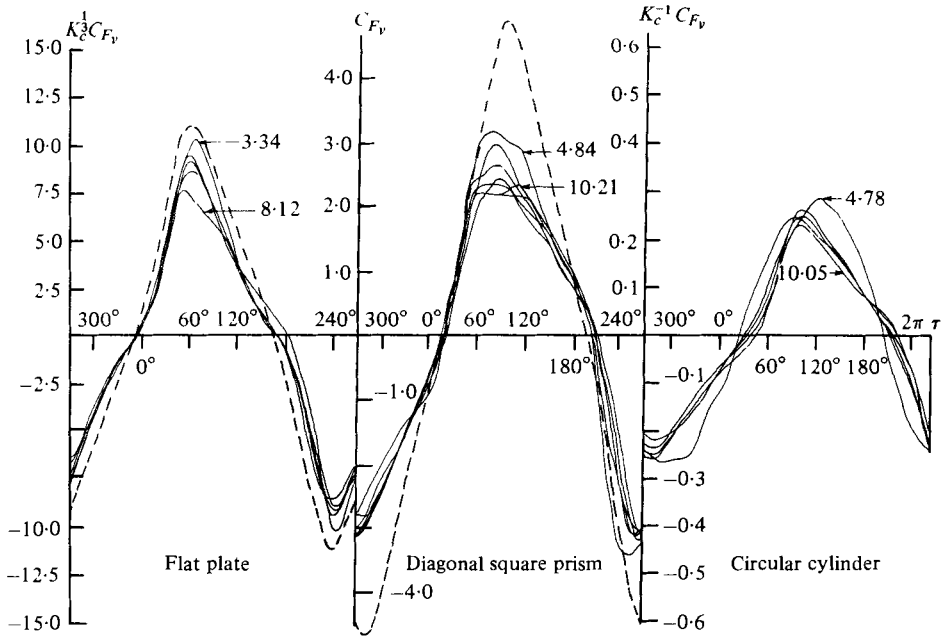

FIGURE 4. The non-dimensionalized vortex force. ——, Measured (maximum and minimum K_c values given); – – –, computed ($K_c = 0$).

is a finite sum whose ratio to the lowest order terms of Z_v is $O(K_c^{(\lambda-1)/(2\lambda-1)})$. Hence the contribution of the vortices being convected as pairs away from the edges to the overall force on the body is negligible in the limit $K_c \to 0$ except in the case when $\lambda = 1$ (the circular cylinder). The lowest order terms contributing to Z_v represent a force acting parallel to the tangent to the surface at ζ_e in the ζ plane, since $\phi_e = \arg(\zeta_e)$. Therefore in the z plane, Z_v acts at right angles to the bisector of the edge angle. For most common cylindrical bluff bodies all the edges shedding vortices have the same internal angle δ with the bisector making a non-zero angle to the free stream so that the analysis derived above for each edge separately can be applied to the overall in-line force on the body.

Vortices close to other parts of the body but far, in terms of the inner region length scale from the edge under consideration are sensed as vortex pairs in the neighbourhood of the edge, because of the effect of their images in the body, and hence may be treated like the other far field vortex pairs. Therefore, neglecting the higher-order contributions to Z_v as $K_c \to 0$ and defining the in-line vortex force coefficient as:

$$C_{F_v} = F_v / \tfrac{1}{2}\rho U_0^2 d,$$

where $U = U_0 \sin(2\pi t/T)$ for oscillatory flow, we obtain

$$C_{F_v} = K_c^{(3-2\lambda)/(2\lambda-1)} \psi(t/T),$$

where ψ is a dimensionless function. This implies a force equation for low Keulegan–Carpenter number flows of the form

$$F = \tfrac{1}{4}\pi\rho d^2 \dot{U} C_{m_0} + \tfrac{1}{2}\rho U_0^2 d K_c^{(3-2\lambda)/(2\lambda-1)} \psi(t/T) \tag{13}$$

instead of Morison's equation (1).

The result can be tested by subtracting the known attached flow inertia component from the in-line force and suitably non-dimensionalizing the remainder. Average cycle† measurements taken in a U-tube on flat plate, square diamond and circular cylinders at different values of K_c below about 10 are shown plotted as the function $\psi(t/T)$ in figure 4. Division by the Keulegan–Carpenter factor ($K_c^{-\frac{1}{3}}$ for the flat plate, K_c^0 for the square and K_c^1 for the circle) implied by equation (13) does produce quite a good collapse of the data in all three cases. A fourth body, a square section with one face normal to the flow, was also measured but did not show such a good collapse when treated in this way. The reason for this is not yet known, but it is thought that because of interference between all four edges which shed at different times in the cycle the smallest value of K_c tested (about 6) may not have been sufficiently low for the theory to apply. In addition the vortices appeared to be very weak in this case leading to considerable inaccuracy in the measurement of C_{F_v}. In the cases shown in figure 4 it is notable that the variation of the vortex force with time is quite similar for all three bodies although there are large differences in amplitude and phase. This suggests that a similar vortex shedding process may occur for all three bodies at low Keulegan–Carpenter number. The analysis given above does not strictly apply to the circular cylinder for the reason that the influence of the far field vortices cannot be shown formally to disappear as $K_c \to 0$ and the separation points are known to move during a flow cycle. However, the experimental results show as good agreement for this case as for the others.

4. Calculation of the vortex force and drag coefficients

The implication of equation (13) is that the drag coefficient C_D in Morison's equation should vary as $K_c^{(3-2\lambda)/(2\lambda-1)}$. Figure 1 shows appropriate theoretical curves varying as $K_c^{-\frac{1}{3}}$ (flat plate), K_c^0 (diamond) and K_c (circle) which do agree with the trends of the measured data at low K_c. Shih & Buchanan (1971) who analysed quite a lot of their own and Keulegan & Carpenter's flat plate data concluded empirically that C_D varied as $K_c^{-\frac{1}{2}}$. Because of the small differences between the $K_c^{-\frac{1}{2}}$ and $K_c^{-\frac{1}{3}}$ curves and the large scatter of the data at low K_c, where the inertia term is tending to predominate, it is not possible on the basis of analysing the data alone to be sure which is correct.

In order to obtain actual predicted values of C_D and C_{F_v} a full vortex calculation is required. A possible way of doing this is to follow the work of Rott (1956) and use a concentrated vortex model in the unsteady flow situation. There are some problems however in correctly modelling the splitting of the vortex sheet which this method does not predict naturally. If the computation is allowed to run with a new vortex shed from an edge each time the vortex shedding rate changes sign at the edge, the vortex strengths continue to increase and the calculation is divergent. An alternative is to use the point vortex array method to represent each vortex sheet. In this method point vortices are shed sequentially from the edge and then tracked as they move with the fluid particles. Groups of vortices which can be identified as representing completely rolled up sheets far from the body are progressively rolled into a central core vortex. A method of shedding the vortices from the edge so that they represent a continuous sheet in that neighbourhood is described in Graham (1977).

† The average of 40 consecutive cycles.

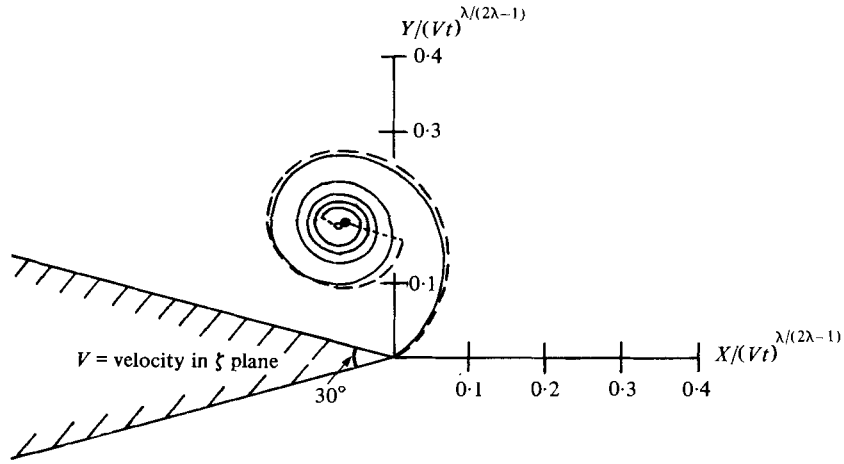

FIGURE 5. Calculated vortex sheets under a uniform acceleration. ——, sheet plus core vortex, Pullin (1978), $\Gamma t/(Vt)^{2\lambda/(2\lambda-1)} = 1{\cdot}43$; – – –, sheet plus core vortex, present calculation, $\Gamma t/(Vt)^{2\lambda/(2\lambda-1)} = 1{\cdot}45$.

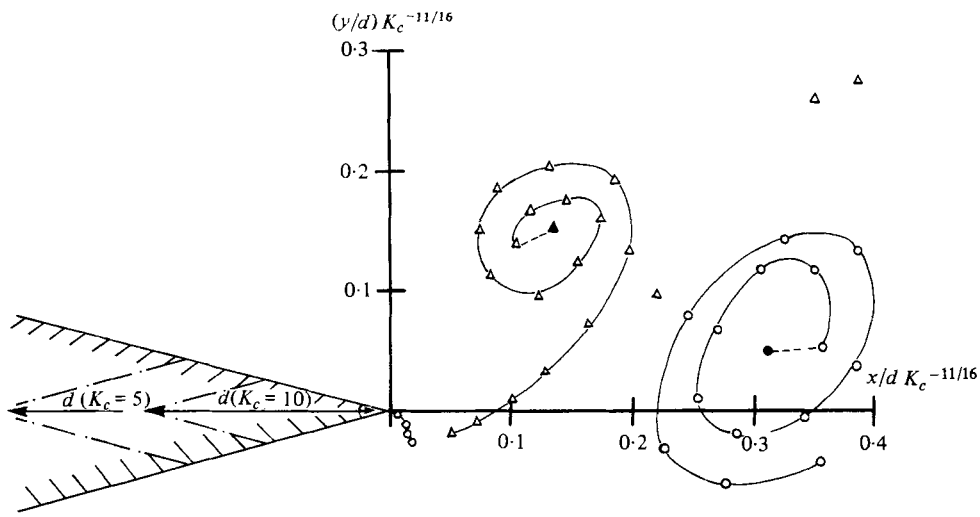

FIGURE 6. Calculated vortex shedding in oscillatory flow.

Using this method and the dimensionless equations (9) and (12) it is possible to compute the vortex development and forces induced by oscillatory flow past an infinite wedge. At small times after the start a single rolling up vortex sheet is shed from the edge under effectively constant acceleration and the flow field corresponds to the self-similar vortex flows studied by Pullin (1978). Figure 5 shows a comparison of the resulting sheet and vortex strength for a 30° edge with Pullin's results. At larger times a succession of rolling up vortex sheets is formed which convect away as shown in figure 6. This computation also for a 30° edge compares quite well with the flow visualization of the same situation shown in figure 2 taken at approximately the same time in the flow cycle. Such a flow corresponds to oscillatory flow past, for example, a diamond cylinder with two thirty degree edges across the flow in the limit of zero

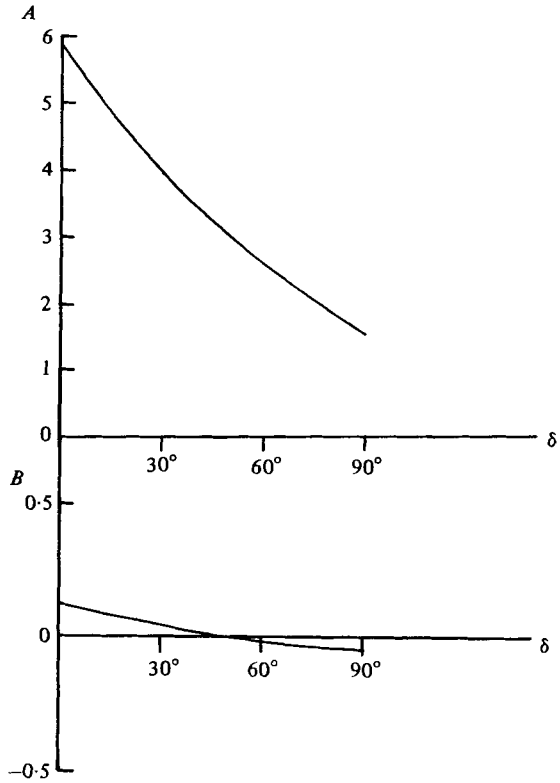

FIGURE 7. Variation of the coefficients A and B with edge angle for a single edge.

Keulegan–Carpenter number. At small, but non-zero values of K_c the length scale of the flow is related to the diameter d of the body through the appropriate power of K_c as indicated on the axes of figure 6. Using these scales the apparent body size varies with K_c as shown and it can be seen that the size of the shed vortices is such that the hypothesis of mutual independence of the two shedding edges is unlikely to hold for K_c much greater than about 5.

The vortex force function $\psi(t/T)$ of equation (13) as predicted by this computation averaged over 5 cycles of the flow is shown as a dashed line in figure 4 for the flat plate ($\delta = 0$) and square ($\delta = 90°$). It is not possible to extend this to the case of the circular cylinder because this discrete vortex method ceases to give a representative shedding pattern for edge angles greater than about 120°. However for edge angles less than this the computation predicts decreasing magnitude and increasing phase lag of the force on the edge as the edge angle increases. The results can be translated into drag and inertia coefficients by taking the appropriate Fourier integral of (13) over one cycle of the flow to give

$$C_D = AK_c^{(3-2\lambda)/(2\lambda-1)} \quad \text{where} \quad A = \frac{3\pi}{4}\int_0^1 \psi(\tau)\sin 2\pi\tau\, d\tau$$

and

$$C_m = C_{m_0} + BK_c^{2/(2\lambda-1)} \quad \text{where} \quad B = \frac{2}{\pi^2}\int_0^1 \psi(\tau)\cos 2\pi\tau\, d\tau.$$

	Plate δ 0°	Square 90°	Circle 180°
A (experimental)	8·0	3·2	0·2
A (theoretical)	11·8	5·7	—
B (experimental)	0·2	−0·055	−0·01
B (theoretical)	0·25	−0·19	—

TABLE 1. Coefficients A and B

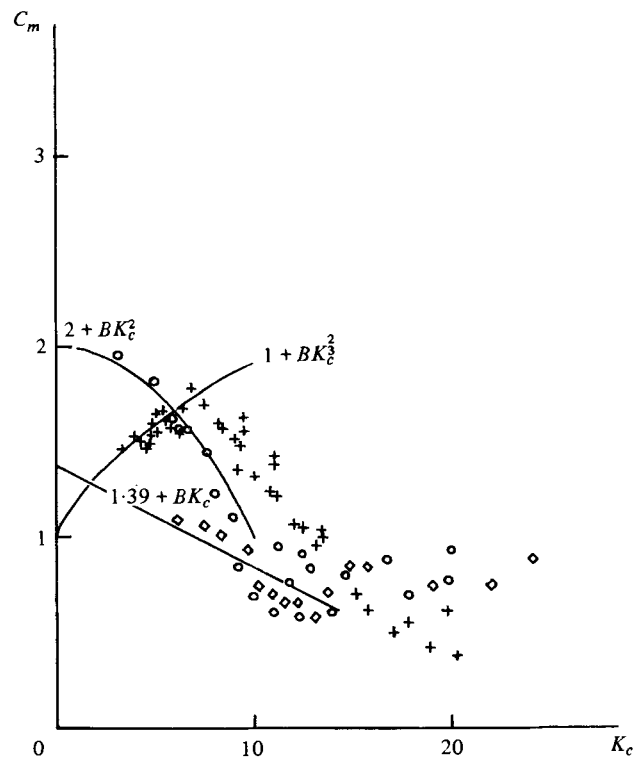

FIGURE 8. Inertia coefficients at low Keulegan–Carpenter numbers. +, Flat plate (Singh 1979); ◇, diamond square (Singh 1979); ○, circular cylinder (Singh 1979).

The coefficients A and B for the infinite wedge are plotted against the wedge angle δ in figure 7 which shows that the increasing phase lag leads to a change of sign of the vortex induced part of the inertia coefficient at $\delta \simeq 50°$. Inertia coefficients measured on plates, square and circular cylinders by Singh (1979) show that this part does change sign between $\delta = 0°$ (flat plate) and $\delta = 90°$ (square cylinder), as shown in figure 8. The coefficients A and B for the flat plate and square cylinder obtained by using the wedge flow results for each edge with the appropriate outer velocity are shown in table 1. The results for the flat plate are in moderate agreement with experiment but considerably overestimated for the square.

The analysis has been derived under the assumption that while the Keulegan–Carpenter number $U_0 T/d$ was arbitrarily small, the Reynolds number $U_0 d/\nu$ remained sufficiently large for an inviscid analysis to be valid. This therefore requires that the

β parameter (Sarpkaya 1975) ($= d^2/\nu T$) must tend to infinity as K_c tends to zero. In many practical cases, such as U-tubes, bodies oscillating at a structural frequency, wave flows and so on, the time period T is of a fixed order of magnitude, and hence so is the β parameter, for a given body and fluid. For these therefore there will also be a lower limit on K_c below which viscous effects become important.

There is some evidence from visualization studies of the flow past different sizes of flat plates in a U-tube that the mechanism of vortex shedding through pairing starts to break down at low Reynolds numbers. In this case the vortices diffuse so rapidly with consequent mixing that each succeeding vortex appears to engulf its predecessor from the same edge, so that no vortices escape from the neighbourhood of the edge.

Shih & Buchanan (1971) in their work on flat plates similarly found a dependence on Reynolds number at very low values of the latter.

5. Conclusions

The vortex force and drag coefficients of cylinders in oscillatory flow have been shown to be proportional to $K_c^{(3-2\lambda)/(2\lambda-1)}$ where K_c is the Keulegan–Carpenter number and $\lambda = 2 - \delta/\pi$ depends on the internal angle δ of the edge of the body at the separation points. Some discrete vortex calculations have been carried out to obtain the constants of proportionality and to predict flow patterns, which are compared with measurements taken in U-tubes.

The author would like to thank Dr S. Singh for the use of his experimental results in this report. This work was supported by the Science Research Council as part of their Marine Technology Research programme.

Appendix

To show that

$$-i\rho\frac{\partial}{\partial t}\oint_S W\,dz - \frac{i\rho}{2}\oint_S \left(\frac{dW}{dz}\right)^{*2} dz = -i\rho\frac{\partial}{\partial t}\oint_\infty W\,dz, \tag{A 1}$$

where the integrals on the left-hand side are taken round the perimeter S of the body, and on the right-hand side round a circuit at infinity.

Suppose the flow contains vortices Γ_n at the finite points z_n with 'image' circulation $-\Gamma_n$ in the body. Then as $z \to \infty$

$$dW/dz \to U_\infty + O(1/z^2),$$

since the sum of all the vortices and images in the field must be zero. Therefore

$$\oint_\infty \left(\frac{\partial W}{\partial z}\right)^2 dz = \oint_\infty \left\{U_\infty^2 + O\left(\frac{1}{z^2}\right)\right\} dz = 0 \quad \text{by the residue theorem.}$$

The circuit at infinity can be shrunk to the circuit S plus the circuits S_n round each vortex Γ_n and the cuts C_n joining each vortex to the edge from which it was shed, as shown in figure 9. The result (A 1) is therefore proved if

$$-\Sigma\oint_{S_n+C_n} \frac{1}{2}\left(\frac{\partial W}{\partial z}\right)^{*2} dz = \Sigma\frac{\partial}{\partial t}\oint_{S_n+C_n} W\,dz, \tag{A 2}$$

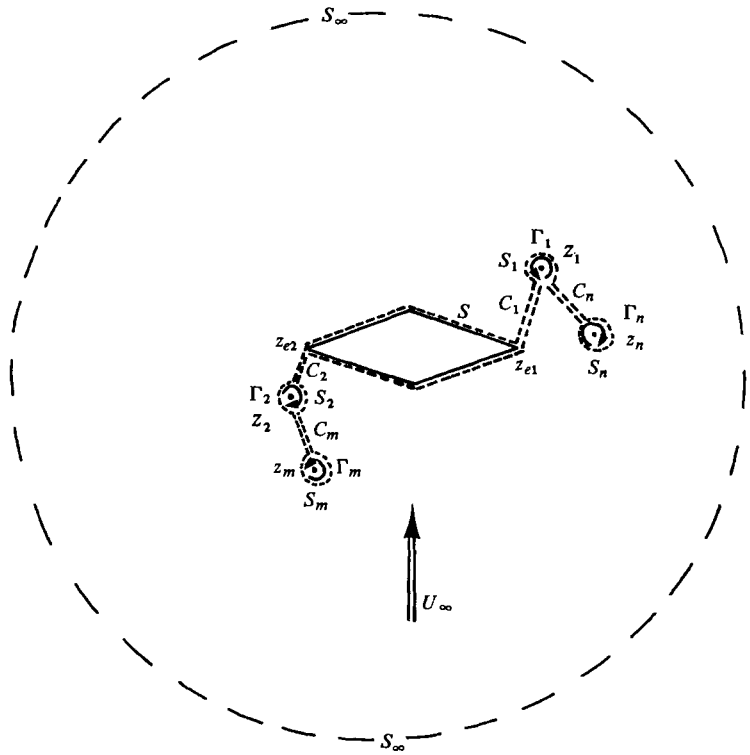

FIGURE 9. Integration circuits for the force.

(dW/dz) is continuous across C_n, therefore

$$\oint_{C_n} \left(\frac{dW}{dz}\right)^{*2} dz = 0.$$

Close to z_n,

$$W = \frac{i\Gamma_n}{2\pi} \log (z - z_n) + q_n z + \sum_{m=0}^{\infty} p_{nm} z^{-m}.$$

Therefore

$$\oint_{S_n} W\, dz = 0, \quad -\oint_{S_n} \frac{1}{2}\left(\frac{dW}{dz}\right)^{*2} dz = -\Gamma_n q_n,$$

and

$$\oint_{C_n} W\, dz = \Gamma_n (z_n - z_e)$$

owing to the jump in W across the cut.

However q_n is the velocity at the point z_n owing to the rest of the flow field, so that, since the vortex Γ_n if shed is free, or if still growing has zero force on itself plus the cut joining it to its edge z_e [see equation (7*c*)], we have:

$$\frac{\partial}{\partial t}\{\Gamma_n (z_n - z_e)\} = \Gamma_n q_n, \quad \text{since } z_e \text{ is a fixed point.}$$

Therefore (A 2) is true for every n and the result is proved.

REFERENCES

BEARMAN, P. W., GRAHAM, J. M. R. & SINGH, S. 1978 Forces on cylinders in harmonically oscillating flow. *Sym. on Mechs. of Wave Induced Forces on Cylinders*. Bristol.

CLEMENTS, R. R. & MAULL, D. J. 1975 The representation of sheets of vorticity by discrete vortices. *Prog. Aerospace Sci.* **16**, 129.

GRAHAM, J. M. R. 1977 Vortex shedding from sharp edges. *Imperial College Aero. Rep.* 77–06.

KEULEGAN, G. H. & CARPENTER, L. H. 1958 Forces on cylinders and plates in an oscillating fluid. *J. Research N.B.S.* **60**, 423.

MAULL, D. J. & MILLINER, M. G. 1978 Sinusoidal flow past a circular cylinder. *Coastal Engng* **2**, 149.

PULLIN, D. I. 1978 The large scale structure of unsteady self-similar rolled up vortex sheets. *J. Fluid Mech.* **88**, 401.

ROTT, N. 1956 Diffraction of a weak shock with vortex generation. *J. Fluid Mech.* **1**, 111.

SARPKAYA, T. 1975 Forces on cylinders and spheres in a sinusoidally oscillating fluid. *Trans. A.S.M.E.* E, *J. Appl. Mech.* **42**, 32.

SARPKAYA, T. 1976 In-line and transverse forces on smooth and sand-roughened cylinders in oscillatory flow at high Reynolds number. *Naval Postgraduate School, Monterey, Calif.*, NPS-69SL-76062.

SHIH, C. C. & BUCHANAN, H. J. 1971 The drag on oscillating flat plates in liquids at low Reynolds numbers. *J. Fluid Mech.* **48**, 229.

SINGH, S. 1979 Forces on bodies in oscillatory flow. Ph.D. thesis University of London.

STANSBY, P. K. 1977 An inviscid model of vortex shedding from a circular cylinder in steady and oscillatory far flows. *Proc. Inst. Civ. Eng.* **63**, 865.

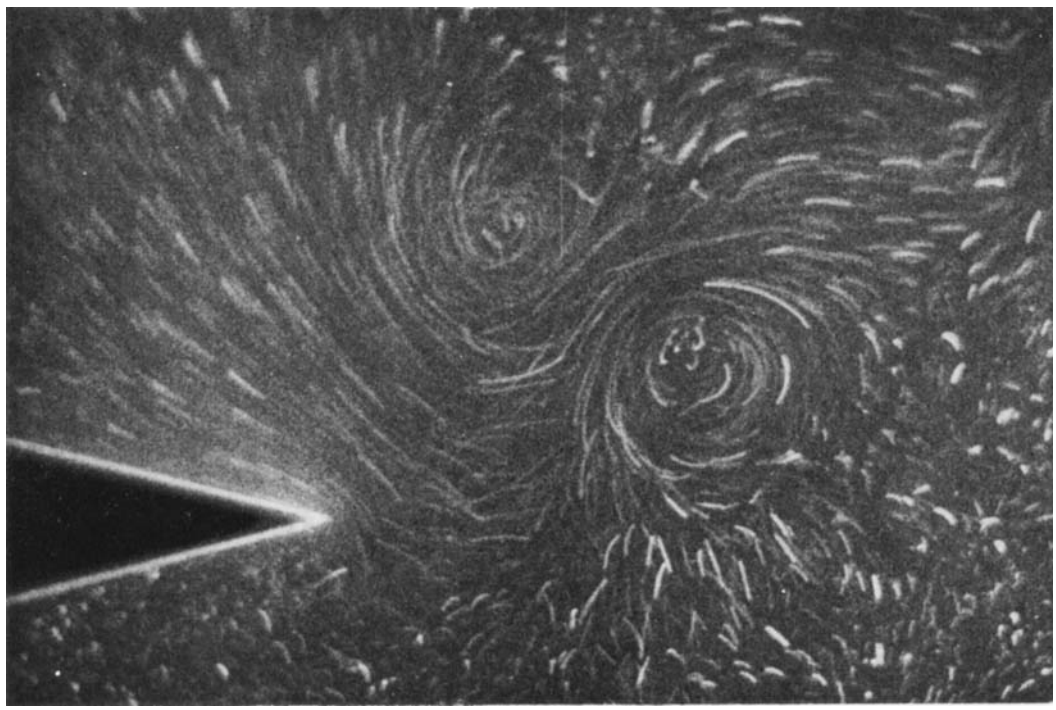

FIGURE 2.

J. Fluid Mech. (1980), *vol.* 97, *part* 2, *pp.* 347–384
Printed in Great Britain

Unsteady laminar separation: an experimental study

By C. A. KOROMILAS AND D. P. TELIONIS
Virginia Polytechnic Institute and State University, Blacksburg, Virginia, U.S.A.

(Received 22 September 1978 and in revised form 16 February 1979)

The design of most aerodynamic surfaces, as for example the helicopter rotor, is based essentially on quasi-steady theories. However, the dynamics of a rotating blade introduce unexpected fluctuations and overshoots of properties like lift, drag, etc. The phenomenon of unsteady stall is intimately connected with the development of an oscillating boundary layer and separation. Experimental investigation of such flows was undertaken by a method of visualization developed especially for the study of laminar or turbulent boundary layers and separation. The method captures the instantaneous two-dimensional flow field, including regions of separated flow, and provides accurate quantitative information. Laser-doppler anemometer measurements complement the optically obtained data. Results reveal that separation responds with time-lag to external disturbances, in agreement with unsteady stall data. Oscillating outer flows result in displacement of the point of separation and, under certain conditions, the Despard & Miller (1971) criterion was found to hold. Earlier theoretical models of separation are confirmed qualitatively and for the early stages of the transient phenomena. The findings provide physical insight and quantitative data that may help explain the phenomenon of unsteady stall and unsteady separation.

1. Introduction

Potential-flow theory has been an invaluable tool for the designer in a variety of engineering applications of aerodynamics. It is well known, however, that this has been possible only via appropriate heuristic assumptions, as for example the Kutta–Joukowski condition, which arbitrarily model the catalytic role played by viscosity. Alternatively, potential theory may be supplemented with a boundary-layer calculation. Today it is widely accepted that viscous effects, although very often confined to small areas, control and regulate basic features of the flow field as, for example, circulation. As a result, aerodynamic characteristics of significant engineering importance, like lift and drag, depend on the development of a viscous layer and its downstream fate which may or may not experience transition to turbulence and separation to a wake.

In unsteady aerodynamics viscosity has again reserved for us some unexpected surprises. It is the agent responsible for phenomena that cannot be predicted or explained with potential theory and quasi-steady viscous models. Some typical examples are: dynamic stall of lifting surfaces; stall flutter of helicopter rotor blades; rotating stall in engine compressor blades; etc. Most of such phenomena can be attributed to the nonlinear character of the viscous layers that generate space and time phase differences, nonlinear steady streaming, separation delay, viscous damping, etc.

0022-1120/80/4403-8670 $02.00

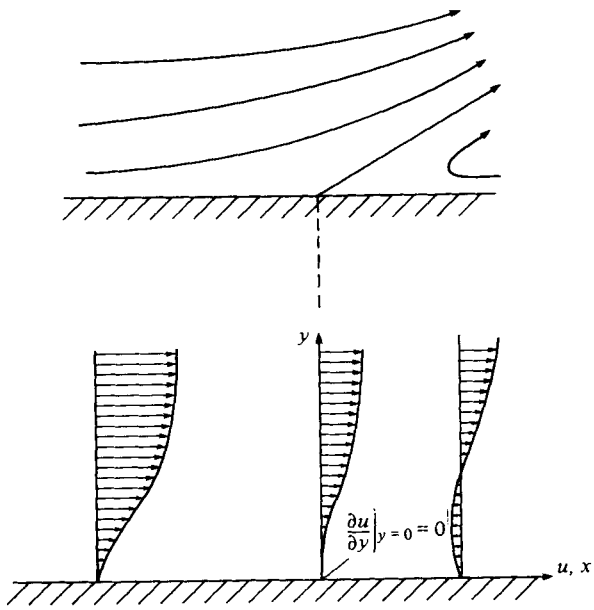

FIGURE 1. Separation over a fixed wall.

Some of the most spectacular dynamic effects that clearly demonstrate the futility of quasi-steady solutions are connected with unsteady separation. Experimental evidence has indicated, for example, that the stalling characteristics of airfoils in unsteady flow deviate substantially from the quasi-steady case. The phenomenon is well known in literature as 'unsteady stall' and is due to the fact that, for an abrupt increase of the angle of attack, the upstream propagation of separation appears to be delayed by some finite time-lag. As a result, the airfoil remains unstalled for a while, at angles of attack that are well beyond the static stall angle of attack.

Separation is usually defined in aerodynamics as the breakaway of the flow from a bounding surface and the initiation of a wake. For the case of steady two-dimensional or axisymmetric flow over fixed walls, a criterion for separation was suggested by Prandtl (1904) (see figure 1)

$$\partial u/\partial y = 0 \quad \text{at} \quad y = 0, \tag{1}$$

where u is the velocity component parallel to the wall and y is the co-ordinate perpendicular to the wall. This criterion proved to predict the phenomenon correctly and it has been used extensively by both theoreticians and experimentalists for over fifty years. However, Sears (1956), Moore (1958) and Rott (1956, 1964) demonstrated that Prandtl's criterion is inadequate for cases other than steady flow over fixed walls and indicated the need for a generalized definition and a convenient criterion for separation. They also suggested independently a more appropriate criterion for the case of steady flow over moving walls, namely (figure 2)

$$\partial u/\partial y = 0 \quad \text{at} \quad u = 0. \tag{2}$$

Sears (1956) and Moore (1958) proposed a definition of unsteady separation which is essentially equivalent to the condition expressed in a co-ordinate system moving with the point of separation. Sears suggested that, in unsteady flow, separation is 'the

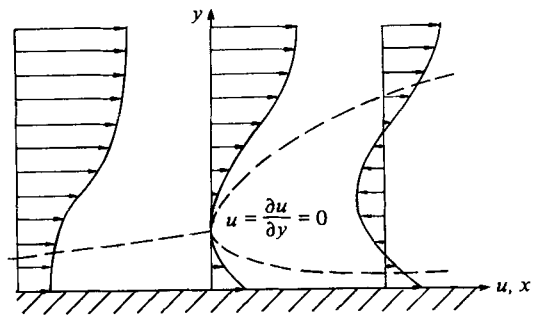

FIGURE 2. Separation over a downstream moving wall. Dashed lines represent streamlines.

appearance of a stagnation point and a dividing flow trajectory between boundary-layer and wake fluids in the flow seen by an observer moving with the separation point'. In the work that followed and is briefly described below, the criterion given by equation (2) and subsequently its extension to unsteady flow in the spirit of Sears' definition are referred to as the MRS criterion, after Moore, Rott and Sears.

Vidal (1959) and later Ludwig (1964) initiated the experimental work with a cylinder rotating in the test section of a wind tunnel. Using hot-wire anemometers, they were able to verify the theoretical model of equation (2), at least for the case of downstream moving walls. Tennant and his associates (Tennant 1973; Tennant & Yang 1973) also performed experiments with moving boundaries for both laminar and turbulent flow. Their findings pertain to skin velocities much larger than the free stream and always downstream motion of the skin. Despard & Miller (1971) again, inspired by the analytical work of Moore (1958) for laminar flow and the experimental work of Sandborn (1968) for turbulent flow, considered the problem of an oscillating outer-flow velocity and proposed a definition for a mean location of separation. Working with air and using hot-wire anemometers, they were also able to verify that in unsteady flow the location of zero skin friction is not necessarily related to the phenomenon of separation. In a very recent effort, Simpson (1977) and Kenison (1977) investigated experimentally the neighbourhood of separation of an oscillating turbulent boundary layer. Kenison reports that, as separation is approached, fluctuating velocity overshoots and phase angles indicate sharp changes. However, the basic features of oscillating turbulent separation are similar to those of laminar separation.

The work of Vidal and Ludwig pertains only to steady flow and the work of Despard & Miller is confined to oscillatory flows with high frequencies and Reynolds numbers. Our knowledge, therefore, about this complex phenomenon is remarkably narrow and urgently in need of more experimental investigation. This can be accomplished both by methods of flow visualization and by hot-wire or laser anemometry techniques. Visualization methods were employed by Schraub *et al.* (1965), Wérlé (1973), Ruiter, Nagib & Fejer (1971), McCroskey (1971) and McAlister & Carr (1978) to study unsteady viscous flow phenomena, but the specific cases considered and the scale of the models were designed for a study of the entire flow field. There was no emphasis on the features of the unsteady boundary layer and in particular separation.

In a recent effort Carr, McAlister & McCroskey (1977) employed a variety of sensing devices ranging from flow-visualization methods (tufts, smoke) to pressure- and

velocity-measuring methods (pressure transducers, hot-wire anemometers, etc.) to study the phenomenon of unsteady stall. In this study some basic features of unsteady separation were verified. In particular, pressure and velocity signatures throughout a period of oscillation were given for different stations on the airfoil and compared with flow-visualization data. A more complete account of this work is reported by McAlister, Carr & McCroskey (1978) who also present estimates of the unsteady drag force and the characteristics of the pressure response which are intimately connected with unsteady separation and symptomatic of the occurrence severity of moment stall.

Telionis & Werle (1973) showed numerically that, for steady boundary-layer flow over moving walls, the location of zero skin friction is non-singular, while a typical separation singularity appears at the station where Moore, Rott and Sears predict separation. A substantial number of analytical investigations on the topic have already appeared as reviewed by Sears & Telionis (1975) and Williams (1977). Of great interest to theoreticians should be the contributions of Williams and Shen, and their associates (Williams 1978; Shen 1978). The first author introduces semi-similar solutions and the second employs a Lagrangian approach. However, the available experimental data up to now is inadequate to validate the theoretical models of unsteady separation.

An experimental study of unsteady separation was undertaken a few years ago at VPI & SU. This is the first complete report of the experimental findings. The work was confined essentially to laminar flows. All the facilities described here were constructed especially for this project. These are: an open channel, a small water tunnel with a free surface and a medium speed water tunnel. Flow visualization was accomplished by dispersion of solid particles with density very close to the density of water. The method developed and described in this report can capture approximately the instantaneous velocity field. Boundary-layer velocity profiles were obtained in this manner for transient and oscillatory velocity fields. Glycerol–water mixtures were used to achieve low-Reynolds-number flows with measurable magnitudes of velocity.

In early visualization studies of separation attempts were made to generate information about the whole flow field. As a result, the details and the mechanism of unsteady separation were not adequately revealed. In the present study, special effort is directed towards the amplification of the neighbourhood of separation. In most of the flows visualized the frame of visualization is of the same order of magnitude as the boundary-layer thickness. Except for the work of Despard & Miller (1971), quantitative boundary-layer data in the neighbourhood of unsteady laminar separation are presented here for the first time. Despard & Miller concentrated on oscillatory flows. In the present report we compare our data with those of Despard & Miller and reconfirm the validity of their definition for separation in oscillatory laminar boundary layers. The present study proceeds further in the area of transient and impulsive flows to provide data that may appear useful to numerical analysts.

Numerous difficulties were encountered in the design of the facilities and the appropriate models to exhibit the dynamic characteristics of separation encountered in common aeronautical applications. Moreover it is a very difficult task for experimentalists to investigate phenomena described earlier by theoreticians. The present results shed some more light on the problem, revealing, indeed, some features of the flow that were predicted theoretically but also indicating the need to reconsider and

reframe the theory. This report includes only a small representative portion of the data obtained throughout the period of the last few years. Reduction and interpretation of the data is presented here as well. However, it is very possible that alternative interpretations may be offered which may in fact prove eventually to be more reasonable.

2. Steady flows over moving walls

The experimental evidence up to now seem to support the MRS criterion [equation (2)] at least for the case of a downstream moving wall. However, the saddle-point-streamline pattern suggested by Moore, Rott and Sears has not been verified analytically. This is because the wake is turbulent for moderate Reynolds numbers. The experimental information of Vidal (1959) and Ludwig (1964) and the analytical results of Telionis & Wérlé (1973) cover the region upstream of separation only. In this section we report on our experimental efforts to visualize streamline patterns in the neighbourhood of separation over downstream and upstream moving walls. 'Saddlepoint' patterns are captured for the first time. Some interesting new information is also disclosed about the overall validity of the MRS criterion in the case of an upstream moving wall. This work was performed in an open channel designed and constructed especially for this project.

The flows considered here are steady. However there is a very strong similarity between steady separation over moving walls and unsteady separation over fixed walls as Moore (1958) and Sears (1956) have pointed out. A convincing analytical argument and a comprehensive account of all other evidence on this point is included in a recent review article (Williams 1977).

The open channel

Open-channel-flow facilities offer some distinct advantages over closed tunnels, essentially because it is very convenient to insert and secure the models in the proper position. In our case the models or other auxiliary equipment are required to perform some type of dynamic motion, and this is particularly difficult to achieve in water tunnels. The open facility appeared further to be very attractive in the initial phase of our project, when a large number of models and shapes had to be tested until the optimum combination could be chosen.

The flow is driven in this facility by a centrifugal pump (Fairbanks, Morse Co., 1160 r.p.m., $4''\phi$) which discharges into an 18 cm diameter plastic pipe (see figure 3). This pump is certainly not ideal for such a facility because it generates an unwanted head, but it was available in the Engineering Science and Mechanics shop and its use appeared satisfactory for the initial steps of this work. Artificial head losses were provided by a valve connected at the discharge of the pump. The pipe directs the flow into an open container where perforated sheets and screens eliminate the large-scale vorticity. After a small converging section, the flow goes through a honeycomb and into the test section, which is an open rectangular section 47×31 cm.

Models were inserted in the middle of the open section and the flow was visualized at the free surface or in horizontal planes beneath the free surface. Surface-flow visualization is straightforward and does not require any special lighting facilities or

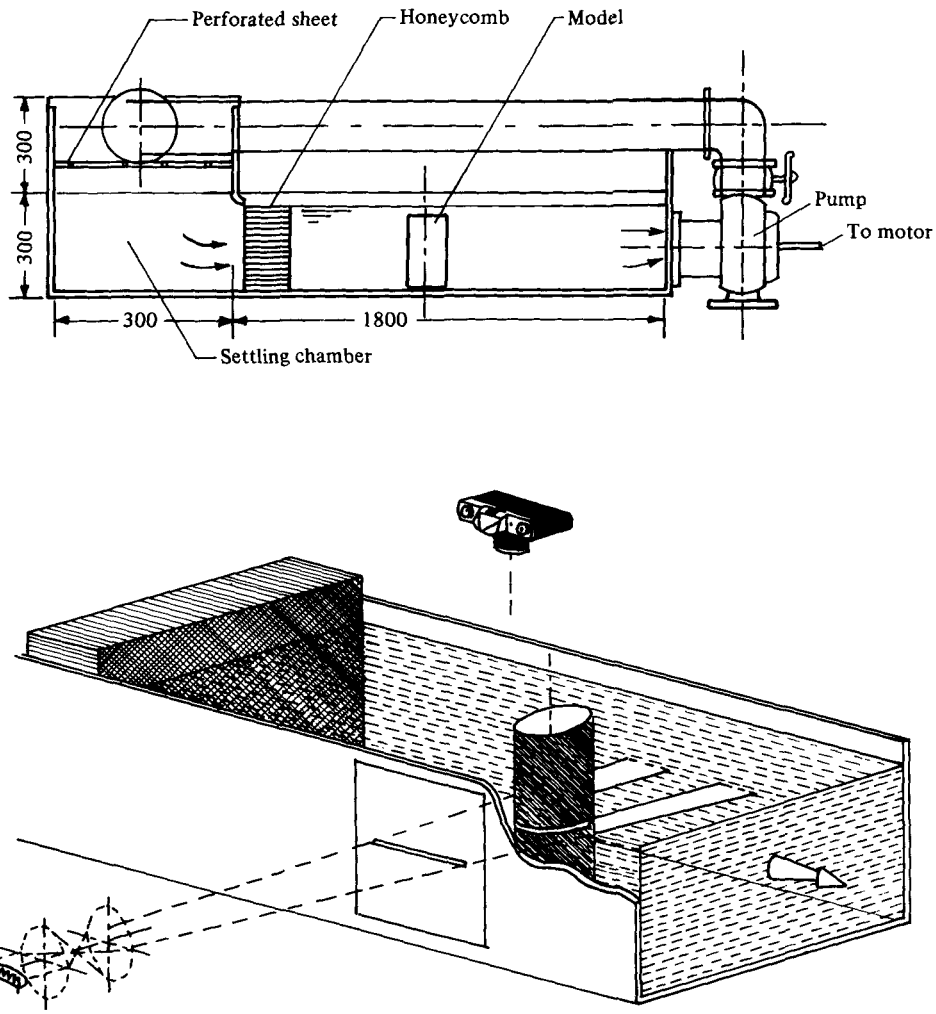

FIGURE 4. Schematic representation of the optical arrangement and the test section.

particles with special buoyancy properties. For visualization beneath the surface, it is necessary to generate a flat sheet of light. This is accomplished by a system of lenses and a narrow slot on the wall of the channel (see figure 4). The photographic equipment is mounted above the channel as shown in figure 4. A 16 mm movie camera with speeds up to 80 frames per second (AROFLEX-S) and a 35 mm motor-drive still camera (NIKON-F2) with a MICRO-NIKKOR 55 mm lens were used to record the flow.

Flow visualization was achieved at first with hydrogen bubbles and Pliolite particles. These methods did not prove convenient for our open-channel facility: the first due to the necessity of special designs for locating wires next to moving walls, the second due to problems with proper lighting and visualization across the free surface of the medium.

In this phase of our work we were interested mostly in low-Reynolds-number flows and such flows were produced with water–glycerol mixtures. However, it was dis-

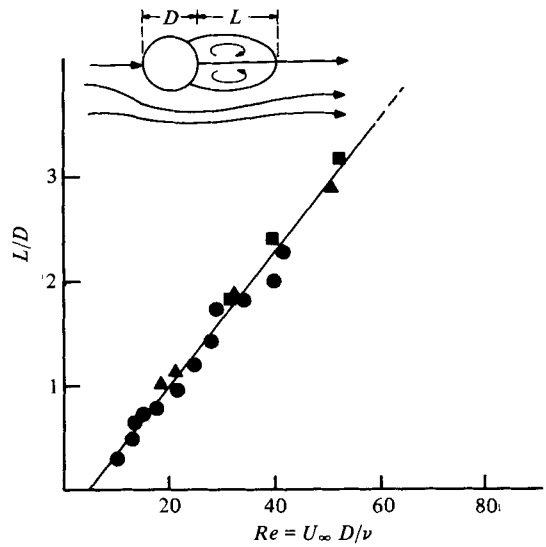

FIGURE 6. The length of the wake as a function of the Reynolds number. ●, Taneda (1971); ▲, Fage (1934); ■, present; ——, theory.

covered that such mixtures quickly become milky if they are subjected to violent turbulent motion. Indeed the flow goes through a region of strong forced mixing in the pump and the valve that follows and this makes it very hard to visualize it beneath the free surface. Most of the experiments with glycerin–water mixtures were performed with surface pellets and surface visualization.

The flow over a circular cylinder was chosen for two basic reasons. On one hand the flow about a fixed circular cylinder is well documented and comparison with earlier analytical and numerical results is possible. On the other hand rotation of the cylinder about its axis of symmetry leaves the potential flow undisturbed, at least if the secondary effects of wake distortion are ignored. The motion of the skin is then the only disturbance of the flow. Any other configuration would require a system of belts on the skin of the body in order to achieve boundary motion with no disturbance of the outer flow.

The flow was visualized on the surface with dyes injected upstream of the cylinder. Black buoyant pellets were also used to visualize particle paths. Still photographs of the flow were taken with exposure times of $\frac{1}{2}$, $\frac{1}{4}$ and $\frac{1}{8}$ s. In these photographs established dye paths appeared, clearly marking the wake region as shown in figure 5 (plate 1). Moreover, the pellets appear as shaded segments on the film. These segments are proportional to the average velocity of the particles, provided the streamline curvature effects are not very strong. All the experiments were performed with a 1:1% water–glycerol mixture, which achieves a viscosity of 7 cP.

Experiments were performed with a fixed cylinder, in order to compare with earlier experimental data. It should be noted that, for the low Reynolds numbers tested, the wake is made up of two finite closed recirculating bubbles as shown in the visualization of figure 5. In figure 6 we compare the length of the wake as measured in our flow-visualization pictures with theoretical results compiled by Pruppacher, LeClair &

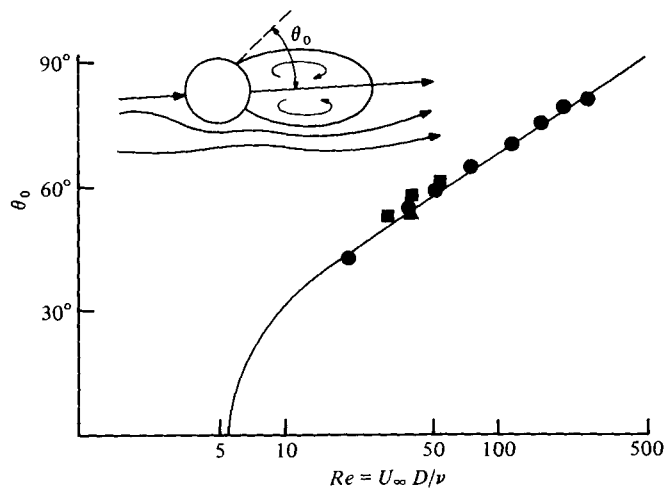

FIGURE 7. The angle to separation as a function of the Reynolds number. ●, Homann (1937); ▲, Taneda (1971); ■, present; ——, theory.

Hamielec (1970) and the experimental data of Homann (1937), Fage (1934) and Taneda (1971). Figure 7 shows the location of separation for different Reynolds numbers. The present results are in good agreement with earlier analytical and experimental results, since their scatter appears to be in line with the cluster of other experimental points.

Separation over moving walls

The flow over a rotating cylinder was studied for Reynolds numbers ranging from 35 to 600 and velocity ratios $u_w/U_\infty = 0{\cdot}4$ to $1{\cdot}4$, where u_w is the velocity of the cylinder skin and U_∞ is the velocity of the undisturbed flow. This corresponds to velocity ratios of approximately $u_w/U_e = 0{\cdot}2$ to $0{\cdot}7$, where U_e is the outer flow velocity in the neighbourhood of separation, that is at $\theta \simeq 90°$. The wake of the rotating cylinder for $u_w/U_\infty = 0{\cdot}8$ with separation over the downstream-moving wall, is shown in figure 8 (plate 2). Figure 9 (plate 2) shows the other side where the flow is opposed by the motion of the skin. The immediate neighbourhood of the points of separation is visualized better by shorter film exposures and larger magnification.

Figures 10(*b*) and 11(*b*) (plates 3 and 4) show the streamline pattern in the neighbourhood of separation as obtained from the flow visualization of figures 10(*a*) and 11(*a*). Figures 8 and 10 indicate that the streamline pattern of separation over a downstream-moving wall is that of a saddlepoint; that is a stagnation point exists away from the wall. Separation may be defined as the location where the velocity vanishes. Separation is displaced with respect to its fixed-wall location in the direction of the motion of the skin. This displacement is shown in figure 12 plotted against the velocity ratio u_w/U_∞. The agreement with the results of other methods is quite satisfactory. However the aim of the present work is to elucidate the qualitative features of separation and no effort was made to generate more data.

The case of an upstream-moving wall has always been very controversial and

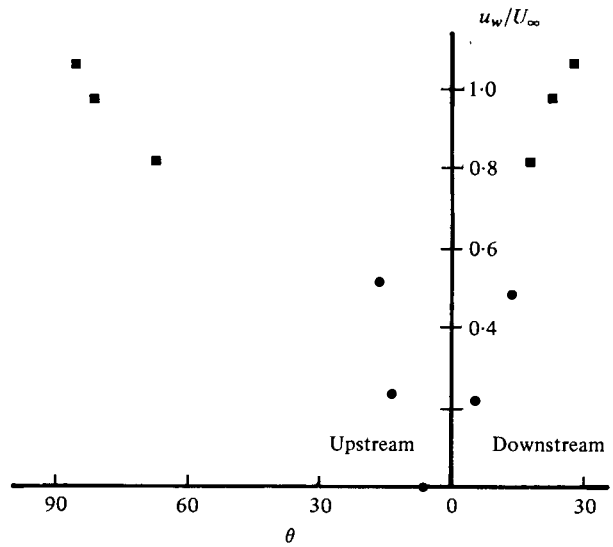

FIGURE 12. Displacement of separation with the wall velocity ratio, u_w/U_∞. ●, Ludwig (1964); ■, present.

perhaps the problem has not yet been resolved. Moore (1958), Rott (1956) and Sears (1956) argue that the point of separation over an upstream-moving wall should again be a stagnation point and such that, in its neighbourhood, the same criterion is met [equation (2)]. The streamline configurations suggested by these authors, however, are not in agreement, as Sears & Telionis (1975) emphasize. Earlier experimental evidence on the topic is inconclusive. Ludwig (1964) discovered that the thickness of the boundary layer on the side of an upstream-moving wall is very large and a sublayer is present which appears to be coming from the wake. As a result, it was not possible to check the singular profile assumed by Moore, Rott and Sears. It is clear that the boundary-layer equations do not permit a solution that meets the MRS criterion for the case of an upstream-moving wall (Fansler & Danberg 1976). However, this does not exclude the possibility that the MRS condition is actually met in real life and therefore that the Navier–Stokes equations could capture it. In fact Tsahalis' (1976) numerical calculations indicate that, for the case of an upstream-moving wall, it appears that MRS conditions are approached with the same rate with which the Goldstein singularity is approached.

The present experimental evidence indicates indeed that a saddlepoint configuration exists on the side of the cylinder where the wall is moving upstream. This is shown clearly in figure 11. Therefore, the fluid in one of the four areas defined by the critical streamlines is moving with the wall in a direction opposite to the outer flow. This is in agreement with the observation of Ludwig (1964) who describes it as 'a sublayer which appears to be coming from the wake'. In fact it is felt that Ludwig's discovery should by no means be considered an anomaly. Such a layer would be necessary if a saddlepoint pattern were to exist in this neighbourhood, as Sears & Telionis (1975) point out.

An overall flow pattern emerges now which together with the distorted separation bubbles is shown in figure 13. The streamline pattern shown in this figure was always

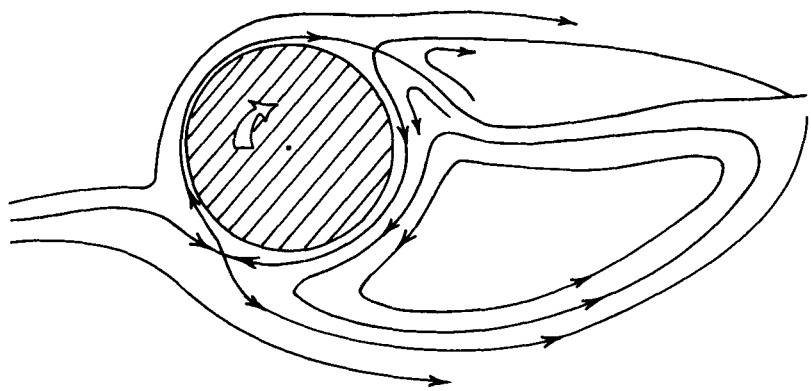

FIGURE 13. Approximate streamline pattern for $u_w/U_\infty = 0{\cdot}8$, $Re = 50$, obtained from flow visualizations.

observed during our experiments. It was not convenient to capture it in one photograph but piecing together the information received from smaller frame pictures we arrived at the sketch of this figure. The geometry of this figure may not be very accurate but on the other hand this is more than just a schematic of the flow field. The error involved in sketching these streamlines, that is their sideways displacement, was estimated to be less than 10 % of the diameter of the cylinder. The streamline pattern shown in figure 13 has only two critical points. It appears that the upper point of separation has merged with the rear stagnation point and the lower point of separation has merged with the front stagnation point in agreement with earlier conjectures of Telionis (1970, 1977).

3. The experimental lay-out

In order to eliminate the effects of free surfaces on the pressure and velocity variations, it is necessary to work with closed test sections. In fact, for larger speeds and especially for pressure gradients dynamically disturbed, the pressure variations on configurations of our interest generate unacceptable surface waves and distort the flow field. Two closed-circuit water tunnel facilities were designed and constructed.

This study is based essentially on flow visualization methods. It represents an effort to investigate qualitatively and quantitatively the immediate neighbourhood of the point of separation. Flow visualization is particularly attractive for flows that involve abrupt changes of the velocity vector in magnitude or direction, such as separating flows. Laser-doppler velocimetry was employed as a calibration tool. Some measurements were also obtained by the LDV system, especially in oscillating boundary layers. Both methods are described in the following subsections.

The VPI water tunnel

The VPI water tunnel was expected to meet the following basic specifications. (*a*) Test sections needed to be appropriate for studying laminar or turbulent boundary layers as well as the potential flow about simple models. Reynolds numbers based on the

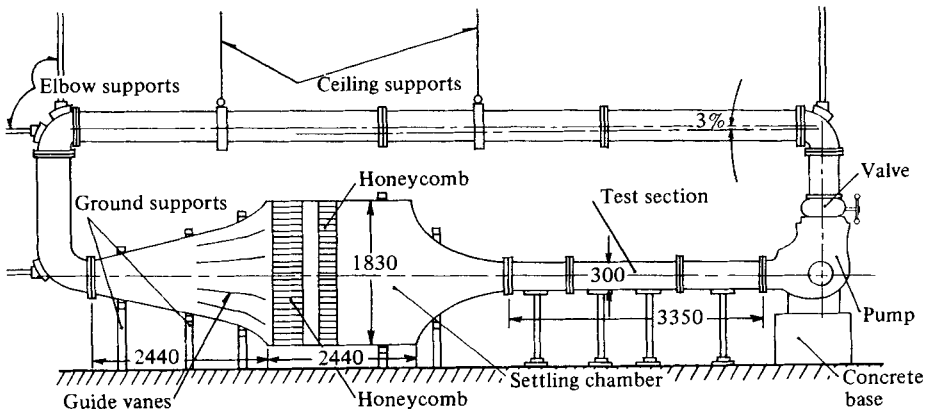

FIGURE 14. The VPI low-speed water tunnel.

length of the test section should therefore range from 10^4 to 10^6 or more. (*b*) The lowest possible volume was required so that expensive fluids like glycerin–water mixtures, Dow–Corning Fluid, etc., could be used to fill the facility. (*c*) The tunnel materials needed to resist corrosive fluids as for example NaCl solutions, necessary for hydrogen-bubble visualization, potassium permanganate and dilute acidic solutions for dye visualization, etc. It should be noted that no permanent dyes can be used, since the working medium is usually expensive and cannot be discarded after a set of dye visualization experiments. (*d*) The operation was required to be free of vibrations. It is imperative that vibrations from the pump and the driving motor or any device used to generate unsteady hydrodynamic effects should not be transferred to the test section. (*e*) The total cost must be within the order of \$15 000. These standards appeared difficult to meet due to unexpected rises of material costs.

To meet these specifications the tunnel shown in figure 14 was designed. Long and carefully calculated diffusers were avoided in order to meet the requirements of low cost and small total volume of working medium. Synthetic materials resisting the corrosive chemicals were chosen, namely Plexiglas for the test sections and the settling chamber and PVC pipes for the remaining sections of the tunnel.

A circular to rectangular converging section leads to the short diffuser and the settling chamber (see figure 14). Guide vanes situated in the diffuser cut the size of large eddies and suppress separation on the walls of the diffuser. At the upstream end of the settling chamber two aluminium honeycombs are situated as shown in figure 14. These honeycombs are made by Hexcel–Bel Air and have hexagonal openings of approximately 3 cm^2 cross-sectional area and a diameter to length ratio equal to 12. The diffuser, the settling chamber, the converging section and the test sections are all constructed out of Plexiglas pieces of dimensions $1{\cdot}8 \times 101{\cdot}6 \times 203{\cdot}2$ cm ($\frac{3}{4}$ in. × 4 ft × 8 ft). A great effort was made to avoid large elastic deflexions of the side walls of the settling chamber. This was accomplished by prestressed external steel reinforcements and transverse aluminium bolts.

The converging section leads into a 25 × 30 cm (10 × 12 in.) rectangular test section. The test section is made of interchangeable units of 2·7 m (9 ft) total length. In this way large Reynolds numbers with not so large velocities can be achieved. A flexible shoot

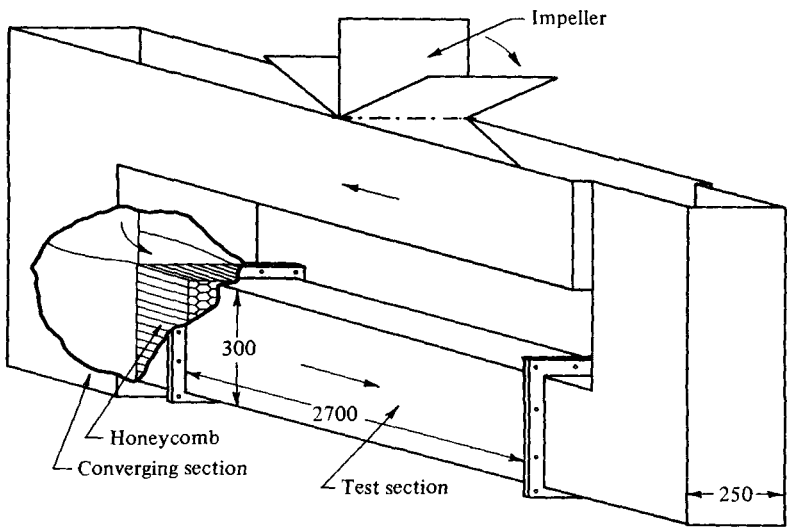

FIGURE 15. The VPI free-surface water tunnel (dimensions in mm).

leads the flow into a low-head pump. The pump is made by Bell and Gossett (model: VSCS–PF, S & D $12 \times 14 \times 12\frac{1}{2}$) and has the following basic characteristics: 12 in. discharge diameter, 8 ft head, and 2000 g.p.m. flowrate. Chrome coating of the pump housing and the impeller appeared very expensive and time consuming. Instead it was decided to have these components cold-galvanized by Livingstone Coating Co. of North Carolina. Two motors are available to drive the pump. The first is a 'Marathon Electric' 1170 r.p.m., 230 V, 15 h.p. motor which can drive the system at full speed (3 m s^{-1}). To control the speed of the tunnel a DURCO BL-311 cast iron valve with a Teflon lining and a stainless-steel butterfly is connected to the discharge of the pump. For the low range of velocities a 2 h.p., 220 V variable speed motor (U.S. Electrical Motors with a U.S. Varidrive) is also available. This motor can drive the pump with a range of 292–675 r.p.m.

Elbows, transitions from rectangular to circular sections and piping that connects the pump to the settling chamber were manufactured out of PVC (polyvinyl chloride).

A smaller facility was also constructed as shown in figure 15. This is a closed-circuit tunnel with a free surface above the test section. The test section is totally submerged but the driving of the flow can be accomplished through a low-speed impeller at the free surface of the facility. This tunnel offers the advantages of very small volume of contained fluid, convenient exchange of the working mediums and, as a result, access to the model and the sensing devices. The same test sections for our larger facility are received and, therefore, preliminary tests can be performed with the small tunnel. Both facilities were calibrated with the flow visualization methods described in the sections that follow as well as by laser anemometry. More information on structural details, three-dimensional effects, turbulence levels, etc., can be found in Telionis & Koromilas (1978).

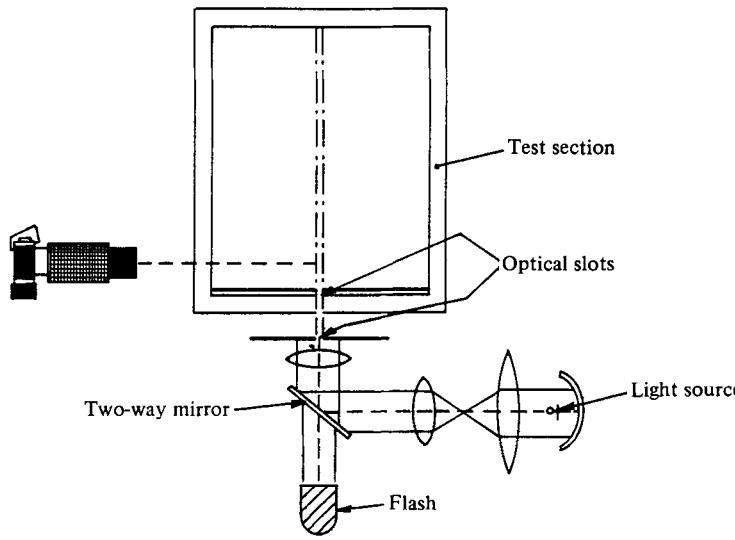

FIGURE 16. The optical system for flow visualization.

Optical methods

To visualize the flow, we use Pliolite† and Amberlite‡ particles that are dispersed in the fluid. The density ρ of these substances is respectively 1·02 and 1·05 g cm^{-3}. These particles are separated by sieve-screening, according to their sizes, into particles of the order of 0·1 to 0·2 mm. Pliolite particles are bright white and should be preferred because of their higher reflectivity. However, mixtures of glycerin and water are more dense than pure water and Pliolite particles dispersed in such mixtures experience buoyancy forces that push them toward the top of the facility. Amberlite particles were found to be more useful for experiments with glycerol–water mixtures. The particles to be used in a certain experiment are mixed in vertical columns and allowed to settle. The neutrally buoyant particles are withdrawn from the mixture, leaving behind the ones that either float to the top or sink to the bottom of the column.

The flow is visualized in planes parallel to the walls of the test section. All of the models tested are two-dimensional and the test section is scanned to check the two-dimensionality of the flow. A thin sheet of light is generated by a system of lenses as shown in figure 16 or by a parabolic reflector. The nearly parallel light so generated is passed through two successive slots of 5 mm width and then it is led into the test section. In front of the reflecting mirror and along the light path, a flash bulb is also situated, which may flash through the same slots into the test section.

Still pictures are taken with a 35 mm 'Olympus' camera and a 90 mm, f2·8 'Vivitar Macro' lens. Time exposures of $\frac{1}{2}$ up to $\frac{1}{20}$ s are used. The images of particles expose the film over the time exposure interval by segments proportional to the average local velocity. This method has some limitations. The larger the speed of a particle, the shorter time its image exposes the film at a certain point and therefore the contrast is reduced. This drawback could be eliminated only if a very powerful source of light is

† Pliolite is the commercial name of polyvinyltoluene butadiene, made by Goodyear Chemicals.

‡ Amberlite is the commercial name of a white ion-exchange resin, IRA-93, made by Rohm and Haas Company.

used. It was also discovered that the method is not appropriate for recording flow fields with both large and small velocities. The proper camera speed is determined by the order of magnitude of the velocities that are expected in the region of interest. If a camera speed is chosen to reveal a small-velocity field, then the faster-moving particles expose almost the entire width of the film and it is impossible to measure the lengths of individual path segments. Moreover, the direction of the instantaneous velocity cannot be calculated with accuracy, since for unsteady flows the particle paths do not coincide with the instantaneous streamlines of the flow. Finally a minor error may be introduced due to the finite speed of the camera shutter. Details of the problem and a method for correcting the data obtained by this method are described in Telionis & Koromilas (1978).

Criticism of this method may arise from the fact that, for large accelerations of the flow and for long time exposures ($\frac{1}{2}$, $\frac{1}{4}$ s), the average velocity may be very far from the instantaneous velocity. For all the experiments performed, this effect was carefully considered and the error involved was estimated. A typical length for changes due to unsteady diffusion is the quantity $L_d = (\nu t)^{\frac{1}{2}}$ whereas the path travelled by a particle in the same period of time is $L_p = Ut$. The ratio of the two lengths, $L_d/L_p = (\nu/U^2 t)^{\frac{1}{2}}$, is a dimensionless number indicative of the relative order of changes due to unsteady diffusion and convection. The smaller this number, the more accurate the representation of the unsteady flow by the present method. In our experiments this number was kept below the value of 0·05.

With the opening of the camera shutter, a flash may be triggered to direct an intense beam of light through the same optical path (see figure 16). In this way the beginnings of particle path segments are marked on the film with brighter spots. This technique is particularly helpful if reversing flows are to be examined.

The models

Separation of the boundary layer is usually induced by adverse pressure gradients. However, its location is almost unaffected by changes of the outer flow conditions if the body configuration induces regions of strong adverse pressure gradients. In the extreme case of a sharp corner, as for example the flow over a backward-facing step, separation is located almost always at the corner. A lot more interesting for practical applications are the cases of mild adverse pressure gradients, as for example the flow over airfoils. In these cases it is possible that minor changes of the outer flow, like a small increase of the angle of attack, may result in large excursions of the point of separation. This implies large changes in the pressure distribution and therefore large changes of integral quantities like drag, lift, etc.

To investigate the phenomenon of unsteady separation, we decided first to design an ideal situation where, for steady flows, two distinct locations of separation, at points say I and II, could be achieved. The flow would then be forced to readjust from conditions I to conditions II impulsively, or in a transient manner or continuously, back and forth between I and II, in an oscillatory fashion. To this end, a circular section with dimensions given in figure 17 is attached at the bottom of the test section. This model is made out of Plexiglas to permit lighting of the flow on its surface. It will be referred to in the sequel as model A. A 7 mm-deep hole was drilled and later filled with epoxy, to provide a length scale. This is shown in almost all of the flow visualization pictures that

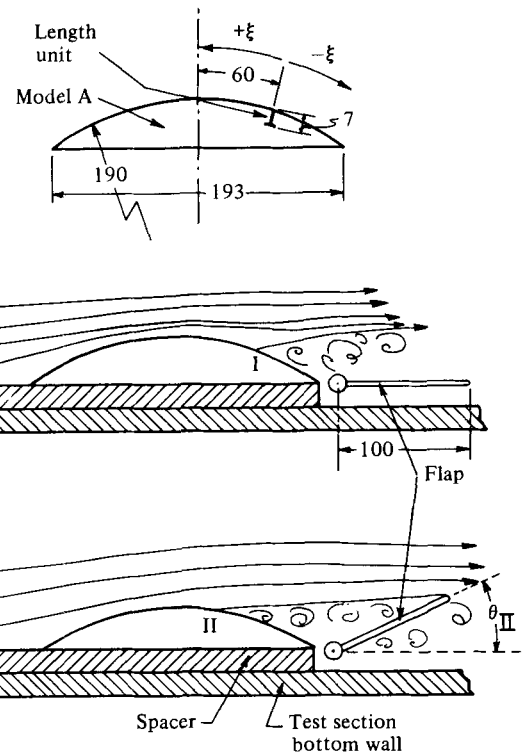

FIGURE 17. The model A and the extreme flap positions.
All the dimensions are in mm.

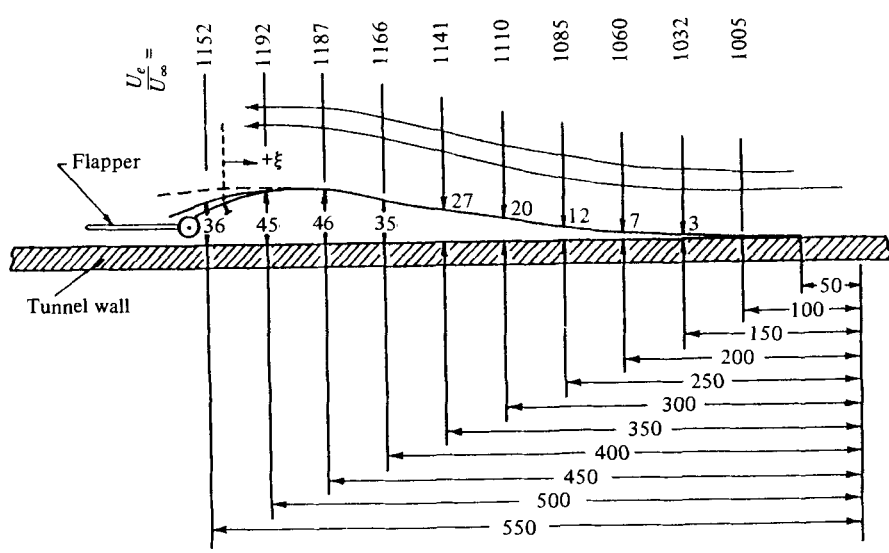

FIGURE 18. The model B. Dimensions in mm.

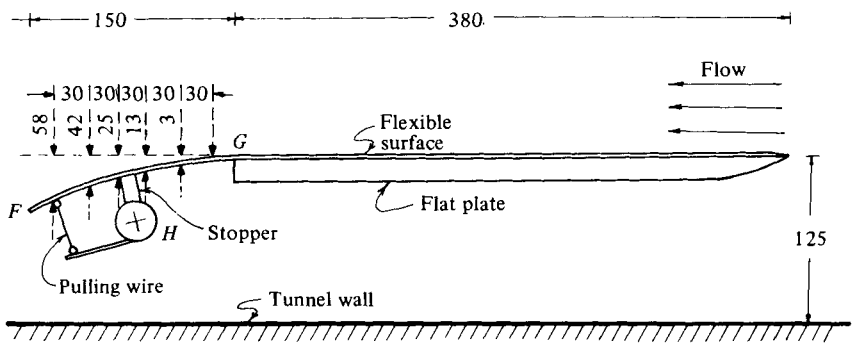

FIGURE 19. The model C. Dimensions in mm.

follow. It was later used to calculate the lengths of particle path segments as well as to define the axial co-ordinates on the skin of the body. The boundary layer is allowed to grow on the bottom wall of the test section. It is then led over a small accelerating region, at the forward portion and towards separation at the lee side of our model. Separation is controlled by a flap as shown in figure 17. Two positions of the flap are found that, for steady flow, correspond to two distinct locations of separation, positions I and II shown schematically in figure 17.

Experiments were also performed with a second model which essentially represents smoothing of the contours and hence pressure gradients of the circular arc just described. The dimensions of this model, referred to in the sequel as model B, are given in figure 18. The afterbody of this model is adjustable, permitting minor changes in the values of the adverse pressure gradient. Unfortunately it is very difficult to measure pressure variations in water at speeds of the order of 0·1 to 0·5 m s^{-1}. Instead we measured the velocity variation at the edge of the boundary layer. This is recorded on top of figure 18 in terms of the ratio U_e/U_∞, where U_e is the outer-edge velocity and U_∞ is the undisturbed mean-flow velocity at the entrance to the test section.

The experiments described in §§ 4 and 5 correspond to flows over fixed surfaces, while unsteadiness is introduced via outer-flow pressure disturbances. In the last subsection of § 4 we describe our experiments with moving surfaces. In the first category we simulate changes of the airfoil environment due to gusts or outer flow disturbances. The second category corresponds to changes of the angle of attack of an oscillating blade.

Changes of the shape and orientation of the model surface are accomplished with flexible surfaces. A flat plate is attached in the middle of the test section in order to provide some distance for the boundary layer to grow. The surface of the plate is covered by a thin flexible surface which extends further downstream as shown in figure 19. The flexible part of the model can be deflected downward, thus generating a zone of adverse pressure gradients and separation.

The thin plate that extends downstream is essentially a cantilever beam. The bending-moment distribution and therefore the curvature of the plate decrease from point F towards point G at which the pulling wires are attached. It is desirable to simulate the flow over a Howarth body, i.e. a body over which the outer-flow distribution decreases linearly:

$$U_e = U_\infty - kx.$$

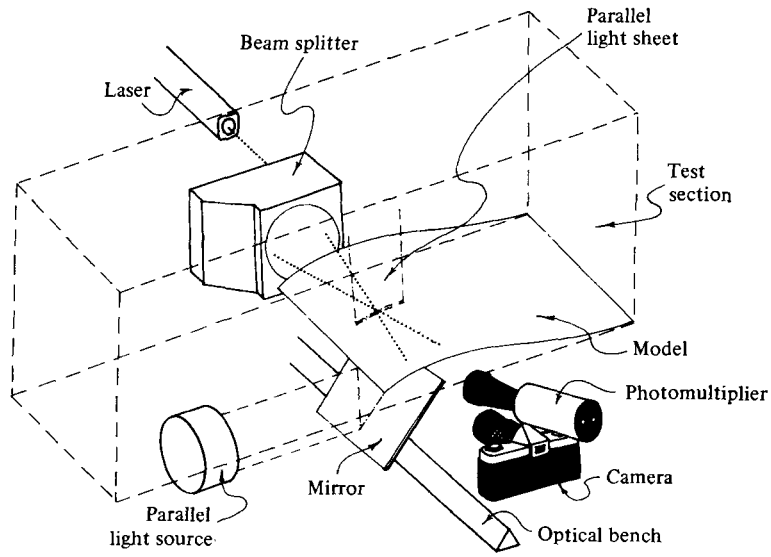

FIGURE 20. The experimental arrangement for simultaneous flow visualization and LDA measurements (reference beam mode).

This implies that U_e starts decreasing right at the leading edge of the plate, and its curvature increases with x. This would be a very difficult flow to obtain experimentally. However, in order to approach somewhat this distribution and achieve larger excursions of separation, the flexible plate is supported at one more point between F and G, the point H. In this way large curvatures in the neighbourhood of point G are avoided.

Laser-doppler velocimetry

For the Laser–velocimetry measurements a DISA LDV one-channel system (55L series) was used. The transparent walls of the test section permit the use of the forward-scattering mode. The arrangement of the equipment is shown in figure 20. A laser tube directs a laser beam into a DISA beam splitter (55L01). A system of brag cells is attached on the casing of the beam splitter to provide for frequency shifting. The two beams are then led into the test section and allowed to cross at the point of interest (measuring volume). A photomultiplier (55L10) is focused at the measuring volume as shown in the figure. The signal is directed to a preamplifier, an oscilloscope and a DISA signal processor (55L20).

Only the component of the velocity parallel to the boundary of the model at a certain ξ station is measured. The laser-beam arrangement in space is shown in figure 21. The plane of the two beams, p, is given an angle of inclination with respect to the horizontal, β, equal to the slope of the model boundary at the point of interest. The two beams are shown in the figure crossing the vertical wall of the test section at the points A and B, crossing each other at M where the measuring volume is formed and penetrating the model boundary at the points A' and B' respectively. The bisector of AA' and BB' in the plane p is also given a slight inclination, α, with respect to the horizontal, say the generator of the model boundary at the point of interest. The fringes are thin planes parallel to the plane r, inclined by an angle β with respect to the vertical plane q. The

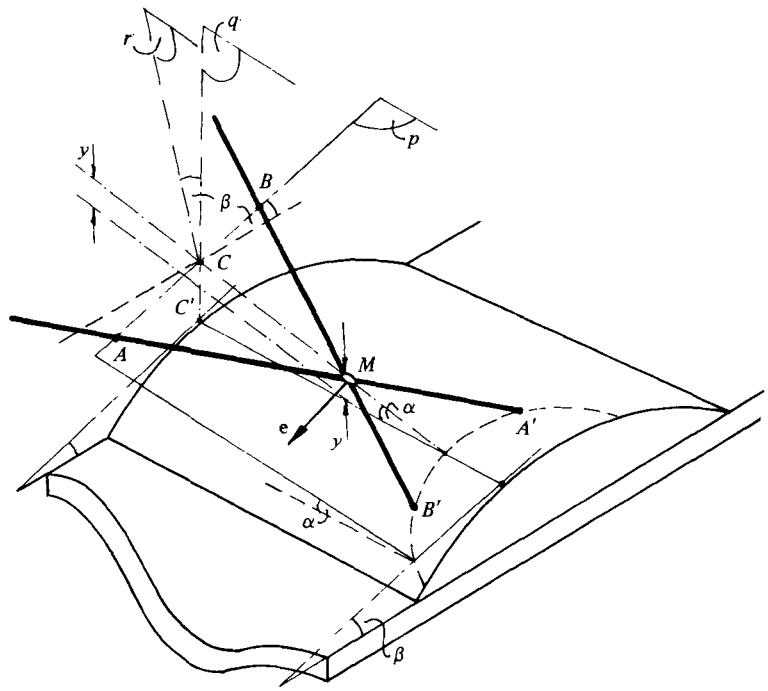

FIGURE 21. Angles involved in laser velocimetry.

normal to the plane of the fringes is denoted by the vector **e** in figure 21 and it is parallel to the model boundary at this point. This arrangement permits the measurement of the velocity component in the direction of **e**, regardless of the value of the angle α.

To measure vertical distances and record the position of measurement the following procedure is followed. The optical bench is lowered until the points A' and B' coincide with the point M, that is until the two beams intersect exactly at the skin of the model. A scale is then located vertically on a side wall, with its zero at the point where one of the beams intersects the tunnel walls. From then on, vertical displacements of the optical bench are read on this scale. The method is as accurate as possible for the determination of the point $y = 0$.

Since the scattering mode permits maximum scattered light collection, the aperture of the photomultiplier collecting lens can be set to higher values (smaller diameters). This decreases the optical noise and permits better focusing on the photomultiplier's pinhole. This in turn results in better signal-to-noise ratios and lower drop-out percentages. It was found that frequency shifting further improves the signal-to-noise ratio. The addition of plain 'Coffeemate' slightly improves the quality of the Doppler signal. No special seeding problems were encountered.

During the initial tests of the system it was found that mechanical vibrations travelling through the concrete floor are transmitted to the optical bench. This was discovered by projecting the fringes on a vertical wall. With the pump motor on, the fringes can be clearly seen to jitter. As a result, a spurious noise is received which appears on the recorder similar to a turbulent velocity measurement. These vibrations were eliminated by supporting the optical bench on a 10 cm thick Styrofoam plate.

4. Transient and impulsive changes of the outer flow

In this section we describe results of experiments performed with the models A, B and C. Unsteadiness is introduced here via impulsive or transient changes of the flap, via mean flow accelerations and decelerations and by impulsively changing the shape of model C.

Impulsive changes, $Re = 10^5$, model A

In the first phase of our experiments, using model A and water as a medium, we examined the case of impulsive changes of the flow. To this end the flap was connected to a lever and a strong spring. With the release of the lever a microswitch was activated and the flap quickly moved from position I to position II. A simple system of electronics was used to activate the camera and the flash. This was first accomplished using a delay-circuit to control the opening and the closing of the camera's shutter. The time delay, Δt, between the initiation of the phenomenon and the opening of the shutter was controlled and the experiment was repeated with different Δt in order to observe the sequence of unsteady velocity fields. This set of experiments was conducted in the small water tunnel (figure 15) which has a rather high level of free-stream turbulence.

The method described has a clear disadvantage. A sequence of photographs thus generated does not correspond to different instances of the same transient phenomenon, spaced apart by equal time intervals. It represents, instead, the flow field of repetitions of the same transient phenomenon, viewed at different instances after its initiation. The repeatability of the flow is therefore an important factor and in fact some of the sequences of photographs indicate discrepancies.

One set of experiments was performed with model A, $Re \cong 10^5$ and a sharp change of the flap inclination from $\theta_{\mathrm{I}} = 0$ to $\theta_{\mathrm{II}} = 40°$. In figure 22 we show four visualizations of the flow at times $t = 0{\cdot}2$, $0{\cdot}4$, $0{\cdot}6$, and $0{\cdot}8$ s after the initiation of the impulsive change, taken with a camera speed of $\frac{1}{8}$ s. The sequence in figure 22 (plates 5 and 6) indicates that the location of separation moves slowly upstream. The initial station of separation is marked in these plates by the symbol S_{I} and the instantaneous station of separation, defined by the wake formation, is marked by an arrow. However, upstream of the point of separation, there exists a relatively thin region of reversed flow, in qualitative agreement with the descriptions of Sears & Telionis (1975), Carr *et al.* (1977) and others (see review article of Telionis 1977). The reversed direction of the flow is apparent from the bright dots that mark the particle location at the beginning of the film exposure.

In figure 23 (plate 7) we show dye visualizations of the same phenomenon. Dye is emitted here approximately 10 mm downstream of the location of steady separation and it is seen to creep upstream, underneath the laminar boundary layer.

Although at this Reynolds number the flow should be laminar, some turbulence, due to the rough design of the small water tunnel and the lack of screens, can be seen in the flow visualization to persist. This set of experiments therefore is not very 'clear', because, although the flow responds in a laminar fashion, it contains random disturances convected from upstream. However, the main characteristics of unsteady separation are still present, despite the high Reynolds numbers and the presence of turbulent 'remnants' in the flow.

A very interesting feature of the flow is apparent from both particle and dye visualization. The separated region grows at the beginning in a controlled fashion but after a certain time it appears that it attains momentum and its thickness increases abruptly. The phenomenon is reminiscent of the bursting of the leading-edge separation bubble. This is clearly shown in the last frame of figure 22. The momentum thus generated quickly takes the form of a well-organized vortex. The weak turbulent field of the wake is probably still present but the dominant motion appears clearly to be the vortical motion and the exchange of mass with the outer stream which is accomplished further downstream. This trend appears to persist in all the experiments performed and it is documented in many sequences of still frames some of which will be included in later sections.

Impulsive changes, $Re = 10^3$, model A

Experiments performed with smaller Reynolds numbers indicate a characteristically different behaviour. Such experiments were performed in the smaller facility (figure 15) with a mixture of glycerin and water in a ratio 60 % by volume. The use of glycerin mixtures permits us to reduce the Reynolds numbers without simultaneous reduction of the velocities. It is therefore easier to observe the flow and capture a velocity field with reasonable film exposure time. Examination of low Reynolds number flows using water as a testing medium would require very small velocities and unrealistically small Δt's. However, the use of glycerin has some disadvantages as well. The dimensionless number $L_d/L_p = (\nu/U^2t)^{\frac{1}{2}}$, which describes the ratio of distances of diffusion propagation to particle displacement, grows. As a result, the error involved when using the present method becomes larger. In the experiments performed with glycerin–water mixtures, L_d/L_p ranged between 0·05 and 0·12.

Transient flows are investigated again for low Reynolds numbers. A more sophisticated triggering system is now being used. It involves a KIM-1 microprocessor which is programmed to receive the signal of the initiation of the impulse and then activate the flash and trigger the camera at specified intervals of time. A schematic representation of the electronics is shown in figure 24. The system is capable of obtaining samples of periodic flows allowing the phase angle to increase with each period as described in a later section. Details on the programming of the microprocessor are described in Telionis & Koromilas (1978). In this way it is possible to receive snapshots of the same phenomenon at different times and thus capture the evolution of a single unsteady flow field. In figure 25 (plates 8 and 9) we show a sequence of velocity fields taken with a camera speed of $\frac{1}{2}$ s and a Reynolds number equal to 1000. The first frame represents the steady flow for $\theta = 0$. The second frame is shot with a delay $\Delta t_0 = 0{\cdot}5$ s after an impulsive change of the flap angle from $\theta = 0$ to $\theta = 40°$. The following frames were obtained at intervals of $\Delta t = 1$ s. The speed of exposure was kept rather low in order to reveal the properties of slowly moving flow at the bottom of the laminar boundary layer and in the separated region. Immediately after the initiation of the impulsive change, the flow indicates a violent departure from the steady-state configuration. Very soon, two distinct recirculating regions appear and a saddlepoint configuration is formed at approximately the station where steady separation occurred. These flow patterns could be interpreted as 'reversed flow upstream of separation', if separation is defined as the saddle point that is shown in this figure.

The velocity fields shown in these frames are indeed fully contained in the viscous

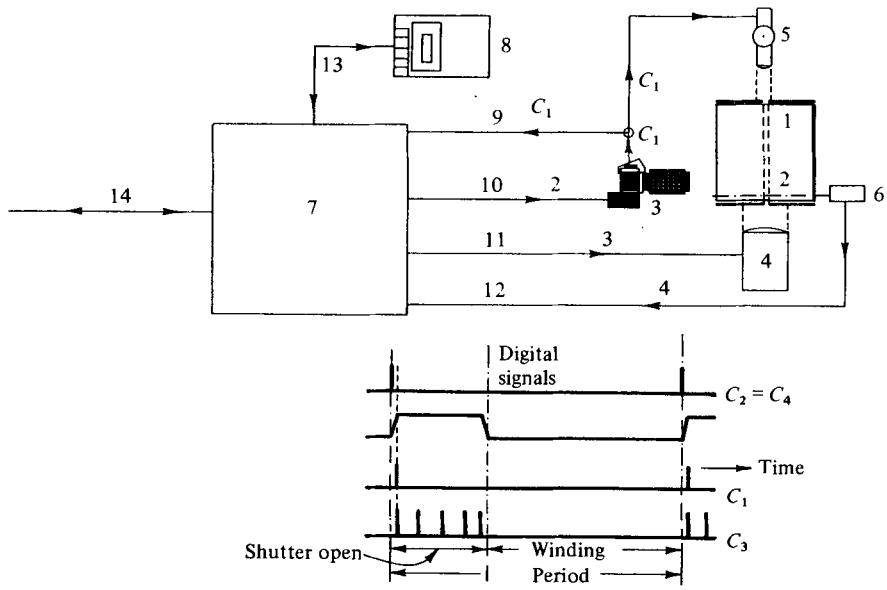

FIGURE 24. The triggering system interfaced with a microprocessor. 1, Test section with transparent walls (cross section); 2, plane of light (observation plane); 3, Olympus OM-1 Motor drive camera (3 frames per second) with Vivitar 90 mm f 2·8 macro lens (1:1 magnification ratio); 4, fast recycling xenon strobe (up to 20 flashes per second) combined with continuous output 1000 W quartz lamp in the same housing and focused at infinity by a lens; 5, Vivitar 283 strobe (up to 3 flashes per second) focused at infinity by a lens; 6, oscillator (variable speed motor oscillating a shaft); 7, KIM-1 (MOS) microprocessor (6502 array) with two 6530 arrays (ROMS), 1152 bytes of 'READ' 'WRITE' memory, two programmable interval timers, six l.e.d. display, keyboard, audio cassette interface, TTY interface; 8, audio cassette recorder interfaced with the microprocessor; 9, camera's shutter open feedback through cameras X synch and slow strobe's (5) control line; 10, motor drive control line; 11, fast strobe's (4) control line; 12, r.p.m. 2 phase feedback through a l.e.d./photosensor; 13, audio cassette interface; 14, TTY interface with IBM computer (optional).

region of the flow. This becomes clear from velocity profiles derived from the visualization of figure 25 and shown in figure 26. However the first bubble seems to retain its identity even after the flow has arrived at its steady-state condition. It is therefore possible that such recirculating bubbles are part of the wake which, for low Reynolds numbers, is usually made up of a few discrete vortices.

It should be emphasized that, with larger viscosities, viscous diffusion is increased and the response of viscous phenomena, including separation, is faster. The sequence of photographs shown in figure 25 could be interpreted therefore as follows. Separation immediately moves upstream. The temporal rearrangement of the vortices then represents the familiar unsteadiness contained in the wake. This would be the interpretation that the numerical analyst would probably offer (Mehta & Lavan 1975; Mehta 1977). A similar phenomenon has been encountered in unsteady internal flows and an attempt to distinguish between unsteady 'detachment' and unsteady 'separation' is made by Telionis (1975). In the last few years it has become evident that the concept of 'unsteady separation' is meaningful only for large Reynolds numbers, a regime most interesting for aerodynamic applications (Telionis 1977; Williams 1977; Shen 1978).

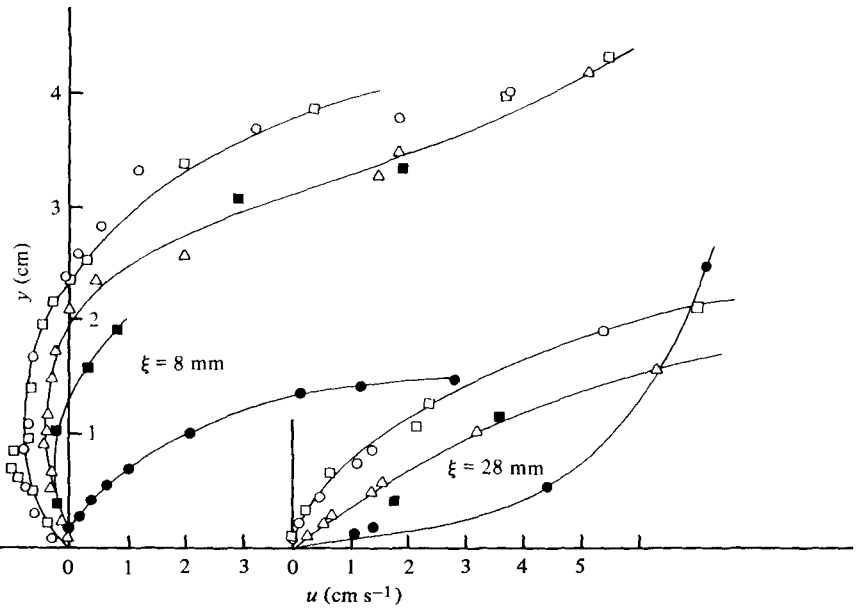

FIGURE 26. Velocity profiles at stations $\xi = 8$, 28 mm (see figure 17) derived from the flow visualization of figure 25. ●, $t = 0$; △, $t = 0{\cdot}5$; □, $t = 1{\cdot}5$; ○, $t = 2{\cdot}5$; ■, $t = 7{\cdot}5$.

In figure 27 (plates 10 and 11) we show a sequence of velocity fields again for $Re \cong 1000$ but with a final flap inclination $\theta_{II} = 30°$. The general characteristics of the flow are similar. In fact it is now easier to accept that the leading recirculating bubble is part of the attached boundary layer. It appears quite possible, and in fact our experimental data seem to support the idea, that, with growing Reynolds numbers, the flow patterns shown in figures 25 and 27 are conserved but their dimension perpendicular to the wall shrinks together with the laminar boundary layer. If this is true, it would imply that the patterns of figure 25 and 27 represent the recirculating flows in front of an upstream-moving separation as described by Sears & Telionis (1975) and Despard & Miller (1971).

Impulsive changes, $Re = 10^4$, model B

We repeated the experiments in the closed water tunnel (figure 14) with water ($Re \cong 10^4$ using the triggering system shown in figure 24 and model B, which provides milder pressure gradients. The sequence of frames shown in figure 28 (plates 12, 13 and 14) was made with an initial delay $\Delta t_0 = 1$ s and subsequent time intervals $\Delta t = 1$ s. These plates represent average flow fields of a single phenomenon which is developing in time. In the blow-up of one of these frames (figure 29, plate 15) the very thin layer of reversed flow predicted theoretically is clearly shown. Figure 30 shows a sequence of velocity profiles at $\xi = 0$. These profiles correspond to the initial steps of the motion during which the flow is well ordered and the wake appears in the form of a recirculating bubble. The sequence of plates of figure 28 indicates, once again, that a finite period of time after the impulsive change, here at $t = 4$ s, a spectacular explosion occurs in the wake and the particles of the wake, including the ones that reside next to the wall, are jettisoned into the flow. Subsequently this erratic motion subsides and the configuration approaches the steady flow that corresponds to the final flap angle.

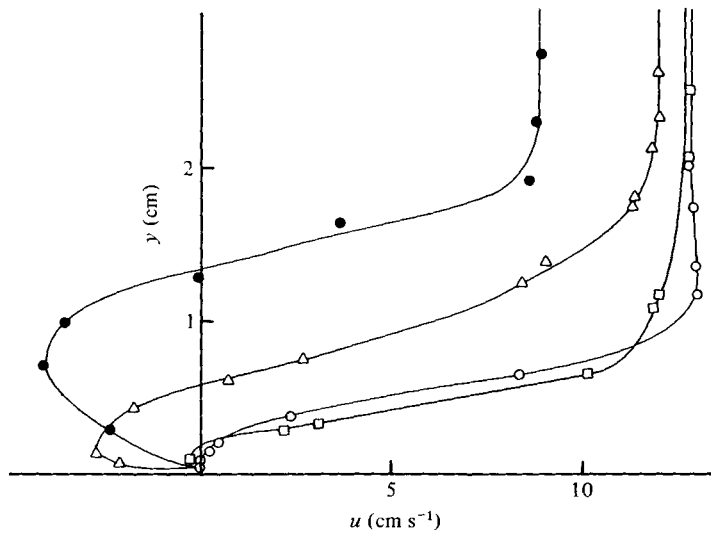

FIGURE 30. Velocity profiles at station $\xi = 15$ derived from the flow visualization of figure 28. ○, $t = 0$–$0{\cdot}25$ s; □, $t = 1$–$1{\cdot}25$ s; △, $t = 2$–2.25 s; ●, $t = 3$–$3{\cdot}25$ s.

Mean-flow accelerations

In another set of experiments we studied the response of laminar separation to accelerating and decelerating outer flows, for $Re \approx 10^4$. In these experiments the disturbing flap was completely removed and unsteadiness was introduced only via the change of the magnitude of the outer flow. It should be noted here that potential flow is unaffected by such changes and the streamline configuration of inviscid flow should remain undisturbed. The flow is governed by Laplace's equation

$$\nabla^2\phi = 0$$

with ϕ the potential function. Time is introduced via the boundary conditions, in this case the free-stream velocity. However, in inviscid flow the pressure is given by Bernoulli's equation

$$\frac{\partial\phi}{\partial t} + \frac{V^2}{2} + \int\frac{dp}{\rho} = f(t),$$

where V, p and $f(t)$ are the velocity, pressure and an arbitrary function of time respectively. Clearly time variations of ϕ generate pressure disturbances which in turn influence to location of separation.

In figure 31 (plate 16) we show a sequence of velocity fields for a flow accelerating from $U_\infty = 12\,\mathrm{cm\,s^{-1}}$ to $U_\infty = 25\,\mathrm{cm\,s^{-1}}$. The visualization at $t = 0$ corresponds to the undisturbed flow. The flow at an initial interval $\Delta t_0 = 0{\cdot}5$ s and subsequent intervals $\Delta t = 1$ s after the initiation of the acceleration is shown until $t = 3{\cdot}5$ s. An inspection of the outer flow is enough to convince that during the acceleration process the outer flow essentially 'washes away' the separated region. Indeed separation is displaced downstream and eventually moves out of the frame of observation. Subsequently and after the outer flow has achieved the new steady velocity of $25\,\mathrm{cm\,s^{-1}}$, the point of separation moves slowly again into the picture and at $t = 6$ s it arrives at almost its

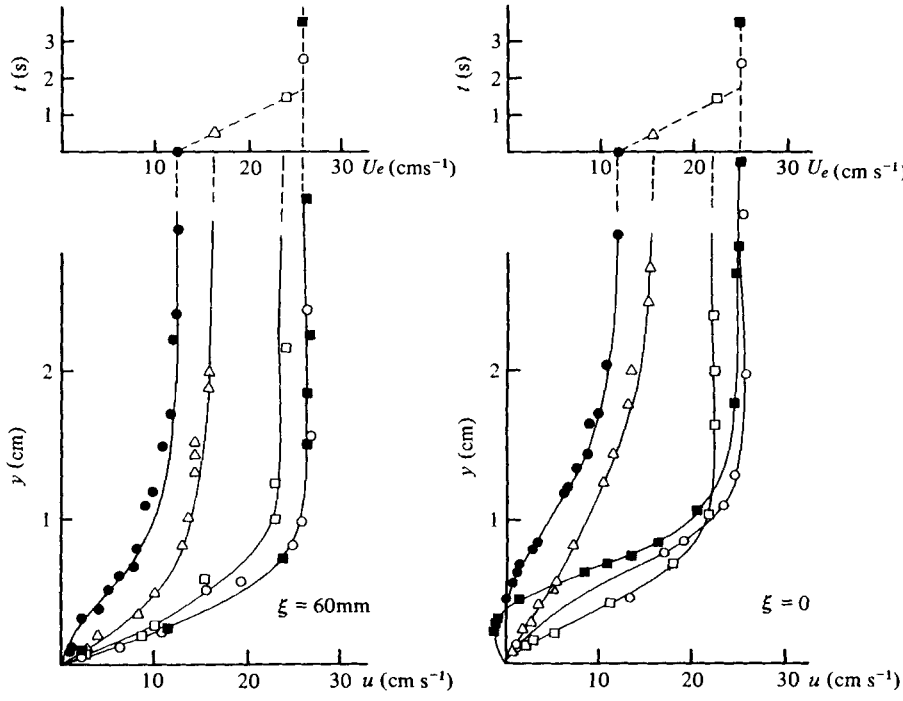

FIGURE 32. Velocity profiles at stations $\xi = 0$, 60 mm (see figure 17) derived from the flow visualization of figure 31. ●, $t = 0$; △, $t = 0{\cdot}5$ s; □, $t = 1{\cdot}5$ s; ○, $t = 2{\cdot}5$ s; ■, $t = 3{\cdot}5$ s.

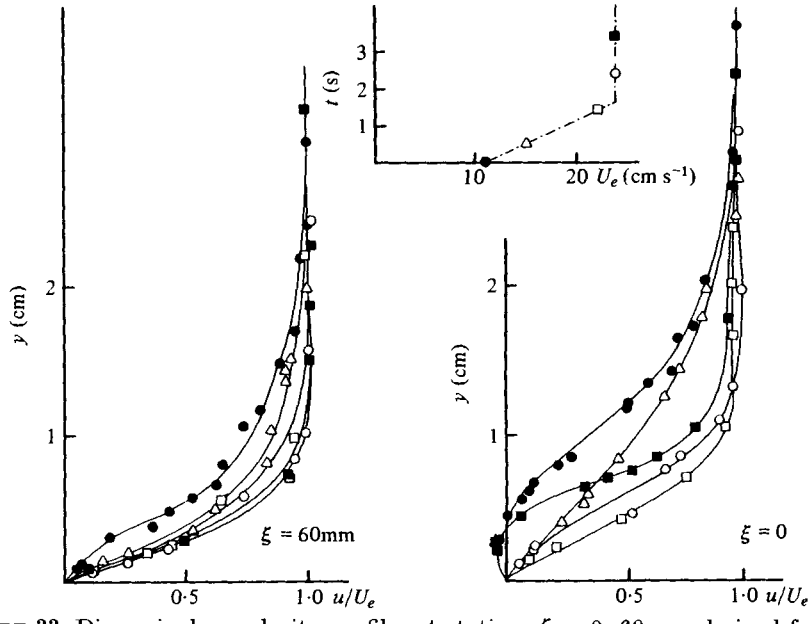

FIGURE 33. Dimensionless velocity profiles at stations $\xi = 0$, 60 mm derived from the data of figure 32 where the symbols are explained.

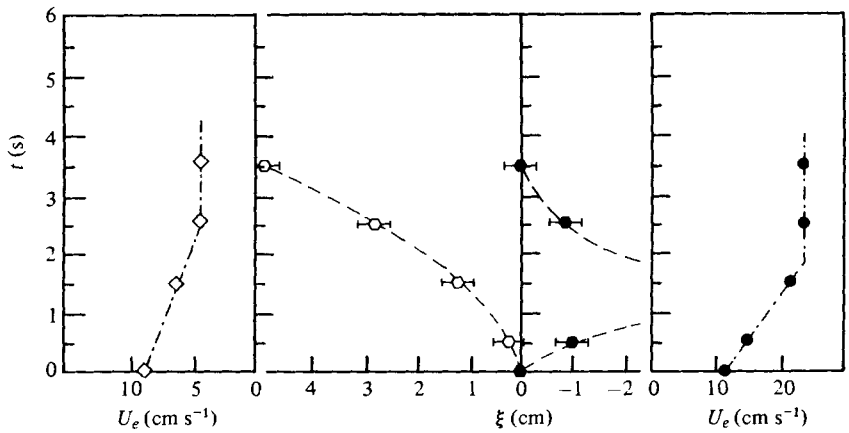

FIGURE 35. The excursions of the point of separation for accelerating (open symbols) and decelerating (closed symbols) flows.

initial position. This was expected since, for $Re \approx 1000$ or above, the location of separation in steady flow is insensitive to the magnitude of the outer flow velocity.

Velocity profiles obtained from these visualizations are shown in figure 32. These profiles correspond to the stations $\xi = 0$ and $\xi = 60$, that is, the point above the scale marker and 60 mm upstream. The flow at $\xi = 0$ is probably a very small distance downstream of the point of steady separation. The velocity profile at this point clearly shows a vanishing of the skin friction, or perhaps a small region of slow reversed flow. After the acceleration of the outer flow begins, the wall shear becomes positive and increases sharply. The inflection point of the profile disappears and only, after the outer flow achieves its final value, do we observe again a sharp decrease of the velocity, the appearance of a point of inflexion and a vanishing value of the velocity at the same distance from the wall as for $t < 0$. Normalized velocity profiles are shown in figure 33.

A sequence of instantaneous velocity fields for decelerating flows is shown in figure 34 (plate 17). In this case the point of separation is displaced sharply upstream, while the separated region thickens abruptly. As time grows the flow pattern returns again to its original configuration.

A plot of the excursions of separation for accelerating and decelerating flows is shown in figure 35. In the same figure we show the variations of the outer flow for comparison. It appears that the time scale of the response of separation is of the same order of magnitude with the scale of changes of the outer flow. Experiments repeated with much smaller accelerations resulted in weaker displacements of the point of separation, until no effect at all on the location of separation could be observed.

Separation over model C, $Re = 10^4$

Model C is the flexible model described in the previous section. Its dimensions are given in figure 19. This model was essentially designed with a Howarth flow in mind. Such flows are very hard to reproduce, as explained earlier, and the present model is only a rough approximation to a Howarth body. The leading part of the model is a flat plate

with a sharp leading edge. The development of the laminar boundary layer can be calculated easily by numerical analysis.

Unsteadiness in this case is introduced only by the change of the shape of the model. No other external disturbances of the flow are involved. The deformation of the model, from a flat surface to the shape shown in figure 19, simulates, for example, a sharp change of the angle of attack of an airfoil.

The experiments are performed as follows. The lever that drives the flexible surface is turned up so that the surface *GHF* (see figure 19) is lifted to become an extension of the flat plate. Laminar attached flow and a Blasius steady boundary layer are allowed to develop on the flat plate. At a certain instant, t_0, the lever is given a sharp displacement and the flexible surface deforms to its new position as shown in figure 19. The microprocessor is programmed to trigger the camera at t_0 and at $t_0 + n\Delta t$ so that again a sequence of frames are taken.

At first the flow is fully attached as shown in the first frame of figure 36 (plates 18 and 19). This clearly demonstrates the inertia characteristics of the phenomenon demonstrated first for laminar flow by the numerical calculations of Telionis, Tsahalis & Werle (1973). Shortly after the impulsive change, a portion of the skin of the body is covered with a very thin layer of reversed flow. However, the outer flow remains attached. The activities of flow reversing and vortex forming are confined at first to a very thin layer at the bottom of the boundary layer. The streamlines of the flow follow very closely the contour of the body. Therefore very small pressure disturbances should be expected at this time level.

Soon after, at $t = 0{\cdot}8$ s, two distinct vortices are formed. One, which extends upstream, seems to be the oldest. The second, further downstream, is historically younger but has already developed into a thicker vortex, clearly showing the potential to develop into a disturbance of larger scale. The subsequent development is a little confusing and we were unable to follow an orderly upstream propagation of the phenomena under consideration: flow reversal and separation. We attribute this fact to the geometrical properties of the model we have constructed, which does not have a monotonically increasing curvature.

5. Periodic disturbances of the outer flow

In the present paper we report only on some preliminary findings in the area of oscillatory flows. Disturbances are again generated via flaps of different sizes at the downstream end of the models as shown in figure 17 and 18. The flap is driven by a variable-speed motor via pushing rods in the shape of a parallelogram. In this way, no external unbalanced forces are transmitted and the test section is free of vibrations. The mechanism that drives the parallelogram is a classical crank–connecting-rod system with a relatively long rod, so that harmonic oscillations can be approximated. The range of frequencies thus accomplished is 0·5–5 Hz. Experience derived from the present experiments and earlier analytical and experimental investigations indicates that separation responds to unsteady disturbances with a characteristic inertia-like behaviour. It was thus expected that the domain of interest would rather be in the lower part of the range of frequencies.

The triggering device shown in figure 24 is used to signal all the events. A photosensor receives a signal at a specified phase of the rotating disk which drives the flap

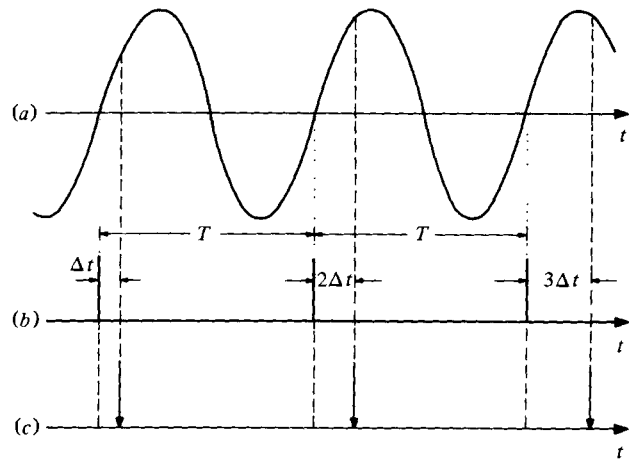

FIGURE 37. Schematic representation of signals. (*a*) Amplitudes of oscillating flap. (*b*) Signal received from the l.e.d. and led into the microprocessor. (*c*) Signal sent to sensing equipment (camera, LDV).

(see point 6 in figure 24). This message is fed into the microprocessor, which in turn sends a signal to the camera (line 10) with a delay time Δt. After one cycle is completed, the microprocessor delays the signal by $2\Delta t$, etc. Thus, during the nth cycle, the signal arrives at the camera delayed by $n\Delta t$. If the quantity $n\Delta t$ exceeds the period of oscillation, then the process is repeated starting from zero delay. A schematic representation of the events is shown in figure 37. In this way measurements are taken at different phases of the periodic motion.

Figure 38 (plates 20 and 21) shows a sequence of averaged velocity fields of a flow oscillating with a period $T = 0{\cdot}6$ s and an average Reynolds number $Re = 5 \times 10^5$. Measurements were obtained for $\Delta t = 0{\cdot}1$ s. The film exposure time was $\frac{1}{15}$ s. At $t = 0$ the flap angle was $\theta = 0$. The separated region appears to gain momentum and its thickness increases sharply. A relatively violent vortex is in fact propagating upstream until it engulfs the whole wake. However the location of separation is barely affected by the oscillatory motion and remains approximately at the position $\xi = 15$ mm, that is two unit lengths upstream of $\xi = 0$. The steady flow corresponding to the same configuration is shown in figure 39 (plate 22).

Velocity profiles measured at the point of separation as detected from the flow visualizations are shown in figure 40. In this figure it is shown that the wall shear fluctuates between zero and a negative value. It is therefore concluded that, for the case considered, the criterion proposed by Despard & Miller (1971) is met. Despard & Miller define separation as the location at which, as one traces the wall in the downstream direction, one encounters for the first time a skin friction that remains negative throughout the cycle of oscillation.

Despard & Miller measured velocity profiles and detected separation by inspecting the outer flow. In the present experiments the outer flow is visualized in considerable detail. However, our interpretation can be rightly criticized. It is very possible here that we see what we wanted to see. A different interpretation can be based on alternative definitions of separation.

For steady high-Reynolds-number flows, it is true that the separated region consists

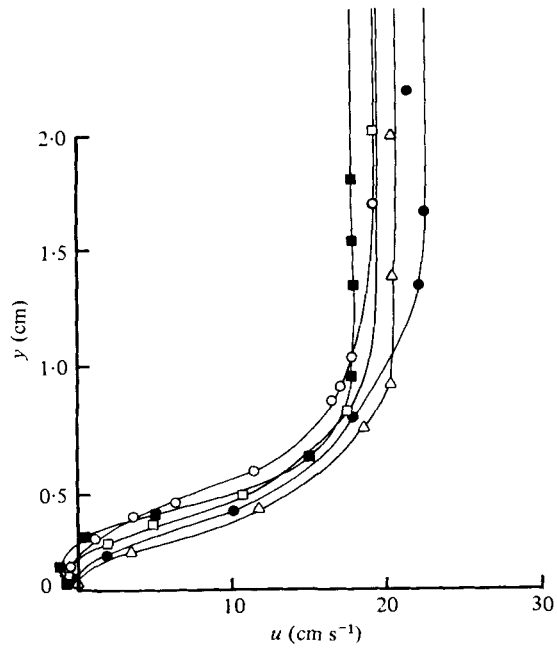

FIGURE 40. Velocity profiles of the flow of figure 38 at $\xi = 15$ mm. ●, $t = \frac{1}{6}T$; △, $t = \frac{2}{6}T$, □, $t = \frac{3}{6}T$; ○, $t = \frac{4}{6}T$; ■, $t = \frac{5}{6}T$.

of fully turbulent, very slow flow, contained within well-defined boundaries. This is not the case for unsteady flows. It is well known by now that unsteady flows over airfoils are characterized by the formation of small or large vortices, which are convected with the mainstream, leave the body and activate the wake to generate a periodic motion, very similar to von Kármán's vortex street. Such vortices, however, are totally removed from the boundary layer and their size is usually one order of magnitude larger than the thickness of the boundary layer.

In order to study the structure of the boundary layer in the neighbourhood of separation the present experiments were conducted with thick boundary layers. However, the familiar unsteady phenomena of the vortex generation are still present, even though such activities are totally contained in the boundary layer. In other words, the typical dimensions of large-scale vortices are of the same order of magnitude as the boundary-layer thickness.

One more comment is pertinent here. The flow visualizations of steady flow (figure 39) with the flap at the position I and the first frame of figure 38 appear to be quite similar. However there is a very significant difference. The region $0 < \xi < 30$ of the separated region in figure 39 contains 'dead' fluid. The velocity there is almost zero. On the other hand the same region in figure 38 contains activated flow which is recirculating. Moreover, the boundary of the separated region in figure 39 is close to a straight line almost parallel to the free stream whereas, in the first frame of figure 38, the 'boundary' that separates the free flow from the recirculating flow is a lot closer to the surface. This could be interpreted as attached non-separated flow as shown schematically in figure 39(*b*). In other words the dotted line of figure 39(*b*) and the first frame of figure 38 indicate that the disturbance of the outer flow may be very small

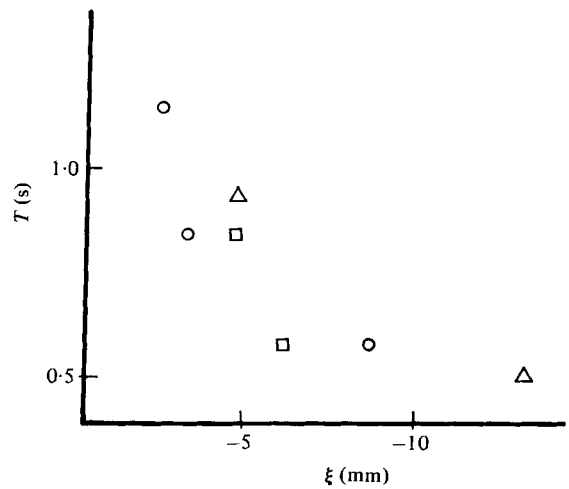

FIGURE 41. The downstream displacement of the point of separation. △, $Re = 5 \times 10^5$; □, $Re = 6 \times 10^5$; ○, $Re = 8 \times 10^5$.

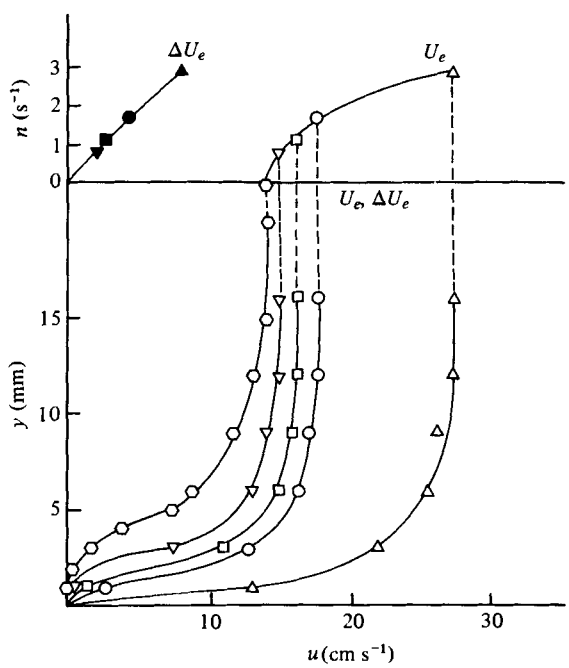

FIGURE 42. Averaged boundary-layer velocity profiles obtained by LDV, at $\xi = 0$. △, $n = 2{\cdot}95$ Hz; ○, $n = 1{\cdot}75$ Hz; □, $n = 1{\cdot}16$ Hz; ▽, $n = 0{\cdot}83$ Hz; ○, $n = 0$ Hz.

and the pressure distribution may not be far from the distribution of a fully-attached flow. It would be very interesting to run the same experiments for higher Reynolds numbers. If the present conjecture is right, then the region below the dashed line should get thinner, since this is part of an attached boundary layer.

In the spirit of these observations it may be appropriate to define separation as the

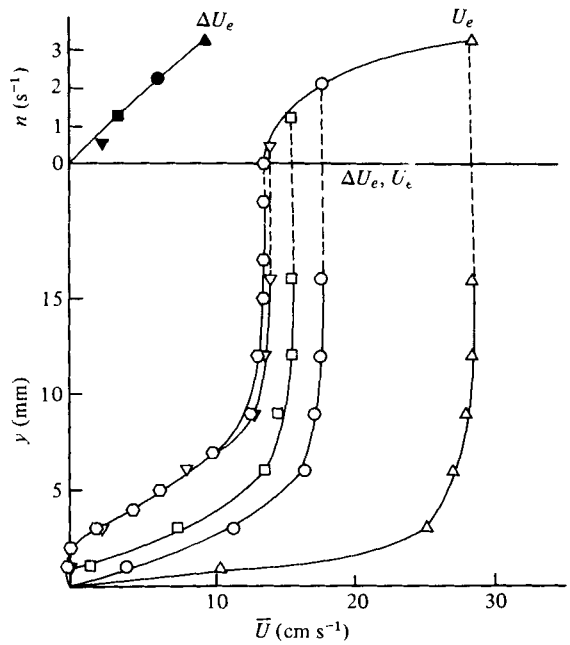

FIGURE 43. Averaged boundary-layer velocity profiles obtained by LDV, at $\xi = -12$ mm. △, $n = 3{\cdot}27$ Hz; ○, $n = 2{\cdot}08$ Hz; □, $n = 1{\cdot}25$ Hz; ▽, $n = 0{\cdot}48$ Hz; ⬡, $n = 0$ Hz.

leading point of the energized vortical flow which appears in figure 38. This vortex grows and moves upstream during the upstroke. Its strength decreases and it is convected downstream during the downstroke. This periodic motion was found from a large number of data to have a phase lag of approximately 60° with respect to the outer flow.

The displacement of separation from its steady-state position that corresponds to $\frac{1}{2}(\theta_{II} - \theta_I)$, is shown in figure 41. These data were collected from a large number of experiments, run with various values of the frequency. This figure indicates that, in all cases examined, the point of separation is displaced further downstream as the frequency increases. In fact for frequencies of the order of $n = 5$ Hz, separation disappears completely from the models examined in this study. Comparison with the experimental data of Despard & Miller was not possible because of the differences in the range of frequencies examined.

Laser velocimetry of such flows appeared inconclusive because of the confusing and random motion of the wake flow. For such flows it will be necessary to measure simultaneously two velocity components.

The LDV system was used here only for measurement of boundary-layer flows upstream of separation. Samples of raw LDV data as recorded by strip chart recorders are included in Telionis & Koromilas (1978). Oscillatory-flow experiments were conducted with a large disturbing flap but with a fixed mean speed of the tunnel. This results in stronger accelerations and decelerations of the flow and further downstream displacement of the point of separation. This is shown on top of figures 42 and 43. In these figures we plot the average of the outer flow velocities $\overline{U}_e$ and the amplitude of

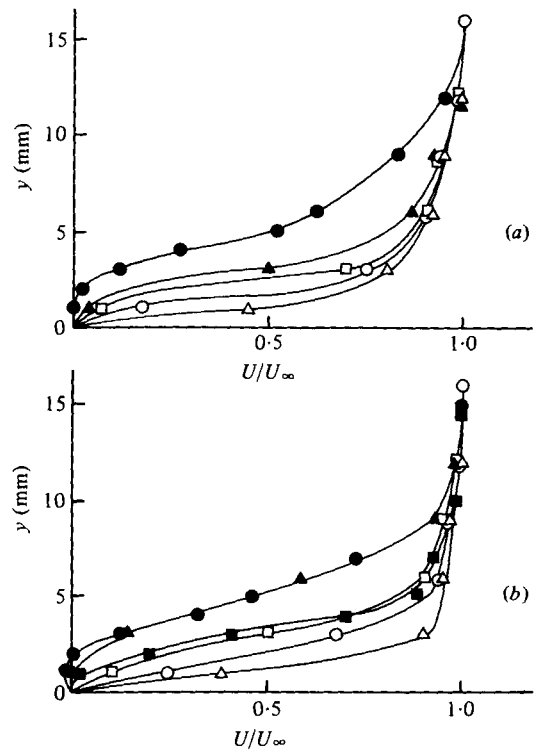

FIGURE 44. Non-dimensional averaged velocity profiles. (*a*) $\xi = 0$: △, $n = 2{\cdot}95$ Hz; ○, $n = 1{\cdot}75$ Hz, □, $n = 1{\cdot}16$ Hz; ▲, $n = 0{\cdot}83$; ●, $n = 0$ Hz. (*b*) $\xi = -12$ mm: △, $n = 3{\cdot}27$ Hz; ○, $n = 2{\cdot}08$ Hz; □, $n = 1{\cdot}25$ Hz; ▲, $n = 0{\cdot}48$ Hz; ●, $n = 0$ Hz; ■, optical (1·5 Hz).

variation ΔU_e for $\xi = 0$ and -12 respectively. It should be emphasized that the flow-rate remains constant and the flap disturbances generate only local mean flow accelerations.

The acceleration effect appears clearly in the averaged profiles shown in figures 42 and 43. In these figures the velocity profiles, for steady flow, indicate that separation may be approximately at $\xi = 0$, whereas at $\xi = -12$ the flow is definitely separated. Optical observations of such flows indicate that indeed the flow separates at approximately $\xi = 0$. Averaged reduced profiles of oscillatory flow are shown in figure 44. In the last figures the averaged values of velocity derived with an optical method are also shown for comparison.

One of the most characteristic features of oscillatory flow is an overshoot of the fluctuating part of the velocity over the amplitude of the outer flow. Velocity amplitudes of oscillation are shown in figure 45 (*a*) and (*b*) for $\xi = 0$ and -12 respectively. As the frequency increases, the maximum of the velocity profile approaches the wall. This is a property well documented both analytically and experimentally. In the present case profiles are obtained very close to separation. Tsahalis & Telionis (1974) have calculated amplitude profiles and indicated that the percentage of overshoot grows as the point of separation is approached. The theoretical curve of Tsahalis & Telionis that corresponds to the furthest downstream points calculated are shown in figure 46 together with some of the experimental points obtained

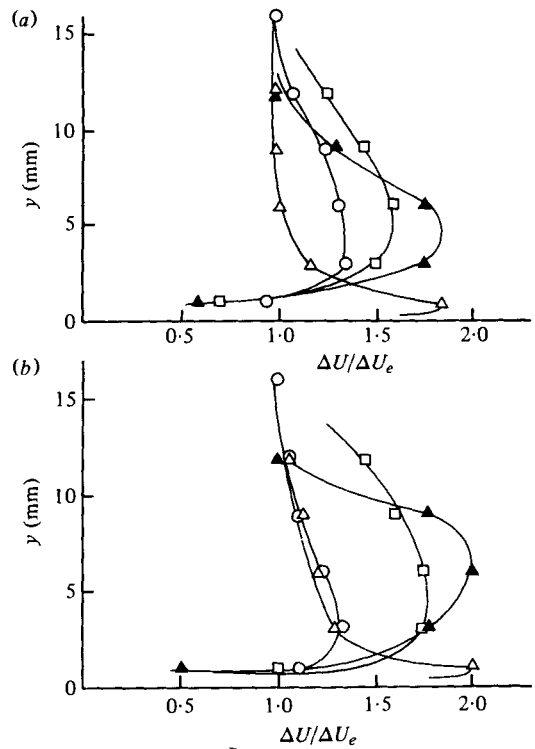

FIGURE 45. Dimensionless amplitude of velocity fluctuation. (*a*) $\xi = 0$: △, $n = 2{\cdot}95$ Hz; ○, $n = 1{\cdot}75$ Hz; □, $n = 1{\cdot}16$ Hz; ▲, $n = 0{\cdot}83$ Hz. (*b*) $\xi = -12$ mm: △, $n = 3{\cdot}27$ Hz; ○, $n = 2{\cdot}08$ Hz; □, $n = 1{\cdot}25$ Hz; ▲, $n = 0{\cdot}48$.

with laser anemometry. Admittedly the two-body configurations are not the same. The contour assumed by Tsahalis & Telionis has a curvature which continuously increases with distance from the leading edge. The present model is preceded by a region of mild, favourable pressure gradient followed by an adverse pressure gradient over a contour with fixed curvature. Moreover, it is difficult to determine the proper scaling factors for the vertical scale as well as the distance from separation. It was finally decided to choose as a length scale for both configurations the distance from the point of zero pressure gradient to the point of separation.

The present investigation clearly indicates that, for the conditions investigated here, separation is displaced downstream if oscillations are imposed on the outer flow. This contradicts the findings of Despard & Miller who found that separation is always displaced upstream. In an attempt to bypass special effects that probably interfere with the experimental lay-out described in this section, we decided to design a completely different experiment. To this end, a sphere 15 cm in diameter was towed in the VPI towing tank. Two different struts were used to support the sphere. The first was heavy and rigid. The second was light and flexible. With the sphere towed at a submerged position the system with the second supporting strut vibrated in the direction of the motion with a frequency of 2·5 Hz. These data correspond to a Reynolds number $Re = U_\infty D/\nu = 10^5$ and a Strouhal number, $St = \omega D/U_\infty = 3{\cdot}2$, based on the sphere diameter. The flow in the boundary layer was visualized by dyes

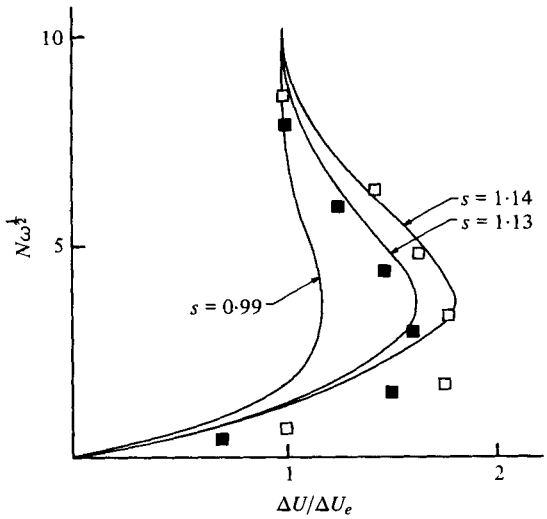

FIGURE 46. Velocity amplitude of oscillations compared to the theoretical predictions of Tsahalis & Telionis (1974). ■, $\omega = 2{\cdot}8$, $\xi = 0$; □, $\omega = 3{\cdot}0$, $\xi = -12$ mm; ——, numerical results, $\omega = 3{\cdot}16$. N is a stretched, dimensionless vertical co-ordinate.

emitted from ports at the point of stagnation and approximately 45° downstream. The azimuthal angle of 90° from the point of stagnation is marked on the sphere with a continuous line.

Figure 47 (*a*) shows the flow about a sphere towed with the heavy strut at a uniform speed. The dyes clearly indicate that the flow is laminar and that separation occurs on a line approximately 80° from the point of stagnation. Figure 47 (*b*) (plate 23) shows the flow about the sphere towed at the same speed, but oscillating as described before. It is clearly seen that separation is displaced downstream to almost 90° from the point of stagnation. The boundary layer has remained laminar and no signs of transition are evident.

6. Conclusions and recommendations

This is the first formal report on an experimental investigation undertaken almost four years ago. It describes briefly the facilities designed and constructed and the experimental methods developed. The main thrust of the effort was directed towards the development of effective and accurate methods of flow visualization, capable of supplying qualitative as well as quantitative information. The target is unsteady and viscous flows and both these characteristics pose particularly irksome difficulties.

The flow visualization method developed, unlike the method of smoke visualization or the hydrogen bubble technique, is non-intrusive. It provides the capability to visualize without preparation any part of the flow and permits the detection of forward or reversed flow. Moreover, the method is applicable to viscous or inviscid as well as to laminar or turbulent flows.

The ultimate goal of this effort was the investigation of unsteady laminar separation. Experiments were performed with rigid and fixed solid surfaces as well as with flexible surfaces that deform dynamically to the desired shapes. Various models were tested

that correspond to varying values of adverse pressure gradients. Time-dependent disturbances of the outer flow pressure distributions were accomplished using downstream flaps, accelerations and decelerations of the mean flow, or deformation of the body contours.

A characteristic inertia in the response of separation was observed in the experiments performed. For impulsive changes of the outer flow the order of magnitude of the time required for the flow to arrive at its new flow pattern is L/U_∞ in qualitative agreement with the work of Tsahalis & Telionis (1974). Separation is usually detected by an abrupt thickening of the wake. An upstream-moving separation is preceded by a thin layer of reversed flow. On occasions this layer was found to be as thin as 5 % of the thickness of the boundary layer. However, even then, methods that detect separation by measuring the wall shear alone, would fail to predict the phenomenon in unsteady flow since the sign of the skin friction is not related to separation.

The present investigation of actual streamline patterns and wake shapes indicates that the problem is more complex than was originally conceived. For mild adverse pressure gradients, which should be the case in flows over thin airfoils, the separated region is so thin that the point of flow reversal may be easily confused with the point of separation. Pressure variations would not be greatly affected by separation and perhaps the argument and the controversy over the proper definition of separation in this case loses its meaning.

One of the most interesting findings of the present study is that, a considerable time after an impulsive change has been performed, the separated region appears somehow to gather momentum and eventually erupts into a violent motion which disturbs the potential flow in a region two or three times larger than the area occupied by the steady-state wake. Subsequently this activity subsides and the flow returns to its steady-state pattern. It is very interesting that the pattern of the flow generated by abruptly changing the shape of the body is very similar to flows generated by a disturbing flap. It should be emphasized that such explosion-type disturbances evolve into large-scale vortical wakes, much thicker than the steady-state wakes that correspond to the initial and the final configuration. This is in fact the case, even for very mild adverse pressure gradients, as for example the flow over lifting airfoils. It is perhaps due to such large-scale disturbances that spectacular overshoots and hysteresis phenomena of integral quantities like lift, pitching moment, etc., are observed.

The study of accelerating or decelerating outer flows indicates a strong influence on separation. A uniform acceleration essentially 'washes away' separation altogether, whereas deceleration pushes separation upstream. After a small interval of time, separation slowly returns to its original position.

Preliminary work with oscillatory flows resulted in conclusions similar to those of Despard & Miller (1971). The averaged location of separation is not affected by the amplitude of oscillation but responds quickly to changes of the frequency of oscillation. The criterion proposed by Despard & Miller is met with reasonable accuracy. However for the range of frequencies and the configuration of the models examined, the point of separation is shifted downstream of its quasi-steady location. Perhaps this is because our outer-flow dependence in axial distance varies with time, a situation that corresponds to a pitching airfoil, whereas Despard & Miller generated disturbances only in the magnitude of the outer flow. Despard & Miller do not provide any information about the shape, size and location of the wake. The present study indicates that the

periodic disturbances of the outer flow induce a well-organized periodic motion in the wake as well. As a result, a vortex is generated downstream of the Despard & Miller point of separation, grows, moves upstream and eventually disappears in a periodic fashion. Once again alternative interpretations may be provided but the most significant characteristics of the flow may be resolved only if reliable pressure data become available. Finally, with regard to oscillatory flows, we should recall that in unsteady airfoil stall studies (McCroskey 1972, 1977), periodicity quite often leads to leading-edge stall, whereby the whole upper surface of the airfoil is covered with a wake. In this case the Despard & Miller model and the present observations would be inapplicable.

Earlier studies of unsteady viscous flows (Wérlé 1973; Ruiter *et al.* 1971; McCroskey 1971; Carr *et al.* 1977; McAlister & Carr 1978; McAlister *et al.* 1978) indicate that large-scale discrete vortices emanate from the leading or the trailing edge of an airfoil, or even sometimes from a relatively smooth surface. These vortices grow quickly and very soon extend deep into the potential flow. In fact their development has been modelled quite accurately in terms of inviscid flow theory. The vortices captured in the present flow-visualization studies are completely embedded in the laminar boundary layer. Yet they exhibit the same characteristic properties found in potential vortices.

This experimental investigation was undertaken in an effort to shed some more light on the theories of Sears (1956), Moore (1958) and Rott (1964), to clarify some of the physical arguments of later contributions (Despard & Miller 1971; Telionis & Werle 1973; Sears & Telionis 1971, 1975; Williams 1977; Carr *et al.* 1977; Mehta & Lavan 1975; Telionis 1970) and provide some evidence for the most recent numerical work (Telionis & Werle 1973; Williams 1977; Telionis 1977; Tsahalis 1976; Tsahalis & Telionis 1974). An objective evaluation of the present findings and their relationship to earlier theories and numerical data is therefore necessary. To begin with, it has been always advocated (Sears 1956; Moore 1958; Rott 1956, 1964) and most recently proved (Williams 1977), that steady separation over a moving wall can be transformed to unsteady separation over a fixed wall. The first problem was investigated here and the saddlepoints, predicted theoretically, were captured for the first time, for both upstream and downstream-moving walls. The evidence of figure 8 indicates that the MRS criterion is met for a downstream wall, since the branches of the saddlepoint configuration are parallel and perpendicular to the wall respectively. This is not true for the case of an upstream-moving wall.

Most of the unsteady flow experiments were performed with an upstream-moving separation. This is easier to realize and more important for engineering applications, since it is intimately connected with unsteady stall. The case of a downstream-moving separation was attempted and some results were included here but they are rather inconclusive. Unfortunately no extensive excursions of separation were possible without a total breakdown of the separation-wake pattern. It was not possible to observe and measure the speed of propagation of separation and therefore it was not possible to make a quantitative comparison with the definition of Sears (1956) and the theory of Sears & Telionis (1971), Williams (1977) and Shen (1978). However, the qualitative patterns appear to be in full agreement with these theories. A very thin layer of reversed flow precedes a more violent wake region, where substantial pressure disturbances should be expected.

One of the objectives of theoretical and experimental studies of unsteady separation

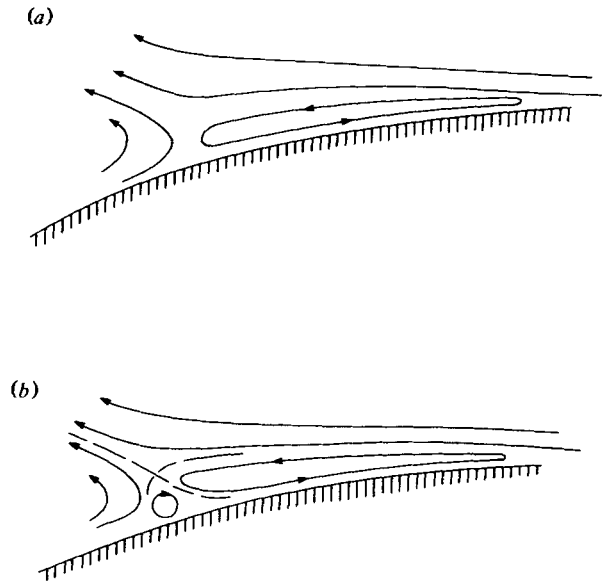

FIGURE 48. Flow patterns for an upstream-moving separation. (*a*) Leading and wake bubbles. (*b*) Leading separation and wake bubbles.

is the development of a criterion that could be used to signal the location of separation. In the numerical integration of the boundary-layer equations, a method is needed to determine the location of unsteady separation and therefore the point where the wake begins and probably large-scale vortices are initiated. It was proposed that the boundary-layer separation singularity could serve this purpose (Sears & Telionis 1971, 1975; Williams 1977). This approach may prove adequate for numerical calculations if the first-order boundary-layer equations are used. However, it is well known that real life and, as expected, the full Navier–Stokes, are free of any singularities in the neighourhood of separation. Except for large-scale visualizations, therefore, there is no available method for determining unsteady separation experimentally.

The evidence contained in this paper indicates that, at least for the case of an upstream-moving separation and for the early stages of the motion, a consistent pattern can be identified. The thin recirculating region upstream of separation, forms a bubble which actually closes at the point of separation. At this point a second bubble, usually much larger, is generated. This is the separation bubble. The pattern is shown schematically in figure 48. Both vortices have a sense of rotation that matches the direction of the outer flow. However, at the point of separation a small recirculating bubble with opposite sense may be formed, as shown in figure 48 (*b*). Such patterns have been found in a very large number of frames obtained by flow visualization, for example: in figure 36, $t = 0{\cdot}8$ s; in figure 28, $t = 2$ s; and in figure 38, $t = 2T/\sigma$. Figure 25, $t = 1{\cdot}5$ s, may be thought of as a pattern similar to figure 48 (*b*) with a stretched scale in the direction perpendicular to the wall, because of the low Reynolds number.

This behaviour of the flow may be used as a signal for the approaching catastrophe. For example the v component of velocity should indicate a very characteristic behaviour there. As long as the boundary layer is attached there is a continuous outflow from the boundary layer. The v component of velocity is therefore positive.

As separation is approached, and in the process of passing from the first vortex to the second vortex, a change in sign of this quantity should be detected. These properties should not be thought of as describing low-Reynolds-number flows for which distinct and organized recirculating bubbles are common. It is well established by now and was documented in this paper that, in unsteady flows, organized vortices may emerge from the region of a steady turbulent wake. In fact, for a truly unsteady flow, the entire field is made up of large and small but well-organized vortices that exchange momentum, thereby fluctuating in size and shape.

A more careful inspection of the pattern of figure 48 (*a*) reveals that matching of the two vortices actually requires the existence of the small recirculating bubble shown in figure 48 (*b*). Moreover, the presence of the three vortices and the outer free flow imply that there exist boundary lines depicted by a dotted line in figure 48 (*b*) and a saddle-point. The velocity at this point is not zero and therefore this is not a stagnation point. Such a pattern is in full agreement with the theory since any saddlepoint streamline configuration maps again to a saddlepoint configuration if the field is viewed by a moving observer, that is if a constant vector is superimposed on the velocity field.

The support of the U.S. Army Research Office under Grant no. DAACO4-75-G-0067 is gratefully acknowledged.

REFERENCES

CARR, L. W., MCALISTER, K. W. & MCCROSKEY, W. J. 1977 Analysis of the development of dynamic stall based on oscillating airfoil experiments. *N.A.S.A. Tech. Note* NASA TN D8382.

DESPARD, R. A. & MILLER, J. A. 1971 *J. Fluid Mech.* **47**, 21.

FAGE, A. 1934 *Proc. Roy. Soc.* A **144**, 381.

FANSLER, K. S. & DANBERG, J. E. 1976 *A.I.A.A. J.* **14**, 1137.

HOMANN, F. 1937 *Forsch. Geb. Ing. Wes.* **7**, 1.

KENISON, R. C. 1977 An experimental study of the effect of oscillatory flow on the separation region in a turbulent boundary layer. In *Unsteady Aerodynamics*, AGARD-CP-227, paper no. 20.

LUDWIG, G. R. 1964 *A.I.A.A. Paper* no. 64–6.

MCALISTER, K. W. & CARR, L. W. 1978 Water tunnel experiments on an oscillating airforl at $Re = 21000$. *N.A.S.A.* NASA TM 78446.

MCALISTER, K. W., CARR, L. W. & MCCROSKEY, W. J. 1978 Dynamic stall experiments on the NACA 0012 airfoil. *N.A.S.A. Tech. Paper* 1100.

MCCROSKEY, W. J. 1971 In *Fluid Dynamics of Unsteady, Three-Dimensional and Separated Flow* (ed. F. J. Marshall), Project SQUID, Purdue University, p. 346.

MCCROSKEY, W. J. 1972 In *Aerodynamics of Rotary Wings, AGARD Conf. Proc.* **3**, 17.

MCCROSKEY, W. J. 1977 *Trans. A.S.M.E.* I, *J. Fluids Engng* **99**, 8.

MEHTA, U. B. 1977 Dynamic stall of an oscillating airfoil. In *Unsteady Aerodynamics*, AGARD-CP-227, paper no. 27.

MEHTA, U. B. & LAVAN, Z. 1975 *J. Fluid Mech.* **67**, 227.

MOORE, F. K. 1958 In *Boundary Layer Research* (ed. H. Görtler), p. 296. Springer.

PRANDTL, L. 1904 In *Proc. Intern. Math. Congr. i Br.*, p. 484.

PRUPPACHER, H. R., LE CLAIR, B. P. & HAMIELEC, A. E. 1970 *J. Fluid Mech.* **44**, 781.

ROTT, N. 1956 *Quart. appl. Math.* **13**, 444.

ROTT, N. 1964 In *Theory of Laminar Flows* (ed. F. K. Moore), p. 395. Princeton University Press.

RUITER, G. H., NAGIB, H. M. & FEJER, A. A. 1971 In *Fluid Dynamics of Unsteady, Three-Dimensional and Separated Flow* (ed. F. J. Marshall), p. 423.

SANDBORN, V. A. 1969 Characteristics of boundary layers at separation and reattachment. *College of Engng, Colorado State Univ., Res. Memo.* no. 14.

SANDBORN, V. A. & LIU, C. Y. 1968 *J. Fluid Mech.* **32**, 293.

SCHRAUB, F. A., KLINE, S. J., HENRY, J., RUMSTADLER, P. W. & LITTEL, A. 1965 *Trans. A.S.M.E.* D, *J. Basic Engng* **87**, 429.

SEARS, W. R. 1956 *J. aeronaut. Sci.* **23**, 490.

SEARS, W. R. & TELIONIS, D. P. 1971 In *Recent Research of Unsteady Boundary Layers* (ed. E. A. Eichelbrenner), vol. 1, p. 404. Laval University.

SEARS, W. R. & TELIONIS, D. P. 1975 *SIAM J. appl. Math.* **28**, 215.

SHEN, S.-F. 1978 *Adv. appl. Mech.* **18**, 177.

SIMPSON, R. L. 1977 Features of unsteady turbulent boundary layers as revealed from experiments. In *Unsteady Aerodynamics*, AGARD-CP-227, paper no. 19.

TANEDA, S. 1971 In *Recent Research on Unsteady Boundary Layers* (ed. E. A. Eichelbrenner), vol. 2, p. 1165. Laval University Press.

TELIONIS, D. P. 1970 Boundary layer separation. Ph.D. thesis, Cornell University.

TELIONIS, D. P. 1975 *A.I.A.A. J.* **13**, 1979.

TELIONIS, D. P. 1977 Unsteady boundary layers separated and attached. In *Unsteady Aerodynamics*, AGARD-CP-227, paper no. 16; also *Trans. A.S.M.E.* I, *J. Fluids Engng* **101**, 29.

TELIONIS, D. P. & KOROMILAS, C. A. 1978 Experimental investigation of unsteady separation. *VPI & SU Engng Rep.* no. VPI-E-78-24.

TELIONIS, D. P. & WERLE, J. 1973 *Trans. A.S.M.E.* E, *J. Appl. Mech.* **95**, 389.

TENNANT, J. S. 1973 *A.I.A.A. J.* **11**, 240.

TENNANT, J. S. & YANG, T. 1973 *A.I.A.A. J.* **11**, 1156.

TSAHALIS, D. TH. 1976 *A.I.A.A. J.* **15**, 561.

TSAHALIS, D. TH. & TELIONIS, D. P. 1974 *A.I.A.A. J.* **12**, 1469.

VIDAL, J. R. 1959 *Research on rotating stall in axial-flow compressors. Wright Air Development Center, Wright-Patterson Air Force, Base, Rep.* Part III. WADC TR-59-75.

WÉRLÉ, H. 1973 *Ann. Rev. Fluid Mech.* **5**, 361.

WILLIAMS, J. C. 1977 *Ann. Rev. Fluid Mech.* **9**, 113.

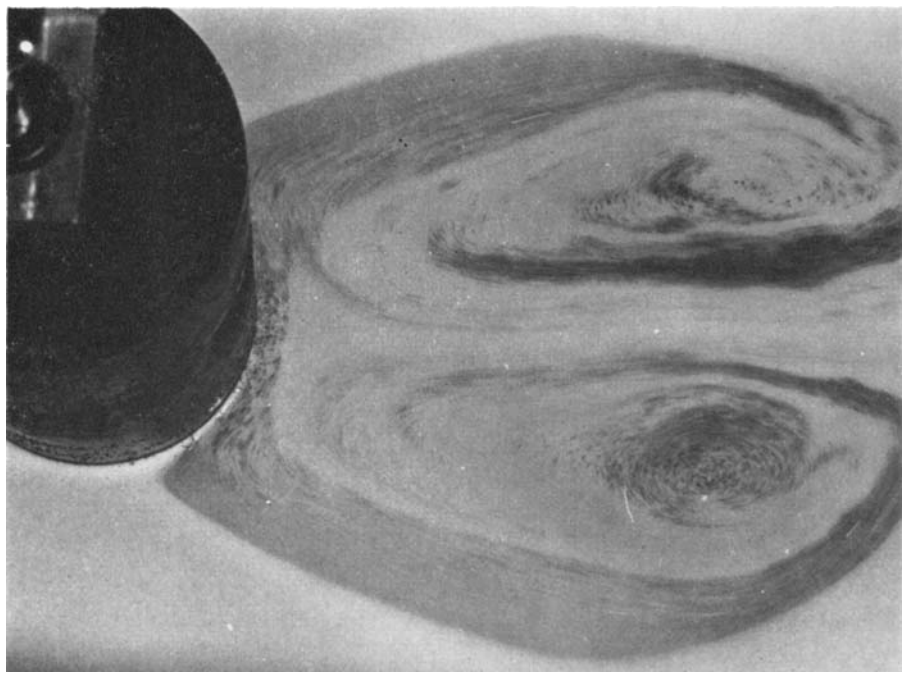

FIGURE 5. The wake of a circulate cylinder for $Re = 40$.

FIGURE 8. Separation over a downstream moving for $u_w/\bar{U}_\infty = 0{\cdot}8$ $Re = 50$.

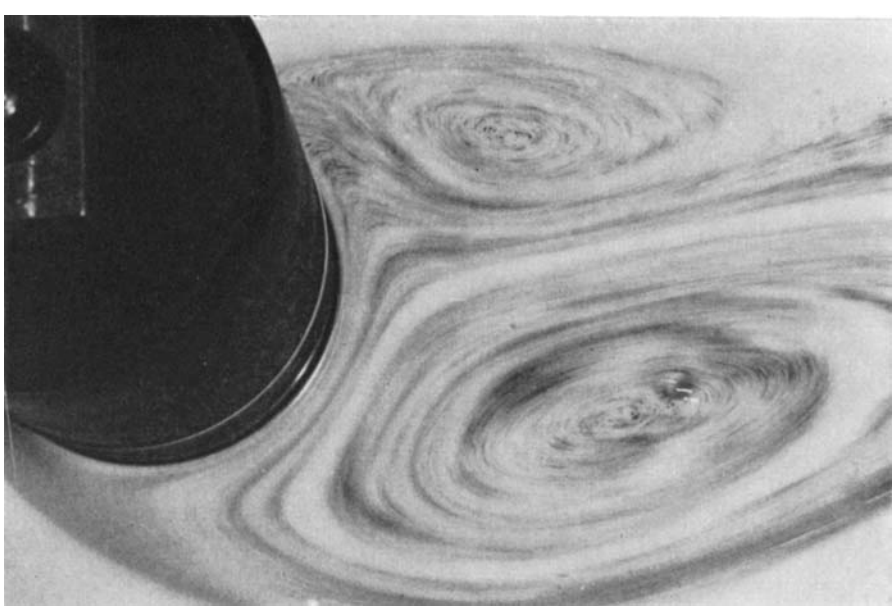

FIGURE 9. Separation over an upstream-moving wall for $u_w/U_\infty = 0{\cdot}8$ and $Re = 50$.

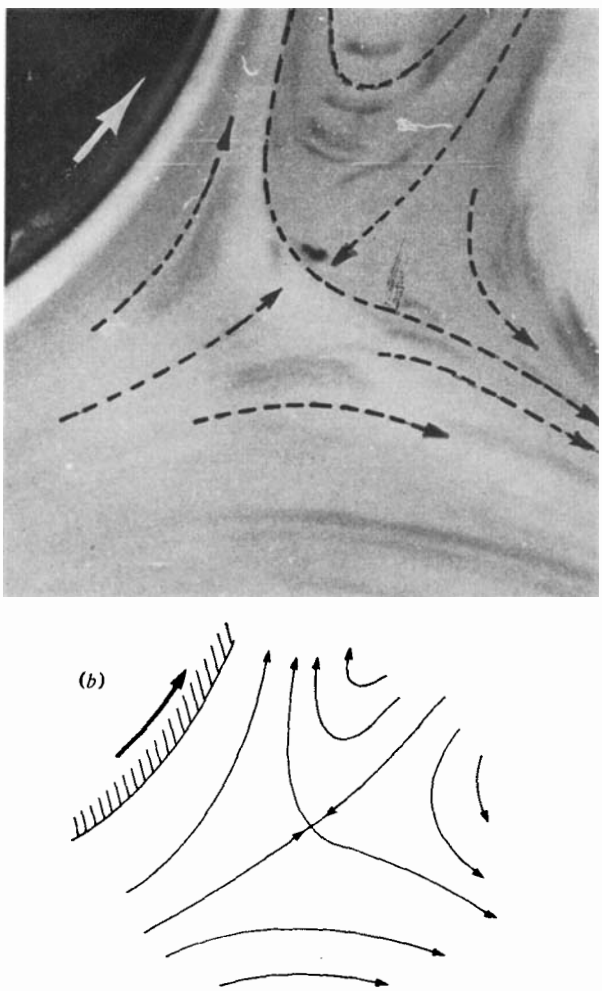

FIGURE 10. (*a*) Detail showing the saddle-point pattern for a downstream-moving wall ($u_w/U_\infty = 0{\cdot}8$, $Re = 50$). (*b*) Streamlines obtained from (*a*).

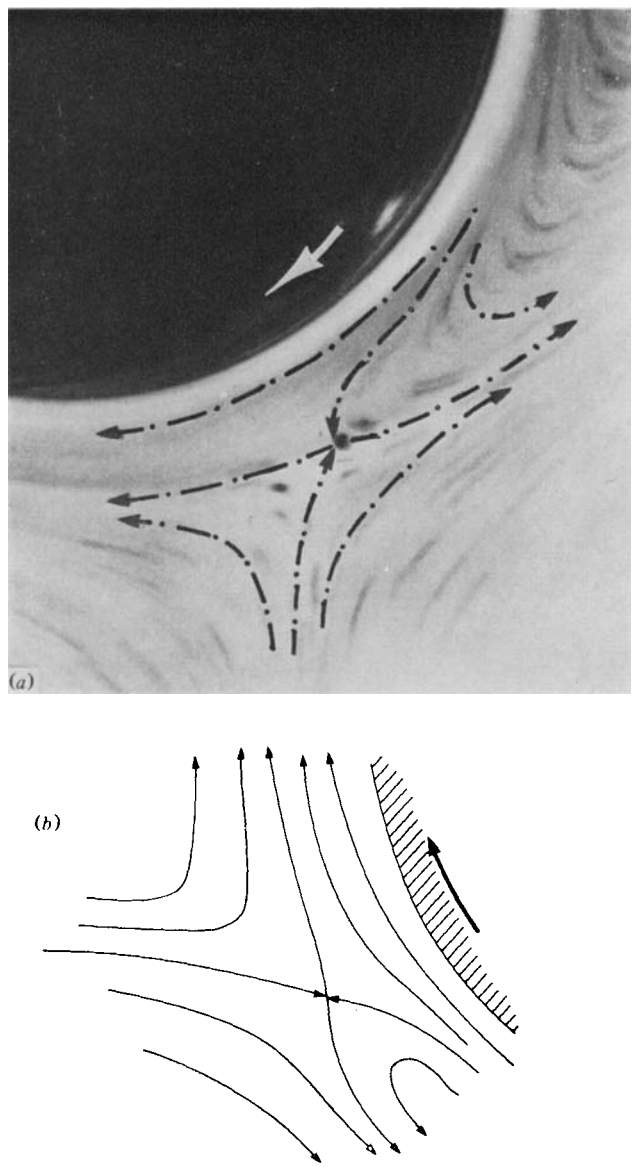

FIGURE 11. (*a*) Detail showing the saddle-point pattern for an upstream-moving wall ($u_w/U_\infty = 0{\cdot}8$, $Re = 50$). (*b*) Streamlines obtained from (*a*).

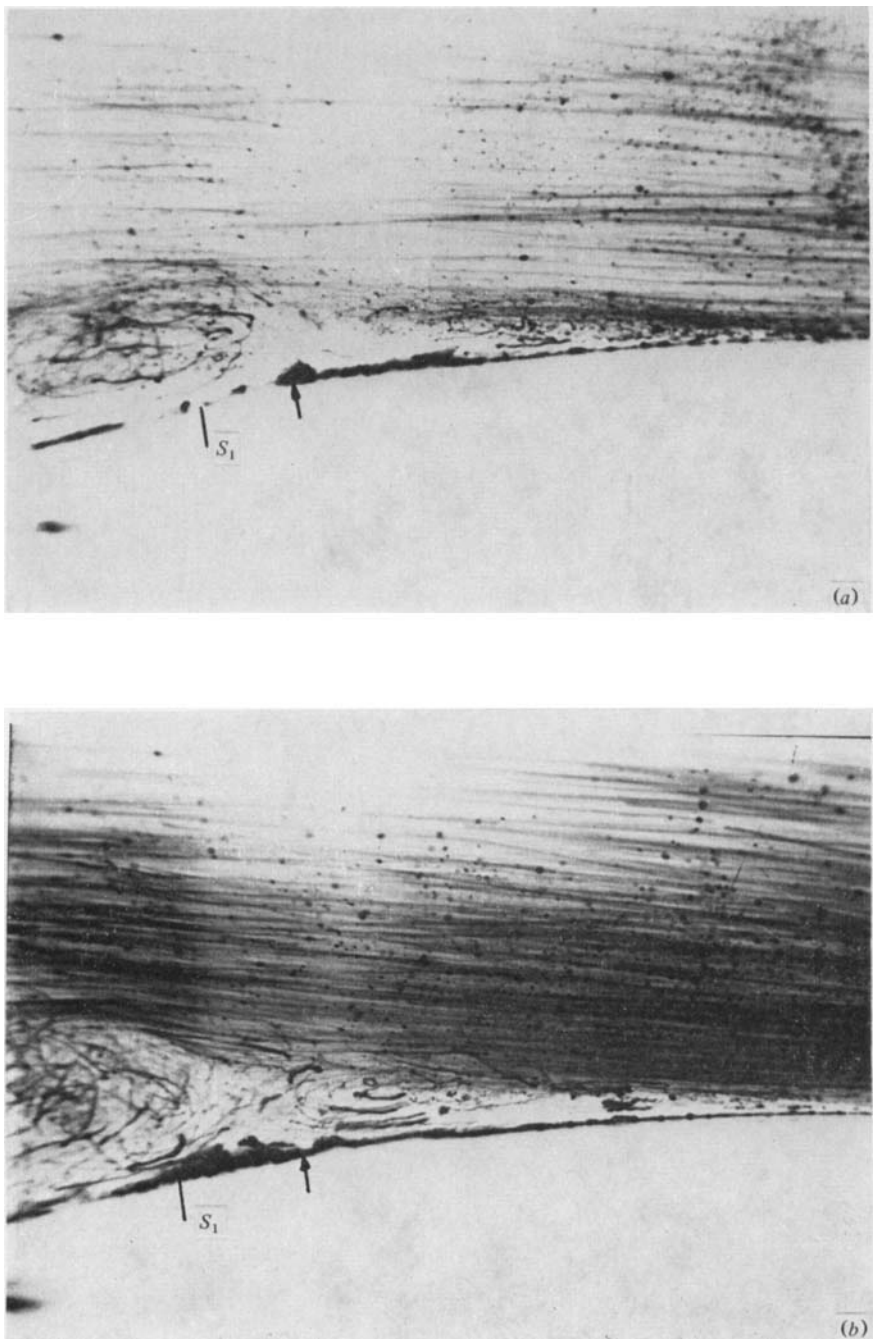

FIGURE 22. Flow visualization of an upstream-moving separation with $Re \sim 10^5$. (*a*) $t = 0{\cdot}2$ s; (*b*) $t = 0{\cdot}4$ s; (*c*) $t = 0{\cdot}65$; (*d*) $t = 0{\cdot}8$ s.

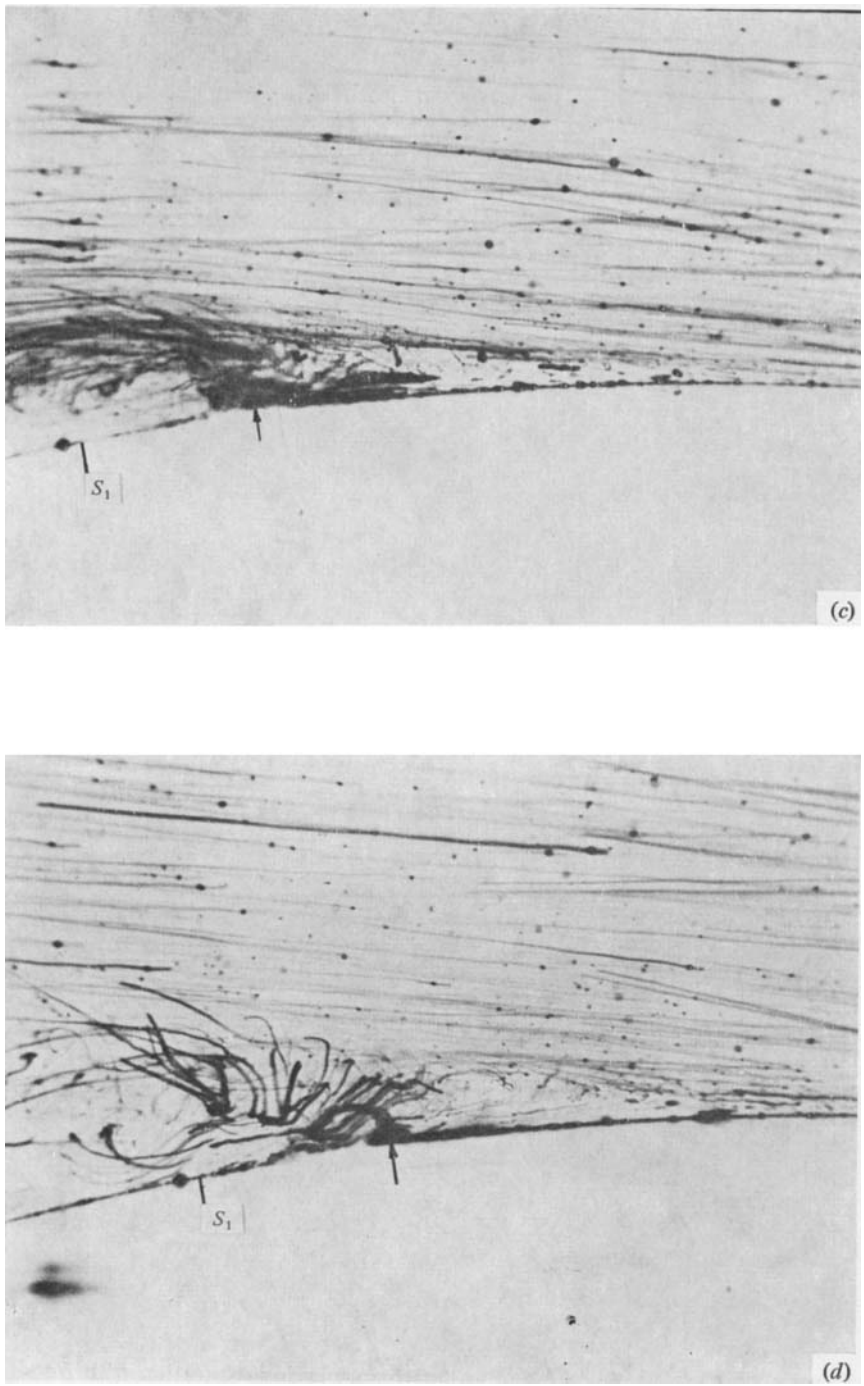

FIGURE 22. For legend see plate 5.

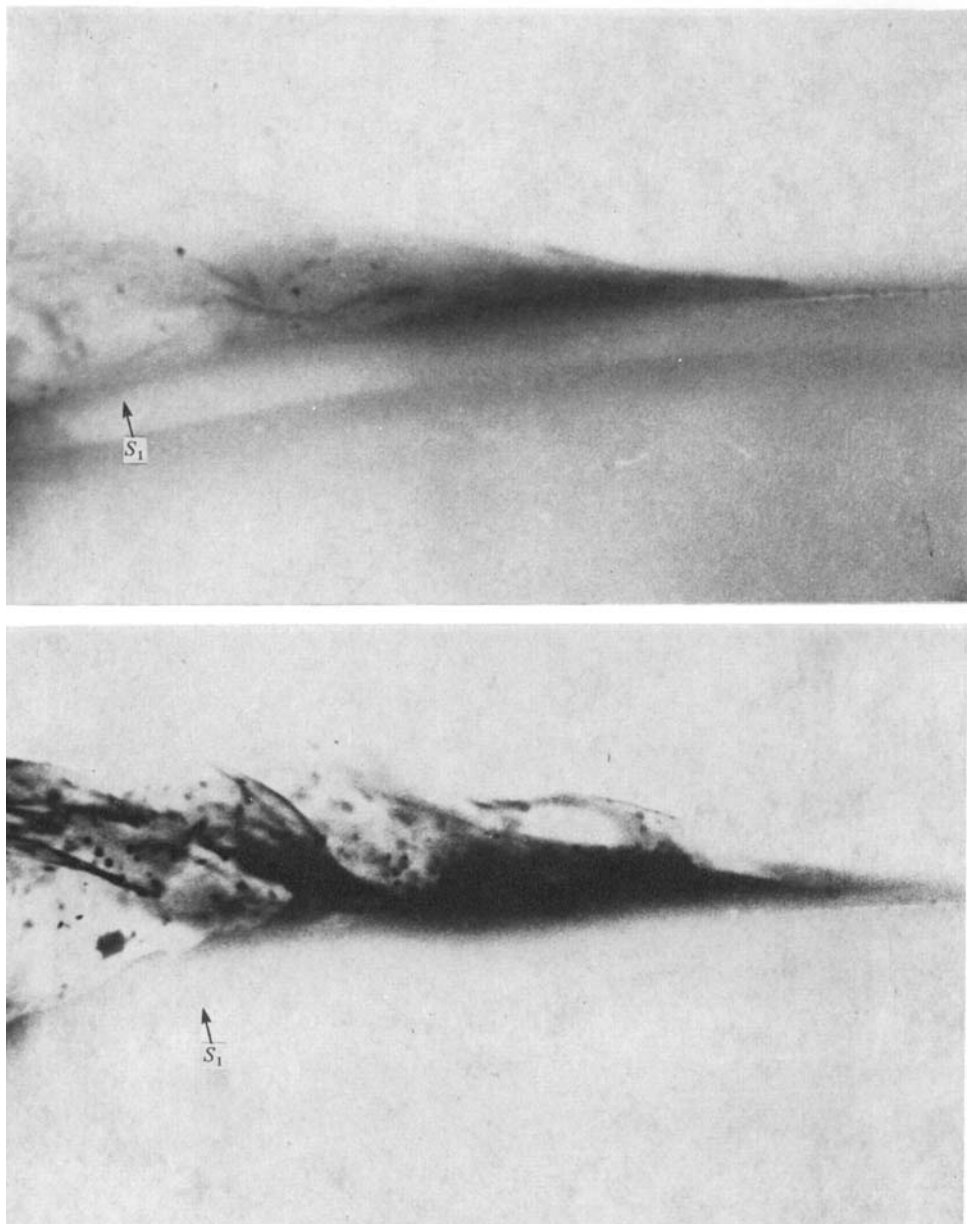

FIGURE 23. Dye visualization of the phenomenon depicted in figure 22.

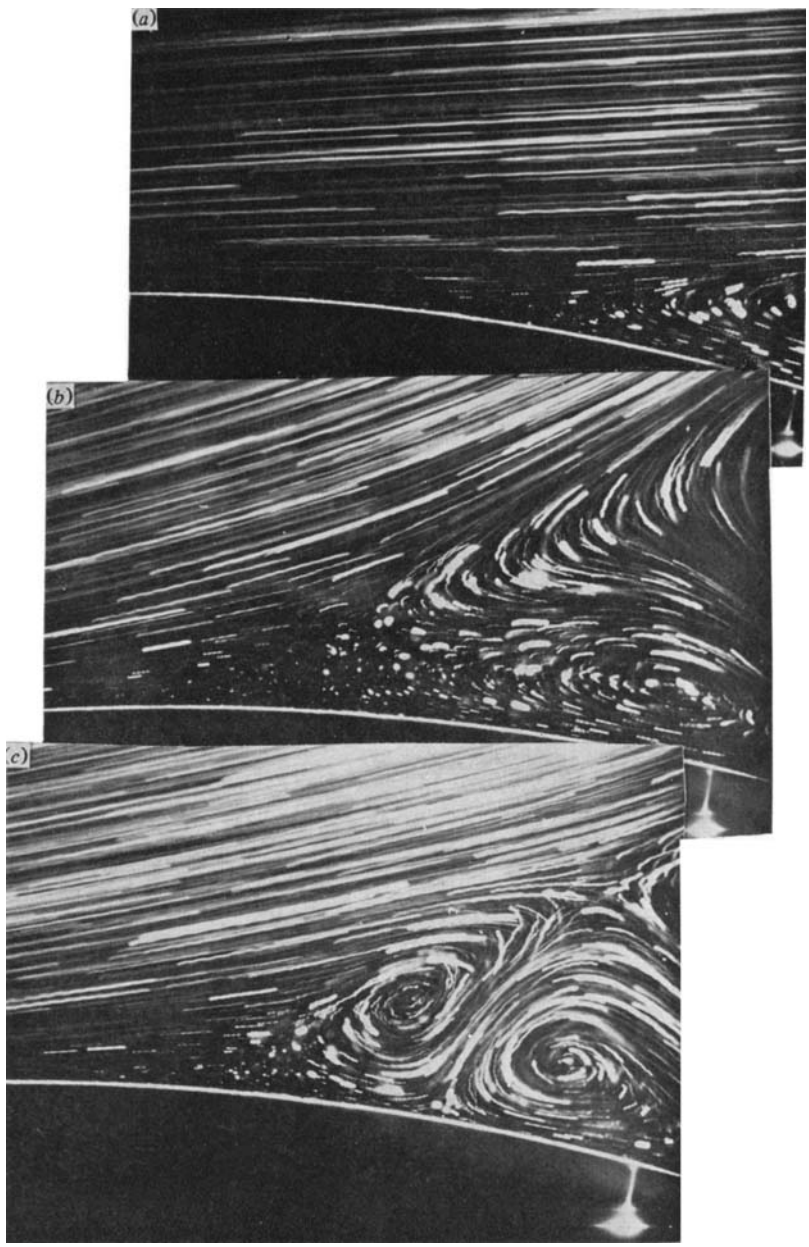

FIGURE 25. Flow visualization of instantaneous velocity fields for an impulsive change $\theta_{\mathrm{I}} = 0$ to $\theta_{\mathrm{II}} = 40°$ and $Re = 1000$. (*a*) $t = 0$ s; (*b*) $t = 0{\cdot}5$ s; (*c*) $t = 1{\cdot}5$ s; (*d*) $t = 2{\cdot}5$ s; (*e*) $t = 3{\cdot}5$ s; (*f*) $t = 4{\cdot}5$ s.

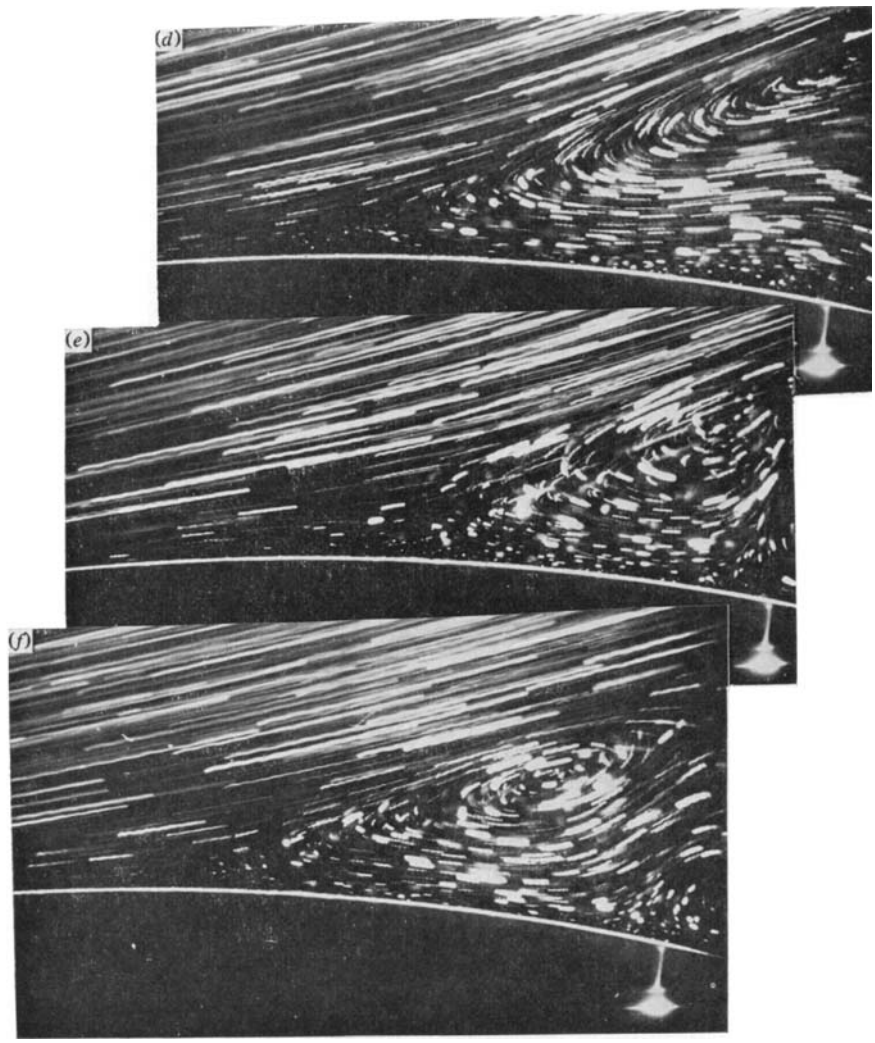

FIGURE 25. For legend see plate 8.

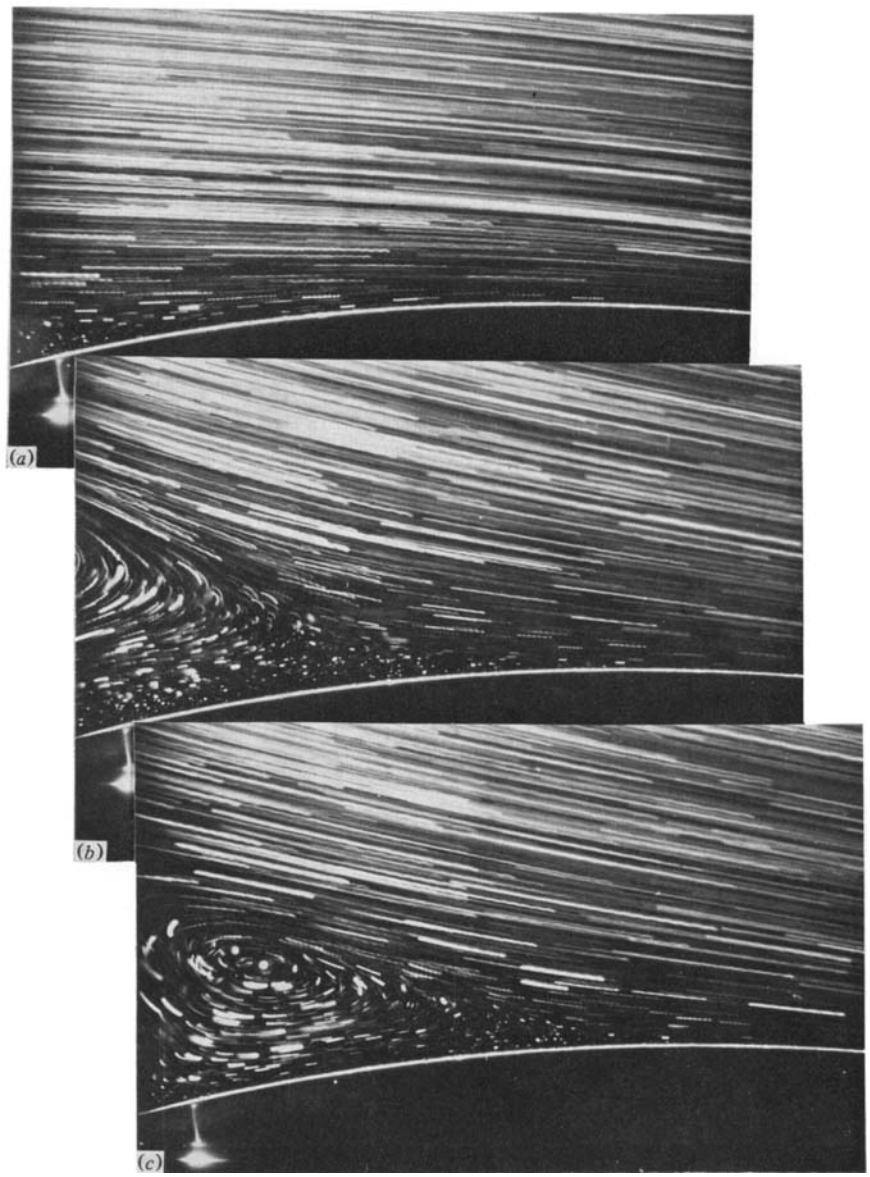

FIGURE 27. Flow visualization of instantaneous velocity fields for an impulsive change $\theta_{\mathrm{I}} = 0$ to $\theta_{\mathrm{II}} = 30°$ and $Re = 1000$. (*a*) $t = 0$; (*b*) $t = 0{\cdot}5$; (*c*) $t = 1{\cdot}5$; (*d*) $t = 2{\cdot}5$; (*e*) $t = 3{\cdot}5$.

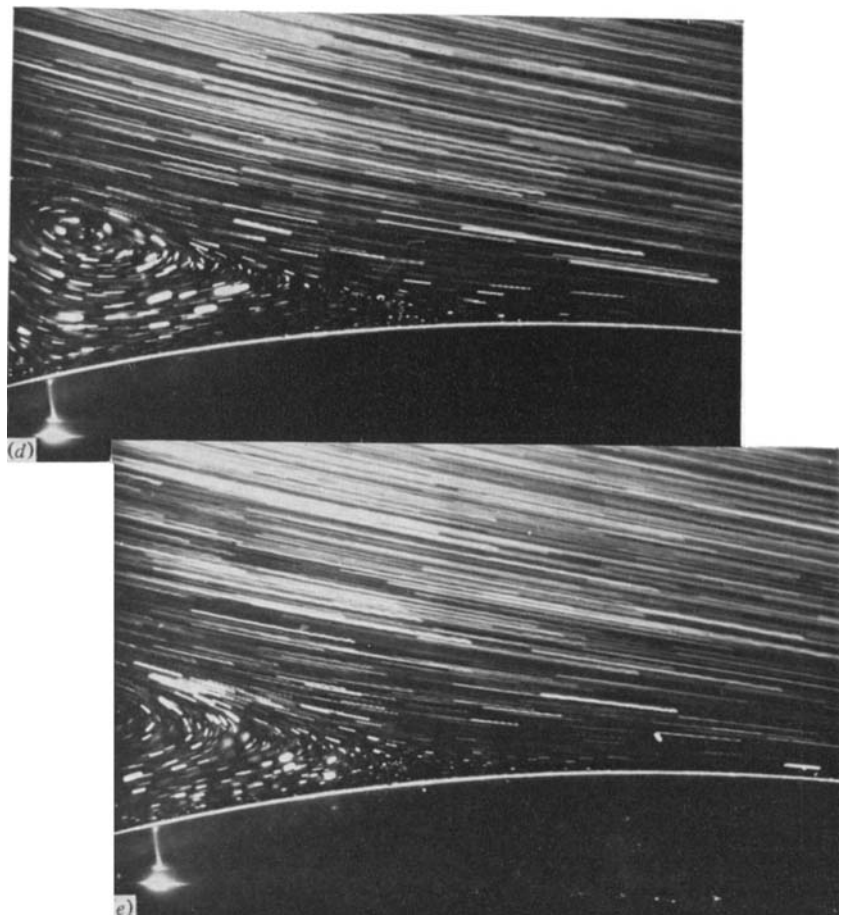

FIGURE 27. For legend see plate 10.

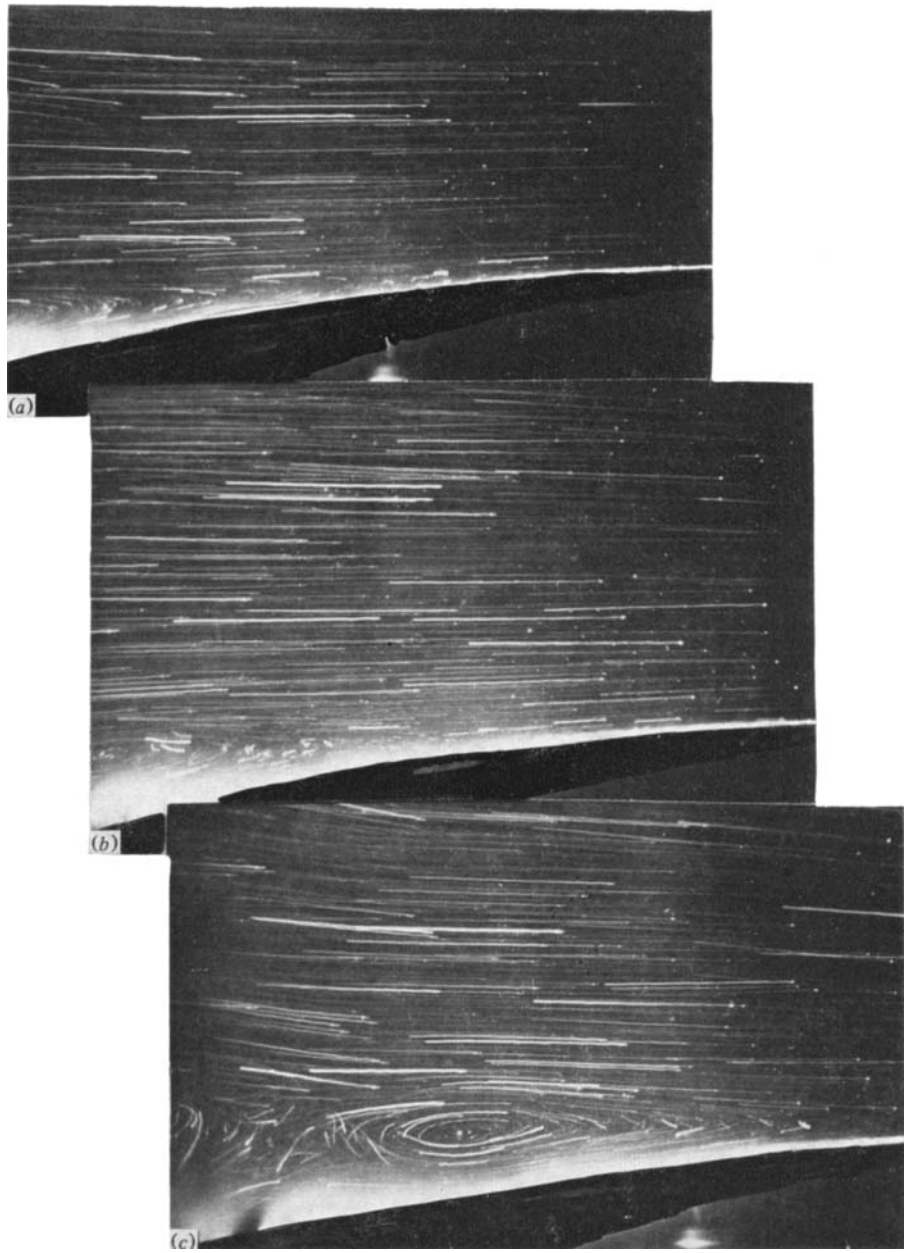

FIGURE 28. Flow visualization of instantaneous velocity fields over model B for an impulsive change $\theta_{\text{I}} = 0$ to $\theta_{\text{II}} = 35°$ and $Re = 10^4$. (*a*) $t = 0$; (*b*) $t = 1$; (*c*) $t = 2$; (*d*) $t = 4$; (*e*) $t = 5$; (*f*) $t = 7$.

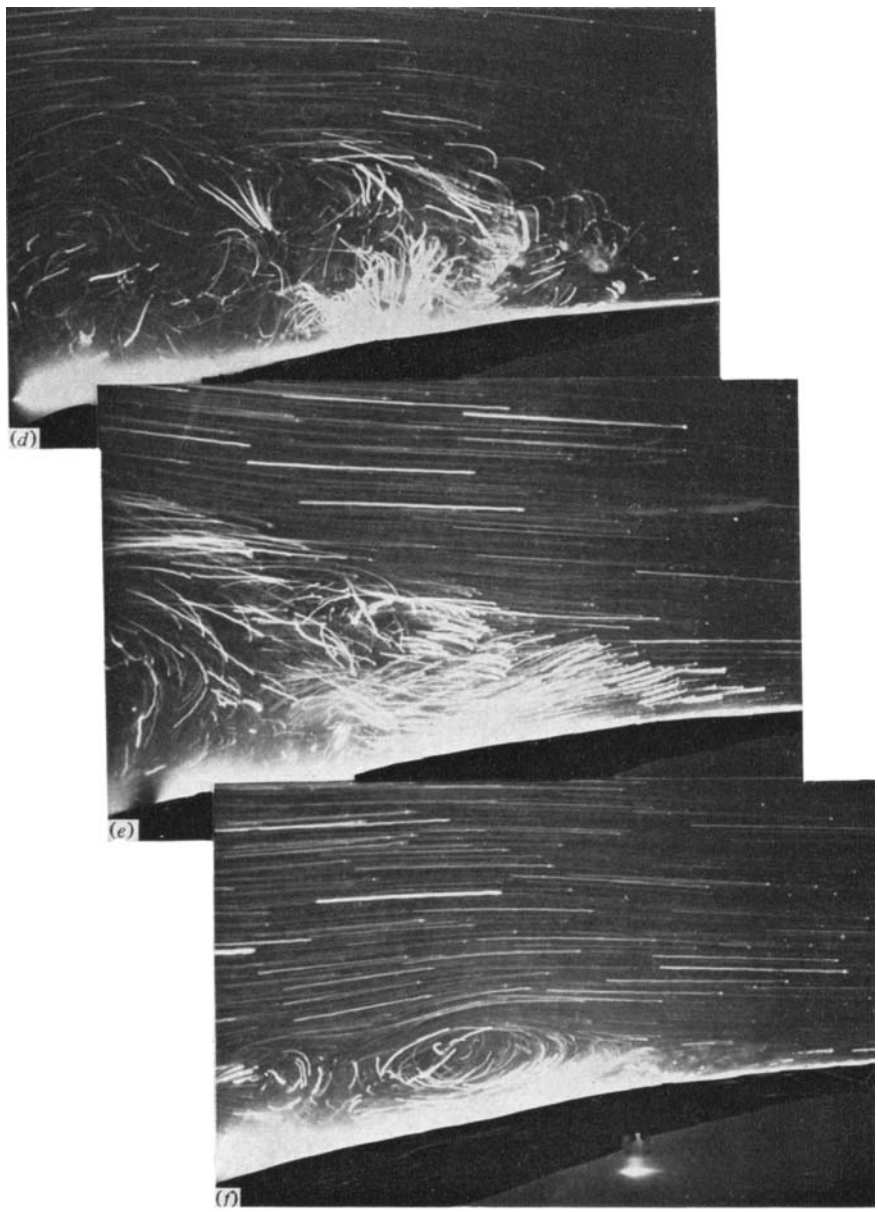

FIGURE 28. For legend see plate 12.

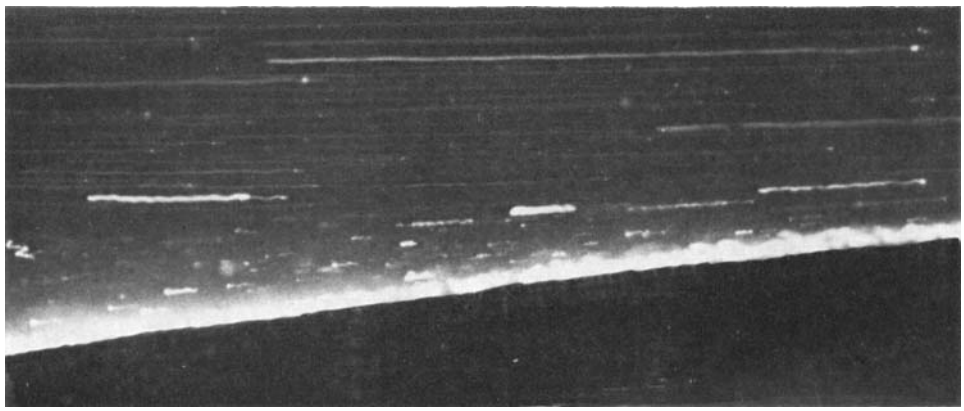

FIGURE 29. Detail of figure 28 (frame $t = 1$ s) magnification 5·7 × life-size.

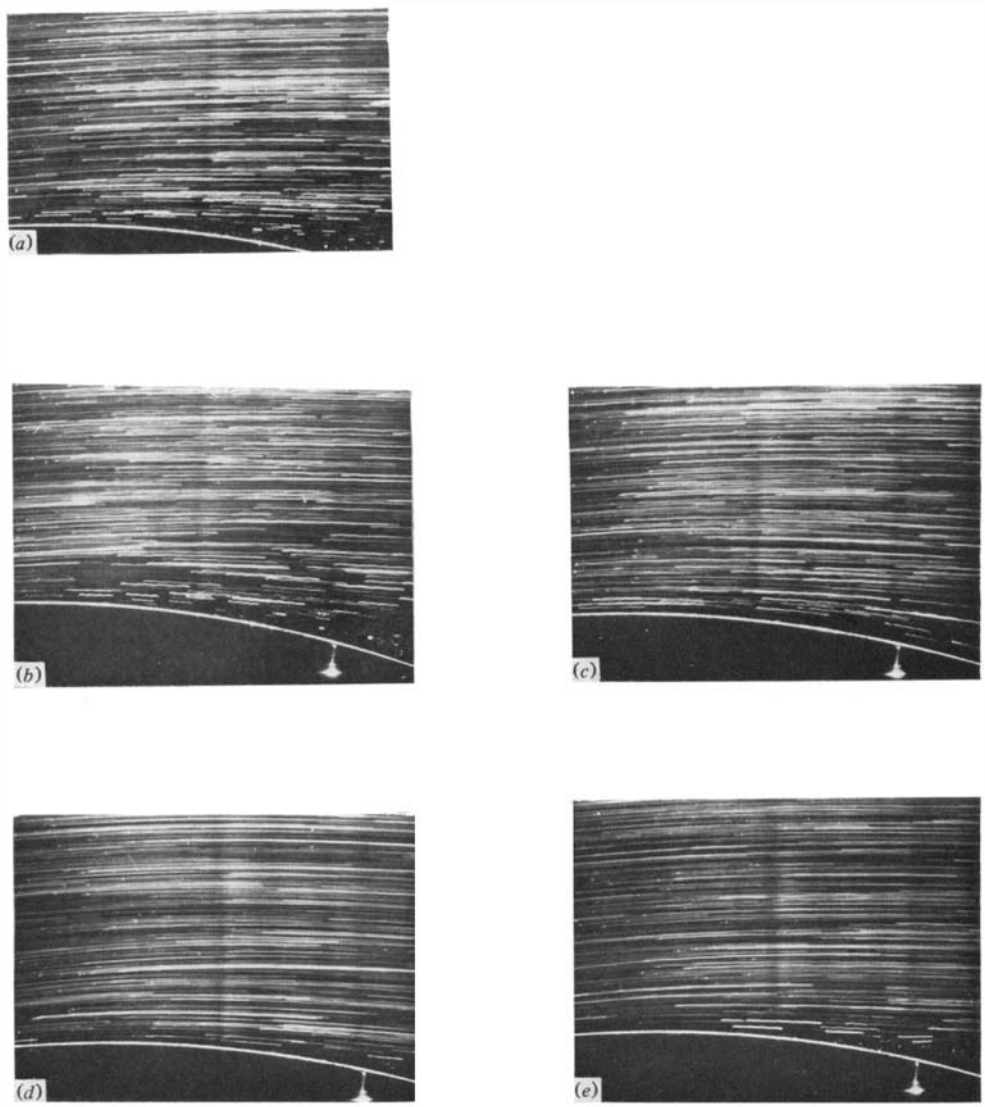

FIGURE 31. Flow visualization for flow over model A accelerating in magnitude from $U_\infty = 12\,\mathrm{cm\,s^{-1}}$ to $U_\infty = 25\,\mathrm{cm\,s^{-1}}$. (*a*) $t = 0$; (*b*) $t = 0{\cdot}5$ s; (*c*) $t = 1{\cdot}5$ s; (*d*) $t = 2{\cdot}5$ s; (*e*) $t = 3{\cdot}5$ s.

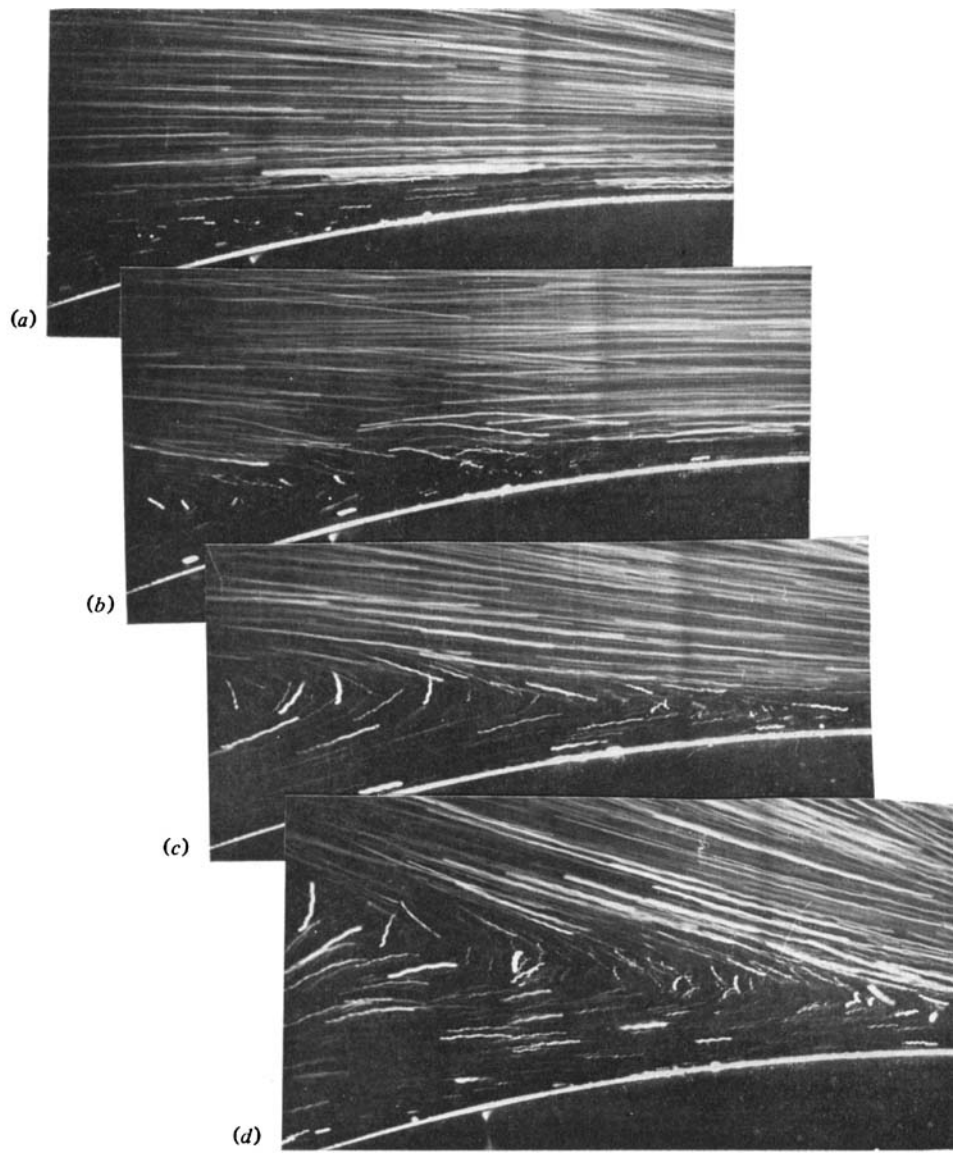

FIGURE 34. Flow visualization for flow over model B decelerating in magnitude from $U_\infty = 20$ cm s^{-1} to $U_\infty = 12$ cm s^{-1}. (*a*) $t = 0{\cdot}5$ s; (*b*) $t = 1{\cdot}5$ s; (*c*) $t = 2{\cdot}5$ s; (*d*) $t = 3{\cdot}5$ s.

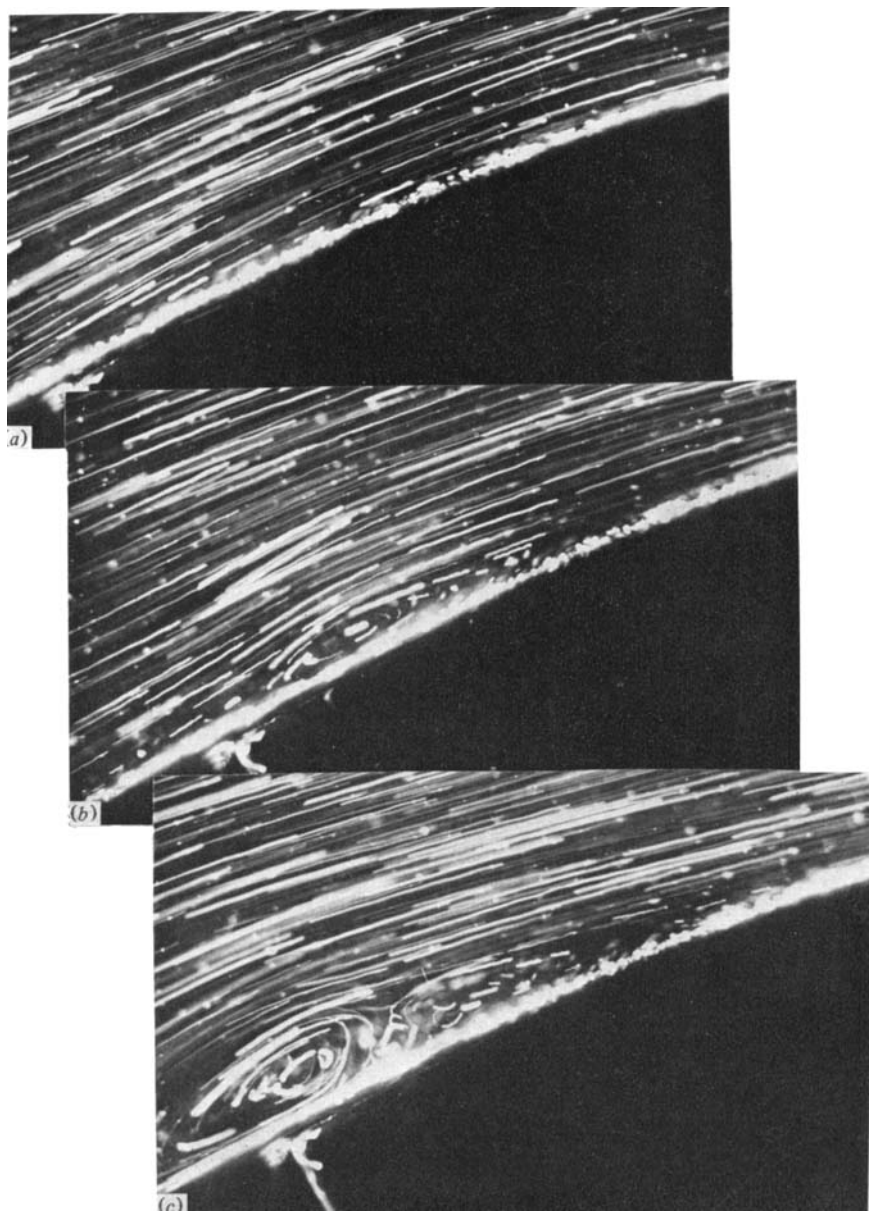

FIGURE 36. Flow visualization for flow over model C impulsively bending as in figure 17, $Re = 10^4$. (*a*) $t = 0$ s; (*b*) $t = 0{\cdot}4$ s; (*c*) $t = 0{\cdot}8$ s; (*d*) $t = 1{\cdot}2$ s; (*e*) $t = 1{\cdot}6$ s.

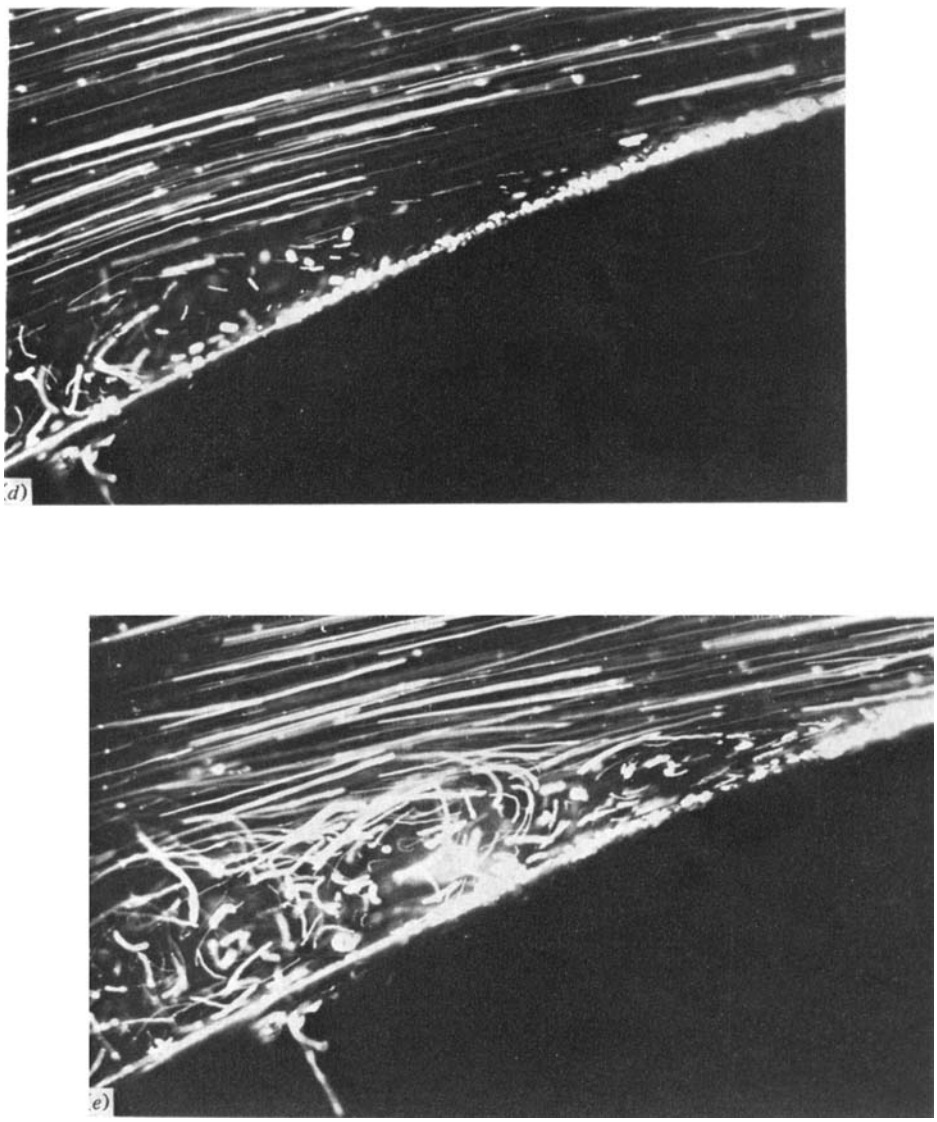

FIGURE 36. For legend see plate 17.

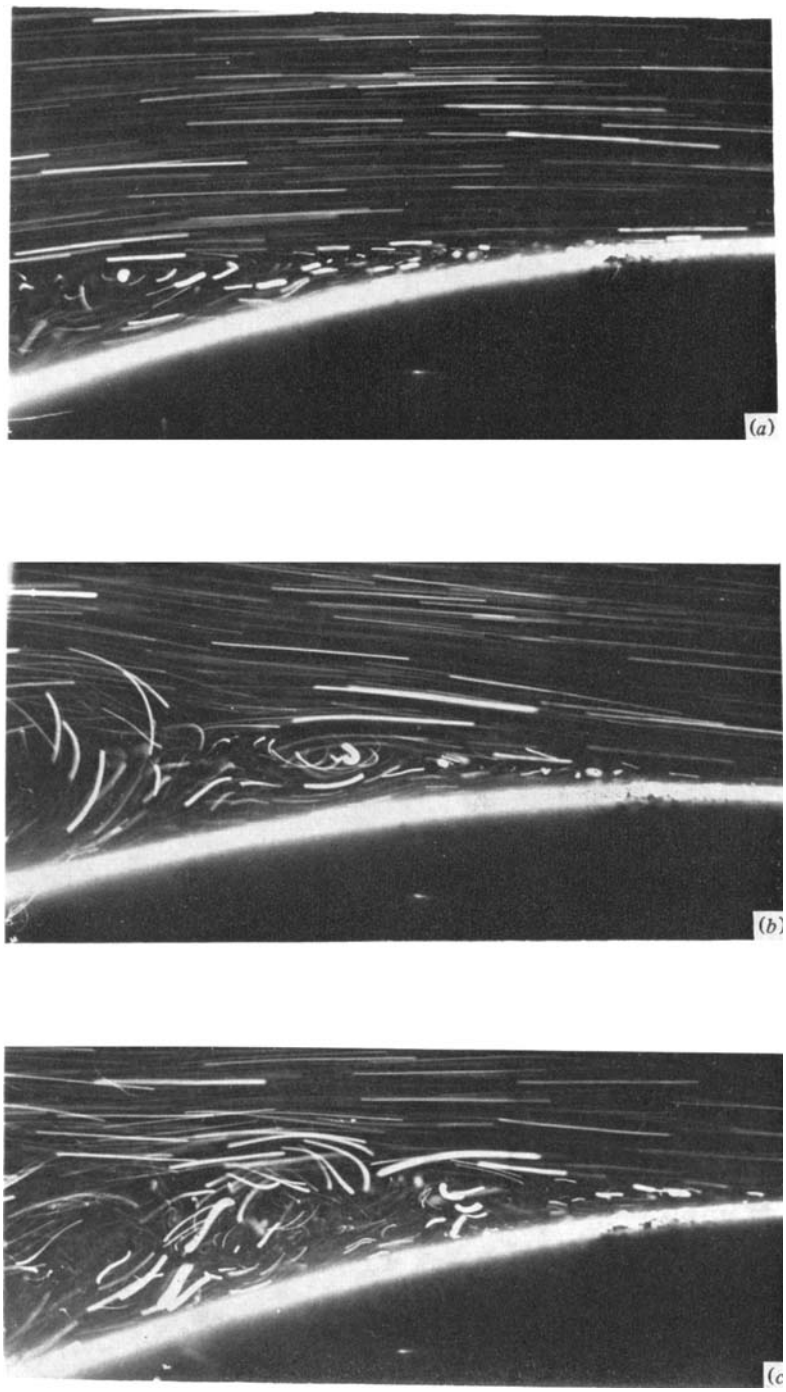

FIGURE 38. Flow visualization for oscillatory flow over model A with a period $T = 0{\cdot}6$ s and $Re = 5 \times 10^5$. (*a*) $t = \frac{1}{6}T$; (*b*) $t = \frac{2}{6}T$; (*c*) $t = \frac{3}{6}T$; (*d*) $t = \frac{4}{6}T$; (*e*) $t = \frac{5}{6}T$.

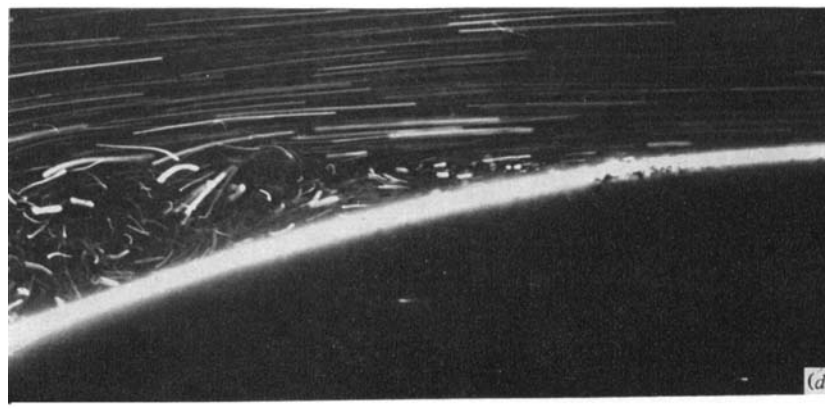

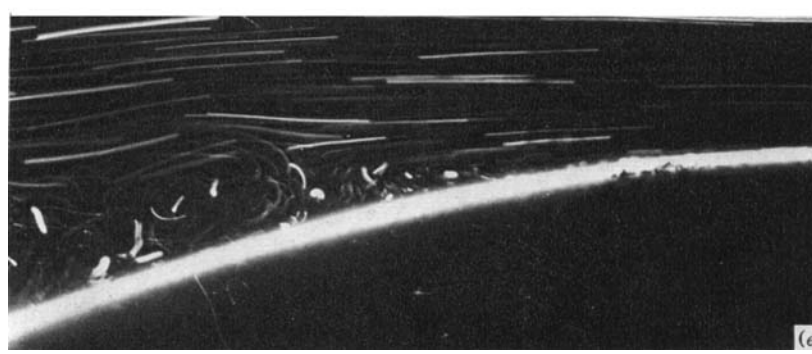

FIGURE 38. For legend see plate 19.

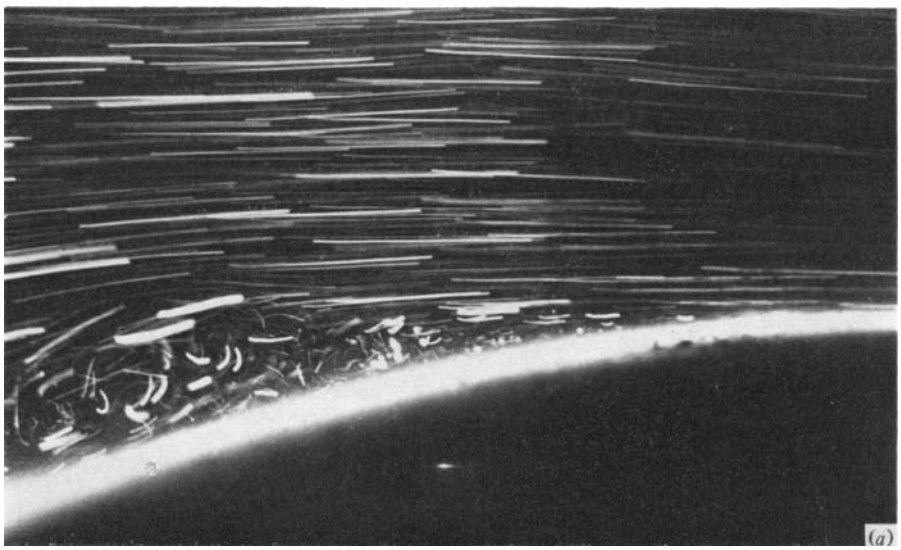

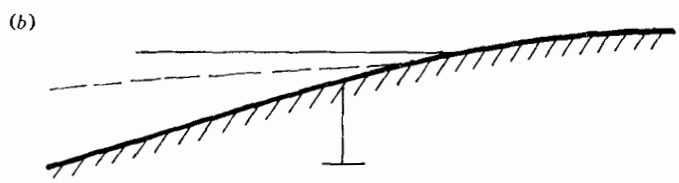

FIGURE 39. (*a*) Visualization of steady flow at $Re = 10^5$ with flap positioned at I. (*b*) Boundaries separating recirculating from outer flow: – – –, frame $\frac{1}{6}T$ from figure 38; ——, flow from figure 39(*a*).

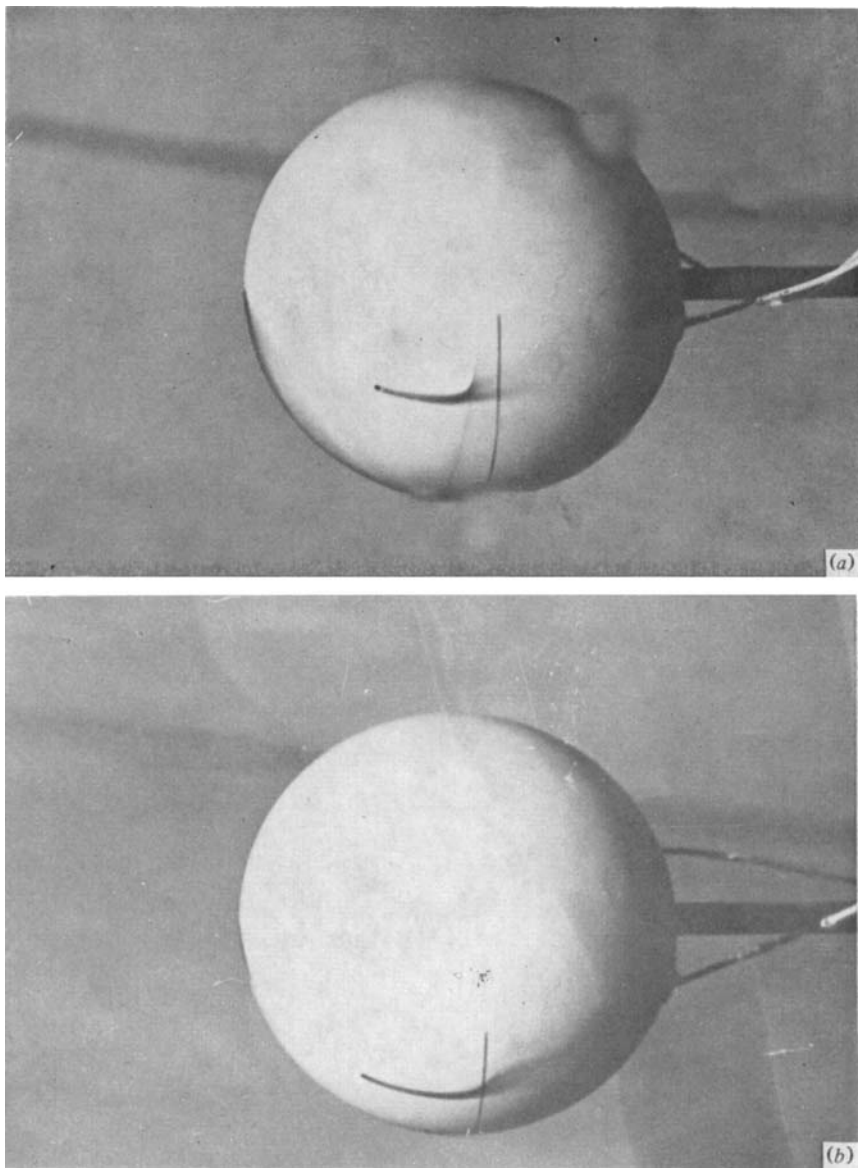

FIGURE 47. Visualization of the flow about a sphere for $Re = 10^5$, $St = 3{\cdot}2$. (*a*) Fixed sphere; (*b*) oscillating sphere.